ROUSLAN BIRABASSOV

DYNAMIC HOLOGRAPHIC GRATINGS

Thèse
présentée
à la Faculté des études supérieures
de l'Université Laval
pour l'obtention
du grade de Philosophiae Doctor (Ph.D.)

Département de physique
FACULTÉ DES SCIENCES ET DE GÉNIE
UNIVERSITÉ LAVAL
QUÉBEC

APRIL 2001

UNIVERSITÉ LAVAL

Faculté des études supérieures

ATTESTATION

Ce 9e jour du mois de avril 2001, les personnes soussignées, en leur qualité de membres du jury de la thèse de Rouslan BIRABASSOV, ont assisté à la soutenance de cette thèse.

NOMS	UNIVERSITÉ	SIGNATURE
Tigran Galstain	Laval	
Nathalie McCarthy	Laval	
Roger-A. Lessard	Laval	
Alain Blouin	CNRC, Montréal	

Prof. Quang HO-KIM

SIGNATURE DU PRÉSIDENT DE LA SOUTENANCE

À Émilie et ma Mère

Résumé court

Dans la première partie de cette thèse, nous présentons l'étude théorique et expérimentale de réseaux dynamiques dans les matériaux photoanisotropes. L'étude de réseaux photoanisotropes démontre que l'on peut enregistrer et reconstruire un état de polarisation elliptique de la lumière. Une chiralité optique dans ces matériaux a également été créée. Les résultats de l'analyse théorique, basée sur la théorie des ondes couplées, correspondent bien aux résultats expérimentaux. De plus, les réseaux qui donnent une diffraction asymétrique dans ces matériaux sont fabriqués et étudiés.

Dans la deuxième partie de la thèse, la diffusion stimulée en arrière dans les cristaux photoréfractifs est analysée. Les avantages des réseaux de réflexion sur les réseaux de transmission sont démontrés. Différents paramètres du cristal photoréfractif sont mesurés: le coefficient d'amplification, le coefficient de réflexion, le temps de réponse, la conductivité dans l'obscurité, et le temps d'effacement des réseaux. Les conditions pour obtenir la conjugaison de phase y sont discutées. Une comparaison des sensibilités de différentes géométries a aussi été effectuée.

Rouslan Birabassov

Dr. T. Galstian
Directeur de recherche

Résumé

Cette thèse contient deux parties. En premier lieu, nous présentons l'étude théorique et expérimentale de réseaux dynamiques dans les matériaux photoanisotropes. En deuxième partie, nous retrouvons l'étude de diffusion stimulée en arrière dans les cristaux photoréfractifs.

Dans la première partie de cet ouvrage, nous avons utilisé les polymères dopés par des colorants azoïques en tant que matériaux photoanisotropes. L'intérêt actuel pour ces matériaux est dû à la réversibilité de phénomènes photoinduits qui sont accompagnés par un dichroïsme et une biréfringence linéaires.

Une nouvelle technique pour la fabrication de films épais et de bonne qualité optique a été proposée. Afin de bien comprendre les mécanismes de photoisomérisation et de réorientation angulaire, l'expérience a été effectuée. La photoisomérisation des molécules anisotropes de colorant dépend non seulement de l'intensité, mais également de l'état de polarisation de la lumière. L'étude théorique et expérimentale démontre que l'on peut enregistrer et reconstruire un état de polarisation elliptique de la lumière en utilisant les réseaux photoanisotropes minces. Un faisceau polarisé linéairement a été utilisé pour l'enregistrement et la reconstruction de l'état de polarisation.

L'étude théorique basée sur la théorie des ondes couplées, ainsi que l'étude expérimentale démontrent que l'on peut créer une chiralité optique en utilisant ces matériaux et en choisissant l'état de polarisation du champ d'excitation.

De plus, les réseaux qui donnent une diffraction asymétrique dans ces matériaux sont fabriqués et étudiés. Le déphasage spatial du réseau d'indice de réfraction relativement au

UNIVERSITÉ LAVAL

Faculté des études supérieures

ATTESTATION

Ce 9e jour du mois de avril 2001, les personnes soussignées, en leur qualité de membres du jury de la thèse de Rouslan BIRABASSOV, ont assisté à la soutenance de cette thèse.

NOMS	UNIVERSITÉ	SIGNATURE
Tigran Galstain	Laval	
Nathalie McCarthy	Laval	
Roger-A. Lessard	Laval	
Alain Blouin	CNRC, Montréal	

Prof. Quang HO-KIM

SIGNATURE DU PRÉSIDENT DE LA SOUTENANCE

Abstract

The work presented in this thesis is divided into two related areas. The first area of research was a study of photoanisotropic materials to record dynamic gratings. The second area was a study of stimulated diffusion backscattering in photorefractive crystals. The two areas are related by the fact that in the two cases we studied dynamic gratings.

We studied reversible photochemical mechanisms using dye molecules suspended in polymer hosts that could record dynamic holograms. The self-developing refractive index changes in dye-doped or dye-attached polymer materials, in particularly azo-dye-doped polymer systems make them promising candidates for many applications (because of the large photoinduced birefringence). The mechanism of photoanisotropic recording in azo-dye-doped polymer materials is based on orientationally dependent photoisomerization of dye molecules that may be macroscopically described in terms of photoinduced linear dichroism and linear birefringence.

We proposed a technique for the fabrication of thick photosensitized polymer materials for real-time (self-developing) holographic applications. Cross modulation experiments to study the photoinduced dichroism are then described and the discussion of photophysical mechanisms involved is given. We used azo-dye doped polymer materials to record thin and thick holograms (scalar and vector). We theoretically and experimentally demonstrated that one could successfully store (using a linearly and an elliptically polarized beams) and reconstruct an elliptical polarization state of light using photoanisotropic materials, even if a plane polarized reference beam is used for the recording and readout. Using photoanisotropic materials, we demonstrated experimentally and theoretically that macroscopic optical chirality may be generated in such systems with a proper choice of excitation beam polarization state. Linear diffraction gratings, that provide strongly asymmetric diffraction without surface

modulation were also created and studied. Asymmetric diffraction may be achieved using blazed gratings. But in our case the spatial phase shift of the refractive index grating relative to the absorption grating is the origin of asymmetric behaviour. Experimental results made with thin mixed phase and absorption gratings in azo-dye-doped polymer films are in agreement with our theoretical results.

In the second part of the thesis we analysed the stimulated diffusion backscattering (SDS) in photorefractive crystals based on the advantages of the reflection photorefractive gratings. The material research, which is the most acute direction, was studied. We believe that optimal crystal (its processing procedure and doping density) is still unknown even for visible range. We discussed the general analysis of the stimulated diffusion backscattering. We studied the relevant parameters for the sample, which demonstrated the most interesting stimulated diffusion backscattering response: measurements of gain, reflectivity, response rate, dark conductivity and grating decay. We clarified the principal possibilities to obtain self-phase conjugation at backward SDS in steady-state conditions. We also made the comparison of sensitivities of different geometries with respect to pump energy. Finally, we experimentally studied double-phase-conjugation geometry at double-loop reflection gratings.

Rouslan Birabassov

Dr. T. Galstian
Thesis advisor

Avant-propos

Ces travaux ont été réalisés au Laboratoire de matériaux et composants optoélectroniques du Centre d'optique, photonique et laser de l'Université Laval. Ce laboratoire est le fruit du dynamisme et de l'engagement du Professeur Tigran Galstian.

Je remercie le Professeur T. Galstian, directeur de ma thèse, pour son soutien, sa confiance en moi et qui durant ces trois années s'est attaché à me guider dans ma démarche de jeune chercheur.

Je tiens à exprimer mes remerciements au Professeur V.Shkunov et au Dr. A. Mamaev qui m'ont fait entrer dans le monde scientifique. Je les remercie pour leur disponibilité et leur patience. Je leur suis reconnaissant pour les nombreuses discussions sur la deuxième partie de ma thèse et leur collaboration.

J'adresse mes remerciements au Professeur A. Ritcey et à Frédéric Dechamplain pour l'aide reçue dans la préparation de mes échantillons, les polymères dopés.

Je tiens également à remercier mes collègues de laboratoire, ainsi que le personnel de soutien du COPL et du département de physique. En particulier, j'aimerais remercier E. Brasselet et A. Yavrian pour de nombreuses discussions enrichissantes.

Finalement, je remercie le Gouvernement du Québec et ainsi que le Professeur Tigran Galstian pour leur support financier.

TABLE OF CONTENTS

LIST OF FIGURES

LIST OF TABLES

INTRODUCTION

Important practical applications of laser-induced dynamic gratings are extremely widespread in modern optical technology. Some of these applications are storage of volume holograms [1-3], data processing and optical logic [1, 4], filtering [5], image processing [6], beam couplers in integrated and guided wave optics [7], phase conjugation [8-10], polarimeters [11], holographic interferometry [1, 33], etc. These practical applications have provided steady motivation to study and develop new materials as well as to understand diffraction processes. In order to record optical gratings, the optical properties of materials (refractive index and coefficient of absorption) are spatially modulated in the interference region of interaction beams. Permanent gratings have been produced in this way by photographic processes for many years. The well-known silver-halide photographic emulsions, photochromic and thermoplastic materials, etc. are used for permanent hologram recording [1, 3].

In this thesis, the dynamic or transient gratings are studied. The dynamic gratings disappear after the inducing light source, usually a laser, has been switched off. The holograms are dynamic because, simultaneously with the grating recording and erasure, diffraction of the incident beams from the grating recorded previously (self-diffraction) will occur. One of the interesting consequences of the grating dynamic nature is the possibility of automatic adjustment of the grating to the corresponding recording conditions. Another advantage of these materials in real-time holographic applications is that no chemical processing of the recording medium is needed.

A wide variety of existing photosensitive materials may be used for dynamic holographic recording of interference patterns [1, 3, 10-21]. These materials may be organic or inorganic. The recorded gratings may be phase (refractive index), absorption or mixed gratings [24, 25]. The diffracted power may be primarily in backward-diffracted orders (reflection gratings) or primarily in forward-diffracted orders (transmission gratings). The diffraction may

be described by Raman-Nath regime (thin gratings), by Bragg regime (thick gratings) or by a mixture of both [22-26]. The optical excitation of materials can be treated using different theoretical descriptions with varying levels of sophistication. Extensive reviews of holographic recording materials and laser-induced diffraction gratings have been written, see for example [1-3, 12-17, 19-36, 118].

In this thesis two important dynamic recording materials are studied: photoanisotropic materials and photorefractive crystals.

Photoanisotropic materials

A growing number of organic optical materials attracts interest for both fundamental scientific reasons as well as for possible applications. We are primarily interested in writing dynamic gratings, therefore we will limit our discussion mainly to solid phase dye-doped polymer systems, which have a reversible recording, erasure capability, and isotropy. The most promising of them are azo-dye-doped polymer systems because of their large value of the photoinduced birefringence [19-21, 31-39, 49-50]. Dynamic recording occurs in these materials, in which a reversible photochemical process transforms single chemical species in two different states that have different absorption spectrum. From the Kramers-Kronig relationship, we know that the change in index of refraction accompanies the change in absorption. When a spatially varying intensity pattern strikes a dye-doped sample, the intensity variation results in a variation of the extent of isomeric transformations across the sample. This is because the rate of photochemically induced transformations depends on light intensity. The spatially nonuniform photochemistry in turn results in a spatial variation in the index of refraction and the absorption coefficient. The excited state of dye molecules is thermally unstable at room temperature, so they will return to their stable state after the excitation light is removed, which lead to the erasure of the hologram.

One of the interesting properties of photoanisotropic materials is that they are sensitive not only to intensity modulation but also to the polarization modulation of the total field [19-21, 31-54]. This means that these materials can be used to record either a pure spatially

varying intensity distribution or a pure spatially varying polarization pattern (polarization gratings) or a combination of both. The progress of polarization holography is hampered considerably by the performance of existing recording materials. This motivates us to fabricate and to study the photoanisotropic materials.

The theoretical analysis to understand light diffraction in isotropic media experienced a major break through with the coupled wave theory of Kogelnik for thick gratings [24] and Raman-Nath theory for thin gratings [23]. Exact formulations without approximations (rigorous coupled –wave analysis and rigorous modal analysis) for isotropic media were developed by Moharam and Gaylord [28, 29]. Despite the fact that a large fraction of the materials used for grating's recording is anisotropic, only limited effort has been made to theoretically and experimentally analyze the diffraction in this kind of media [40-43, 45-46]. This motivates us to theoretically and experimentally study thin and thick photoanisotropic gratings. Mixed phase and absorption gratings, with common grating vector and arbitrary relative phase shift, are also considered. Asymmetric diffraction was experimentally demonstrated for the first time, to our knowledge, in this thesis.

Photorefractive crystals

Noncentrosymmetric materials, which are photoconductive and electrooptic, may exhibit the photorefractive effect in which the index of refraction can be modulated due to spatial variations of the incident intensity. The optical nonlinearity of the photorefractive effect results from the following chain of processes [12-17]:

1) Photoexcitation of free charge carriers;
2) Spatial redistribution of charge carriers under the action of fields or by diffusion;
3) Trapping of the carriers by the trapping centers with the formation of an inhomogeneous space charge;
4) Modulation of the refractive index by the space-charge field by means of the electrooptic effect.

The separation of charges can occur in two ways. The first is based on spatial modulation of the intensity [12-17]. This leads to a spatially nonuniform distribution of carriers, which are transported either by an external electric field, diffusion or under the effect of intensity-dependent component of photovoltaic current.

The second mechanism for the formation of a space charge is polarization-dependent photovoltaic currents [115]. Currents brought by circularly polarized light exist in doped 3m-group crystals. The direction of current propagation depends on whether the polarization is right-hand or left-hand-circular. This makes possible the recording of gratings with two beams having orthogonal states of polarization.

The photorefractive effect is a very exciting phenomenon because it is not spatially local. This means that the nonlinear polarization at a particular point depends upon the light field at other nearby points. Therefore, the maximum refractive index change does not necessarily occur where the intensity of the incident beams is the greatest. This spatial mismatch between the interference pattern, produced by the signal beam and pump waves, and the grating recorded in the media is a necessary condition for amplification of weak signal. In a nonlocal-response medium this shift stems from the properties of the material itself (noncentrosymmetry) [12, 13]. Parametric processes in local-response media are characterized by a mismatch of the own interference pattern (i.e. the pattern formed with the participation of the signal wave under consideration) with respect to the grating written by foreign beams. In stimulated processes, the shift of the moving grating with respect to the moving interference pattern results from the finite relaxation time of the nonlinear changes produced in the medium. The necessity for a spatial mismatch between the grating and the pattern to produce gain, reflects a general principle which states that forced resonant oscillations always proceed with a $\pi/2$ phase delay relative to the periodic exciting force [8].

One of the striking phenomenons in the propagation of laser beams is the apparent high reflectivity of normally transparent materials when powerful pulse lasers are used as excitation beams. The reflected light goes straight back in the direction opposite to the incident beam. The reflectivity is caused by strong dynamic gratings that build up from random fluctuations

by the interaction of the incident and the scattered light. Depending on the dominant type of interaction, gratings of optical phonons (stimulated Raman scattering) [55], gigahertz acoustic sounds (stimulated Brillouin scattering) [56], and temperature (stimulated thermal Rayleigh scattering) [57] are created. The important new aspect of stimulated scattering was discovered by Zel'dovich [9]: in some circumstances the stimulated wave will be nearly phase conjugate to the incident wave. This could be of relevance for atmospheric or complex optical communication channels. Phase conjugation was demonstrated experimentally utilizing various nonlinear optical processes, e.g., three-wave mixing, four-wave-mixing, stimulated Brillouin scattering [8-10, 80]. In photorefractive materials, large photo-induced refractive index changes can be induced even with low cw laser beams [12, 13, 16]. This allows cancellation of beam distortion with simultaneous amplification [8, 10, 16, 17].

The aim of the second part of the thesis is to study the photorefractive analogue of backscattering, also called stimulated diffusion backscattering (SDS) due to the diffusion nature of dynamic photorefractive gratings [77, 82-102]. We demonstrated the advantages of the reflection photorefractive gratings. The best demonstrated sensitivity in visible region, using self-pumped phase conjugate mirror in a ring configuration, was $5x10^{-4}$ J [101]. This motivates us to improve this value using SDS geometry. The sensitivities of double phase conjugate mirror, in which two mutually incoherent beams become phase conjugate to each other [109-114], and loop-based geometry [89, 101] were also measured. The experimental demonstrations in the papers [84-104] are convincing enough to pay special attention to photorefractive geometries, which utilize reflection gratings. The second part of the thesis also deals with the material parameters, a very important aspect in the study of photorefrective gratings.

Comparisons between photorefractive and photoanisotropic materials

Both photorefractive crystals and photoanisotropic materials have high photosensitivity and a large dynamic range (amplitude of the refractive index or absorption grating). Both materials can be used for writing permanent or dynamic gratings. Most photorefractive

crystals do not have polarization recording ability. Both materials can be utilized for recording a large number of holograms via angular multiplexing in the thick samples.

Doped polymers have several advantages over inorganic photorefractive crystals: compositional flexibility, ease of sample preparation, low fabrication cost, much larger sample size, high resolution capabilities. However, there are also several disadvantages. Because the direct structure changes of the dye molecule in polymeric environment could result in irreversible side reactions, dye-doped polymer materials usually show some fatigue after many thousands of recording cycles. This may be solved by replacing with a new sample since organic materials are inexpensive. However, in some cases realignment and reexposure of the new sample may be required.

The gratings recorded in a dye-doped polymer films are local because the dye molecules doped in polymer are not free to move whereas photorefractive materials are nonlocal. This lead to an inability to obtain two-wave mixing gain in photoanisotropic materials like in photorefractive crystals [13].

Since the state of the optical field produces a modulation of the material properties at the molecular level, and diffusion of the photoactive species is minimal, the resolution capabilities of photoanisotropic materials is extremely large, in the range of several thousand lines per millimeter [44]. In spite of some disadvantages of doped polymer materials comparing with photorefractive crystals their development and their use is a great interest from fundamental and practical point of view. In addition, organic materials can produce high diffraction efficiency holograms based on photoinduced index changes. Photoanisotropic materials also have large storage capacity due to the availability of large sample sizes. Photoanisotropic materials have several disadvantages as well in comparison to photorefractive crystals. In addition to fatigue, and no gain, the doped polymer materials show thermal blooming under excitation by high power laser beams. The high diffraction efficiency is difficult to achieve at the recording wavelength due to high absorption. Although we could use a different laser wavelength to reduce significantly the absorption. Time constants of

photoanisotropic materials are on the order of seconds to minute whereas photorefractive crystals are on the order of seconds or less (see later thesis).

The results of this comparison show that the study and use of photoanisotropic and photorefractive materials is of great practical interest. These materials could be used in different kinds of applications, which are not intersecting.

Outline of Thesis

This thesis contains six chapters, an introduction and a conclusion. In the introduction we present our motives why we are interested in photoanisotropic and photorefractive materials.

Chapter 1 is an introduction to the first part of the thesis. In this chapter we describe reversible photoisomerisation mechanism. This enables us to understand why the photoanisotropic materials are sensitive to both intensity and polarization modulation. We then described a Disperse Red 1/ poly(methyl methacrylate) recording system that we fabricated in our laboratory and present its experimental data. Cross modulation experiments to study the photoinduced dichroism are described and the discussion of photophysical mechanisms involved is given. The presence of intermediate excited (triplet) states is suggested.

Chapter 2 is the basis to understand dynamic photoanisotropic holography and the core of the first part of the thesis. In this chapter we used azo-dye doped polymer materials to record thin and thick holograms. There exist several publications on photoanisotropic materials [19-21, 31-46] but there are only applicable for transmission gratings and experimental demonstration for thick photoanisotropic gratings is missing. We theoretically and experimentally demonstrated that one could successfully store (using a linearly and an elliptically polarized beams) and reconstruct an elliptical polarization state of light using photoanisotropic materials. Linearly and elliptically polarization for recording was used for

the first time. We also showed in this chapter that macroscopic optical chirality might be generated in photoanisotropic materials with a proper choice of excitation beam polarization state. This is, to our knowledge, the first demonstration of a light-induced chirality in solid phase polymer film. Theoretical analysis for thick reflection gratings was also made.

Chapter 3 describes linear diffraction gratings that provide strongly asymmetric diffraction without surface modulation. The spatial phase shift of the refractive index grating relative to the absorption grating is the origin of asymmetric behavior. Thick shifted gratings were theoretically studied in [27]. This motivates us made the theory for thin gratings and asymmetric diffraction was experimentally demonstrated.

Chapter 4 is an introduction to physics of stimulated diffusion backscattering. General analysis of the problem itself, its current state-of-art and future prospects as well as a scientific motivation of this research are elucidated in this chapter. We also performed a comparative analysis of the reflection and transmission gratings to emphasize potential advantages of the reflection gratings.

In chapter 5 the material parameters of $KNbO_3$ crystal (SDS gains, response rate, polarization characteristics, dark decay effects, Debye radius etc.) are measured using a new technique. We believe that optimal crystal, its processing procedure as well as a dopant and its density is still unknown even for visible range. These parameters are evidently very important in each particular geometry.

Chapter 6 is devoted to experimental study of conditions to arrange self-starting phase conjugation via reflection photorefractive gratings. We experimentally demonstrated that SDS geometry has the minimal energy required to switch on the phase conjugation reflection in comparison of other known phase conjugate geometries, giving the SDS effect a considerable practical value. Detailed experimental investigations of double-phase-conjugation geometry at double-loop reflection gratings were made.

Finally, the conclusion contains general summary of the whole thesis.

PART I

LASER INDUCED GRATINGS IN AZO-DYE-DOPED POLYMER MATERIALS

In the first part of the thesis we studied azo-dye-doped polymer materials. In the following chapters we discussed:

1. photophysical mechanisms responsible for refractive-index and absorption changes in azo-dye-doped polymer materials.
2. thin and thick photoanisotropic gratings.
3. linear diffraction gratings that provide strongly asymmetric diffraction without surface modulation.

CHAPTER 1

AZO-DYE-DOPED POLYMER MATERIALS FOR DYNAMIC HOLOGRAPHY

The development of photonic technologies is directly related to the question of the availability of optical materials that are adapted for each particular application. For instance, erasable optical storage, image-processing systems, like holographic correlators and interferometers, require materials with reversible photo excitation mechanisms, that would allow the recording of dynamic holograms. In this chapter we study reversible photochemical materials using dye molecules suspended in polymer hosts that could record dynamic holograms. The self-developing refractive index changes in dye-doped or dye-attached polymer materials, in particularly azo-dye-doped polymer systems make them promising candidates for the fore-mentioned applications (because of the large photoinduced birefringence) [19-21, 31-54]. The mechanism of photoanisotropic recording in azo-dye-doped polymer material is based on orientationally dependent photoisomerization of dye molecules that may be macroscopically described in terms of photoinduced linear dichroism and linear birefringence. In this chapter we will discuss the photoisomerization mechanisms of dye-molecules. Further we will propose a technique for the fabrication of thick photosensitized polymer materials for real-time (self-developing) holographic applications. Cross modulation experiments to study the photoinduced dichroism are then described and the discussion of photophysical mechanisms involved is given.

1.1 Photoisomerization of azo-dye molecules in a polymeric environment

The photoanisotropic materials (anisotropy may be induced by light), which we investigated, are azo-dye-doped polymer systems. Azo compounds are organo-nitrogen derivatives with the characteristic double-bonded –N=N– functionality and the general formula $R-N=N-R'$ where R and R' can be the same or different groups. The presence of a double bond generally has profound consequences on the stereochemistry: it gives the molecule more rigidity and restricts the number of possible forms. The main feature is the coplanarity of all atoms adjacent to a double bound as well as of the double bounded nitrogen atoms themselves [59]. Azobenzene derivatives have two geometric isomers: the trans or E and the cis or Z forms, which have different absorption spectra [18, 37-39]. The isomerization reaction is a light- or heat- induced interconversion of the two isomers. As the trans form is generally more stable, by about $50kJ \cdot mol^{-1}$ in the case of azobenzene [18], the thermal isomerization is generally in cis⇒trans direction. Light induces transformation in both directions. The photoisomerization reaction begins by raising molecules to electronically excited states and nonradiative decay brings them back to the ground state, in either the trans or the cis form. From the cis form molecules revert to the trans form by two mechanisms: thermal spontaneous relaxation or the reverse photoisomerization. Photoinduced isomerism of azobenzene proceeds with large structural change as reflected in the dipole moment and change in geometry. The isomerization involves a decrease in the distance between the para carbon atoms in azobenzene form from about 9.0Å in trans-form to 5.5Å in cis-form and the local contraction may be even longer [37-39]. Figure 1.1 presents the isomerization reaction for Disperse Red 1 (DR1) azo dye (pseudo-stilbene type molecule, as classified by Rau [18]).

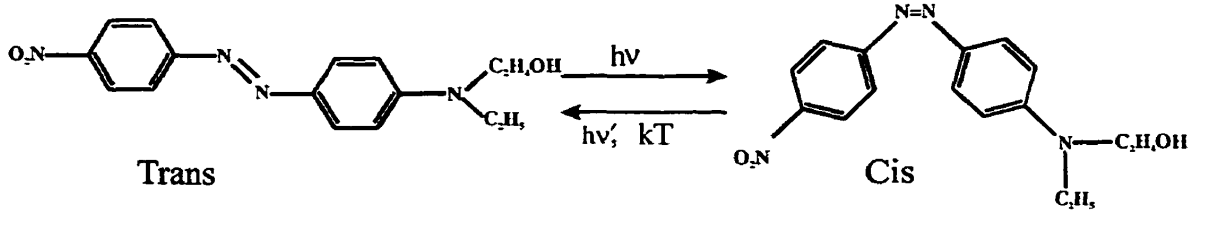

Figure 1.1 Trans⇔cis isomerization of Disperse Red 1 (DR1) azo-dye molecule.

The azobenzene compounds are characterized by a low-lying n-π^* state and a large energy gap between this and the next higher π-π^* state. Two mechanisms may occur during the photoisomerization of azobenzene derivatives : one from the high energy π-π^* transition, which lead to rotation around the –N=N– double bond, and the other from the low- energy n-π^* transition, which induces isomerization by means of inversion through one of the nitrogen nuclei [18]. Both mechanisms lead to the same eventual conformational change of the molecule, but for each the process of photoisomerization is different [18]. For the photoisomerization of azobenzenes it has been shown that the free volume needed for inversion is lower than for rotation. Both mechanisms have their weaknesses: neither of them can rationalize the temperature dependence of the quantum yields of isomerization. There seems to emerge the concept of independent singlet and triplet isomerization pathways. The isomerization mechanism is not yet fully understood.

The molecular geometrical change that occurs in the photoisomerization process may lead to a loss of the initial orientation of the molecules after a complete trans⇒cis isomerization cycle. These reversible processes (isomerization and reorientation) provide the basis for dynamic holographic recording [37-39, 32-34, 47-49].

1.2 Model of photoisomerization

The probability of a highly anisotropic azo-dye molecule (when starting from isotropically distributed trans isomers) absorbing a photon and subsequently isomerizing depends on the orientation of the molecule's principal absorption oscillator axis with respect to the polarization direction of the acting light. This probability is proportional to the cosine square of the angle between the transition dipole moment and the polarization direction of the acting light (linearly polarized beam burns a hole in the orientational distribution due to the selectivity of the molecular excitation (angular hole burning)). Thus the dye molecules that have their transition dipole moment parallel to the direction of polarization of the pump beam present the highest probability for pumping and for undergoing trans⇒cis isomerization. This process changes the orientation of the molecules (orientational redistribution). Both angular

hole burning and orientational redistribution lead to an anisotropic distribution of the azo-dye molecules within the photoisomerization reaction. The isotropy can be restored by rotational diffusion that can be described by the rotational Brownian motion resulting from thermal agitation [37,47-49].

Anisotropic molecular absorption cross section as a function of the orientation of the incident polarized light with respect to the molecule is [37-39] (see Fig.1.2):

$$\sigma = \sigma_{\parallel}(a^2\cos^2\theta + b^2\sin^2\theta\cos^2\phi) + \sigma_{\perp}[(a^2\sin^2\theta + b^2(1-\sin^2\theta\cos^2\phi)] \qquad (1.1)$$

where $\sigma_{\parallel}$ and $\sigma_{\perp}$ are the absorption cross sections of the molecule for the light polarized parallel and perpendicular, to its principal axis, and θ and ϕ are the polar coordinate angles of the molecule. a and b, defined to be along X and Y, are the major and the minor half-axes of the optical elliptically polarized wave. M. Dumont, Z. Sekkat et al. modeled the photoisomerization and photoinduced reorientation of azobenzene molecules for a linearly polarized and circularly polarized excitation beams (assuming the trans and cis molecules characterized by uniaxial molecular polarizability tensors (cigar-shaped molecules)) [47-49]. Their model assumes that only the trans isomer absorbs significantly at the excitation wavelength (see absorption spectrum for DR1). I will just remind some interesting physical and mathematical aspects of the two-level model assuming that a linearly polarized light excites the azo-dye molecules (Fig.1.3):

$$\begin{aligned}
\frac{dn_T(\Omega)}{dt} &= -I\phi_{TC}(\sigma_{\parallel}\cos^2\theta + \sigma_{\perp}\sin^2\theta)n_T(\Omega) + \frac{1}{\tau_C}\iint Q(\Omega'\rightarrow\Omega)n_C(\Omega')d\Omega' + D_T\vec{R}^2 n_T(\Omega,t) \\
\frac{dn_C(\Omega)}{dt} &= I\phi_{CT}\iint n_T(\Omega')(\sigma_{\parallel}\cos^2\theta + \sigma_{\perp}\sin^2\theta)P^{TC}(\Omega'\rightarrow\Omega)d\Omega' - \frac{n_C(\Omega)}{\tau_C} + D_C\vec{R}^2 n_C(\Omega,t)
\end{aligned} \qquad (1.2)$$

where $P^{TC}(\Omega'\rightarrow\Omega)$ and $Q(\Omega'\rightarrow\Omega)$ are the probabilities that a molecule will rotate in the redistribution processes of trans⇒cis optical transition and cis⇒trans thermal recovery

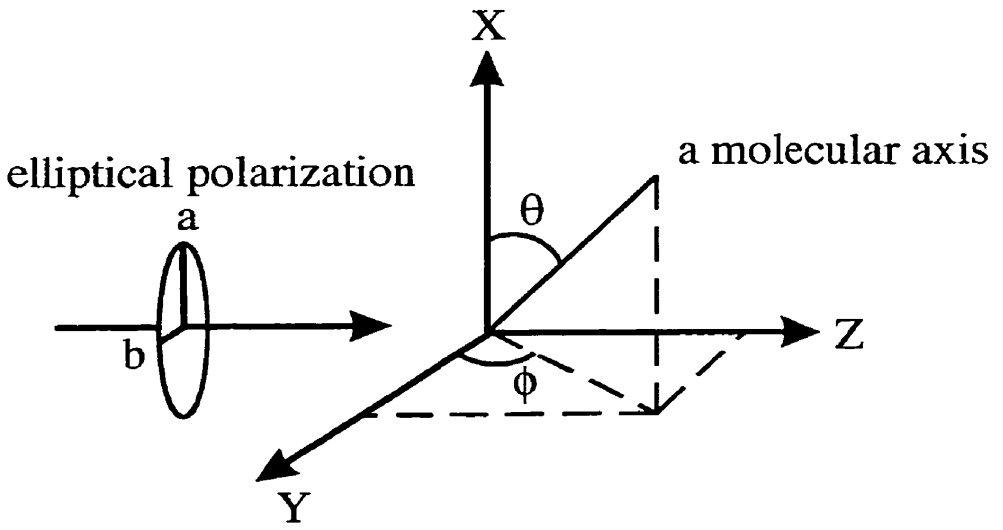

Figure 1.2 Spatial orientation of dye molecule with respect to the polarization state of the exciting light.

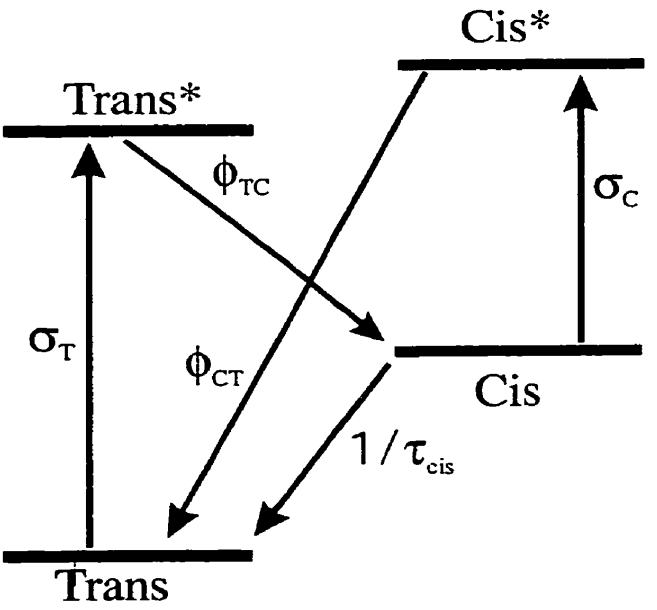

Figure 1.3 Simplified model of the molecular states

respectively. $D_C(D_T)$ is a constant of diffusion for the cis (trans) configuration which is given by the following Einstein relation: $D=kT/\xi$ where ξ is the friction coefficient that depends on the viscosity of the polymer and on the molecular shape. $\bar{R}$ is the rotational operator. $n_T(\Omega)d\Omega$ and $n_C(\Omega)d\Omega$ are the number of trans and cis molecules whose representative moment of transition along the long axis is present the elementary solid angle $d\Omega$ around the direction $\Omega(\theta, \phi)$ respectively. The normalizations are:

$$\begin{aligned}
&\iint n_T(\Omega)d\Omega = N_T \\
&\iint n_C(\Omega)d\Omega = N_C \\
&N_C + N_T = N \\
&\iint P^{TC}(\Omega' \rightarrow \Omega)d\Omega' = 1 \\
&\iint Q(\Omega' \rightarrow \Omega)d\Omega' = 1
\end{aligned} \tag{1.3}$$

where N_T and N_C are the molecular densities at the trans and cis states, respectively, and N is the total molecular density. When we consider that the molecular distribution is axially symmetric (the symmetry axis is defined by the direction of the irradiating light polarization), it is obvious that the Legendre polynomials are the eigenfunctions for the system [49]. The general formalism given by Eq.1.2 can be simplified when Legendre formalism is used, and the variations of the cis and trans populations are given by the variations of their expansion parameters T_n and C_n, respectively. Neglecting the expansion parameters above the third order, the fourth Legendre polynomial moment is only a small correction to the second Legendre polynomial moment that gives the anisotropy one obtain [49] the system of equations (T_0 is proportional to the average absorbance, T_2 is proportional to the linear dichroism):

$$\begin{aligned}
&\frac{d^2T_0}{dt^2} + \left(\frac{1}{\tau_C} + \Gamma + I_T + \frac{11}{7}I_T\right)\frac{dT_0}{dt} + \left(\left[\frac{1}{\tau_C} + I_T\right]\left[\Gamma + \frac{11}{7}I_T\right] - \frac{4}{5}I_T^2\right)T_0 = N\frac{1}{\tau_C}\left(\Gamma + \frac{11}{7}I_T\right) \\
&\frac{d^2T_2}{dt^2} + \left(\frac{1}{\tau_C} + \Gamma + I_T + \frac{11}{7}I_T\right)\frac{dT_2}{dt} + \left(\left[\frac{1}{\tau_C} + I_T\right]\left[\Gamma + \frac{11}{7}I_T\right] - \frac{4}{5}I_T^2\right)T_2 = -\frac{2}{5}N\frac{1}{\tau_C}I_T
\end{aligned} \tag{1.4}$$

where Γ is a constant of rotational diffusion and $I_T = \frac{\sigma_{//}^T + 2\sigma_{\perp}^T}{3}\phi_{TC}I$. We assume that the rates of both the cis⇒trans thermal reaction and the diffusion in the cis and trans forms are very small ($\frac{1}{\tau_C} \approx \Gamma \approx 0$) and we obtain for a linearly polarized excitation beam the solution (if the irradiating light is turned at the time t=0):

$$\begin{aligned} T_2(t) &\approx 0.2N\exp(-2.23I_T t) - 0.2N\exp(-0.35I_T t), \\ T_0(t) &\approx 0.33N\exp(-2.23I_T t) + 0.61N\exp(-0.35I_T t) \end{aligned} \tag{1.5}$$

with $C_2(t) = -P_2^{TC}T_2(t)$ and $C_0(t) = N - T_0(t)$. P_2^{TC} is given by the second-order Legendre polynomial of cosα: $P_2^{TC} = \frac{1}{2}(3\cos^2\alpha - 1)$, by assuming that the long molecular axis of each azo molecule is reoriented by the same angle α when experiencing a trans⇒cis photoisomerization with equiprobability for all the direction commencing from the initial orientation. The boundary conditions are: $T_2(t=0)=C_2(t=0)=T_2(t=\infty)=C_2(t=\infty)=0$, $C_0(t=0)=0$, $T_0(t=0)=N$. These analytical solutions show, through simple expressions, that the molecular alignment and the population change evolve with two time constants that mainly depend on the irradiating light intensity I and the quantum yield ϕ_{TC} of the direct trans⇒cis photoisomerization.

When the irradiating light is switched off at the photostationary state of the irradiation, the thermally activated back cis⇒trans reaction that depends on the cis lifetime mainly governs the population change from the cis form to the trans form. Furthermore, the rotational diffusion that depends mainly on diffusion coefficients of the azo molecule in both the trans form and cis form only governs to dichroism evolution. The cis diffusion is considered only for the cis lifetime because after this time all molecules are relaxed to the trans form. Taking I=0 one obtain [49]:

$$N_C = N_C^0 \exp(-\frac{t}{\tau_C}), \qquad N_T = N - N_C^0 \exp(-\frac{t}{\tau_C}),$$
$$C_2 = C_2^0 \exp(-\frac{t}{\tau_C}), \qquad T_2 = T_2^0 + Q_2 C_2^0 \left[\exp(-\frac{t}{\tau_C}) \right] \tag{1.6}$$

where N_C^0 is the cis molecular density at the moment where the irradiating light is switched off; T_2^0 and C_2^0 are the second order expansion parameters of the trans and cis molecular distributions at this moment. Note that the motion of dye molecules in a polymeric surrounding is much more severely restricted than in liquid solvents leading to a significantly slower thermal relaxation than in liquid solvents.

It should be also noted that molecular relaxation in polymeric films has shown multiexponential behaviors, so a more rigorous theory of the complex relaxation phenomenon that appears in polymer films should combine the Brownian relaxation with a free-volume theory [61].

1.3 Cross modulation experiment in thick dye-doped polymer films

1.3.1 Fabrication of thick PMMA sheets

Experimental results presented here correspond to the poly(methyl methacrylate) (PMMA) films obtained by means of free-radical polymerization of methylmethacrylate (MMA) and doped with the Disperse Red 1 (DR1) azo dye (Merck, Ltd.), for which the formula is presented in Fig.1.1. The absorption spectrum for the DR1-doped PMMA system is presented in Fig.1.4. The polymerization technique is a process in which a liquid monomer (or prepolymer) is polymerized inside a suitable mold. In general, polymerization is chemically initiated, and the curing or polymerization step usually takes place when the mold is heated in an oven or a water bath. For our technique, the mold consisted of two sheets of plate glass

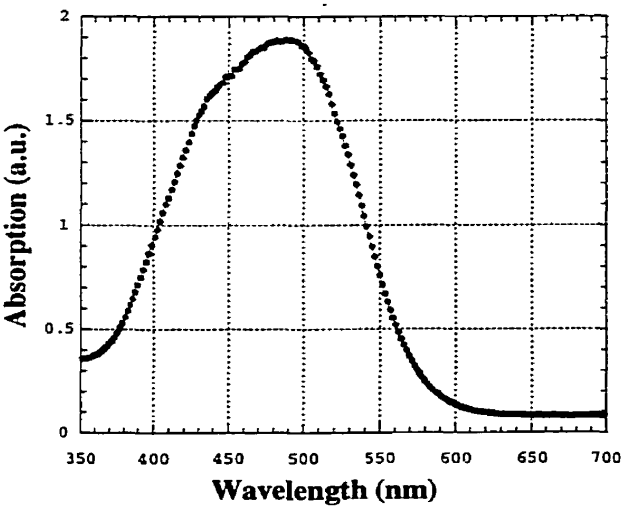

Figure 1.4. Absorption spectrum of the DR1 dye in the poly(methyl methacrylate) (PMMA) matrix.

separated by a gasket (Tygon tubing) and held together by spring clips. The mixture of the monomer-initiator (freshly distilled methyl methacrylate and 2.2′-azobisisobutyronitrile (AIBN)) along with the DR1 dye, was poured into the mold, the gasket was adjusted to seal the inlet, and the assembly was placed in thermostate-regulated water at 60°C for 6-8h. After this step, the polymerization yield was approximately 90-95%. Our aim was complete polymerization (> 99%); thus we next heated the molded sheet in an oven at temperatures higher than the glass-transition temperature. Typical thicknesses above 2 mm with the concentration 5 wt%-7.5wt% DR1-doped PMMA films were obtained [50].

1.3.2 Cross modulation study

If a dye-doped polymer material is excited with polarized light, the resulting change in the optical properties is anisotropic: i.e. the material becomes dichroic and birefringent. Photoinduced anisotropic effects in the azo-dye-doped polymer systems, as we discussed above, are due to selective trans-cis isomerization and reorientation of dye molecules in the direction perpendicular to the polarization of incident light. We studied the photoinduced dichroism in our samples. For this purpose, we used cross modulation setup [50]. Namely, the

probe beam was normally incident on the polymer film. Its transmission was modulated by a linearly polarized pump beam. Two geometries with parallel and crossed polarizations of the pump and the probe beams were studied. The polymer film was in the vertical plane, while all wave vectors were in the horizontal plane. The pump beam (from Ar-ion laser λ=488 nm) intersected the signal beam (from He-Ne laser λ=632.8 nm) at the plane of the film with an interbeam angle of 10° in air. The intensity of the probe and the excitation beams were I_p=2.5 mW/cm^2 and I_e=930 mW/cm^2, respectively. Figure 1.5(a) and figure 1.5(b) show the change in the transmission of the signal beam polarized perpendicular and parallel to the polarization direction of the pump beam, respectively. As one can see, the dynamic behavior is quite different for these two interaction geometries. Thus in both cases the probe transmission demonstrated a rapid jump (increase) when the pump was switched on. However, the value of the jump is slightly different. We have approximately 1,56 % variation in the cross polarized geometry and 0,92 % variation in the parallel polarization geometry. Further kinetics was different too. Thus the detected transmission variation was smooth and monotone in Fig. 1.5(a). We obtained in this case a significant decrease of transmission in the steady-state excitation regime. Another transient jump (decrease) of transmission was observed (in both geometries, Fig.1.5) when the excitation beam was switched off. The corresponding values of transmission variations were 1,46 % and 1,28 % for the cross- and the parallel-polarization geometries, respectively. The initial transmission was then slowly established. As we mentioned above, the transmission of the probe beam with parallel polarization demonstrated the same rapid jumps when the excitation was switched on and switched off. However, the probe's transmission at steady-state excitation regime was almost the same as before excitation (Fig.1.5 (b)).

1.3.3 Discussion of cross modulation results

It was established that the trans form of azo dyes has relatively small absorption at the probe wavelength [21, 49, 50]. This absorption is stronger in the dye's cis isomer form. In addition, the trans form has positive dichroism, that is, a higher absorption when the light polarization is parallel to the dipole moment of the dye (almost parallel to the dye molecule's

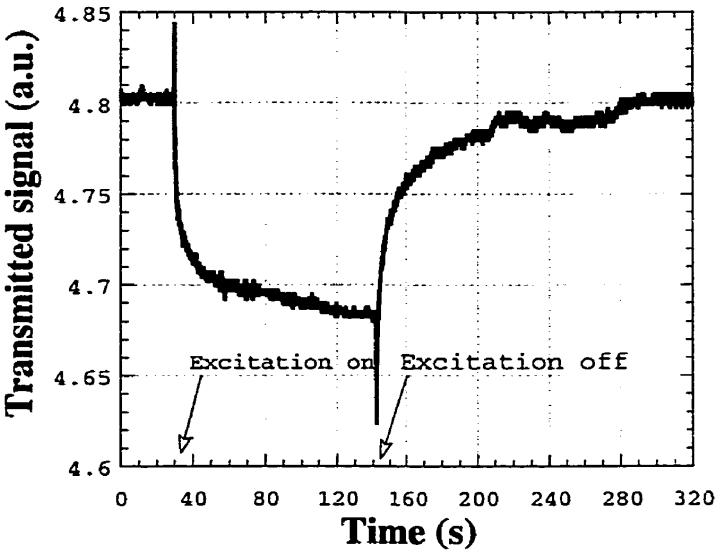

(a)

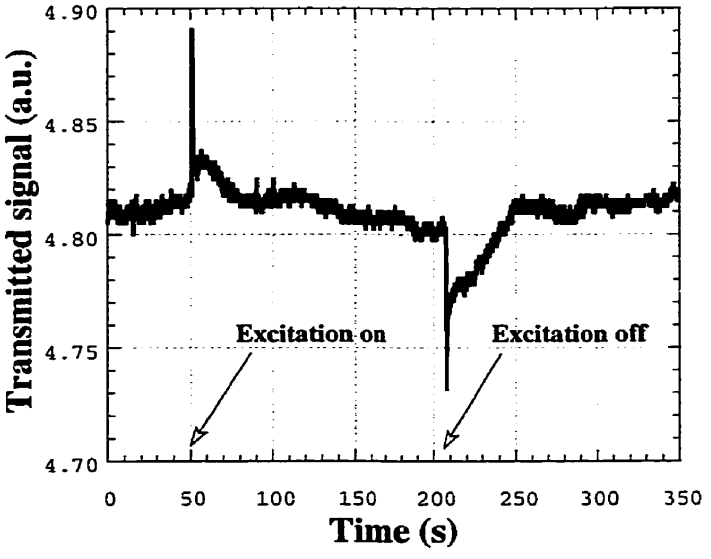

(b)

Figure1.5 Transmission of the plane polarized probe beam through the DR1/PMMA polymer sample under illumination by a linearly polarized excitation beam; (a) crossed polarizations, (b) parallel polarizations.

geometrical axis). As we already noted the trans form is the more stable one at room temperature [18] and we have more trans than cis forms in the dark. Taking this into account, we can interpret the cross-modulation results obtained as follows. The excitation of the trans and the cis populations to excited singlet and mainly triplet (because of the longer lifetimes) states leads to the transient decrease of absorption and thus to the probe transmission increase [the first transient jumps in Figs. 1.5(a) and 1.5(b)]. These exited states should possess a certain dichroism of the probe absorption because we have almost 0,5 % difference of transmission modulation (increase) for two polarization configurations. The further equilibration of populations in the steady-state excitation regime leads to the formation of new cis species and to the reorientation (out of the pump-beam polarization direction) of molecular axes of trans forms. The trans⇒cis isomerization mechanism increases the absorption of the probe beam, thus leading to the decrease of its transmission (fig.1.5(a)). The transmission decrease is more significant for the cross polarized probe (compared with Fig.1.5(b)) because it is accompanied by the reorientation of trans forms, which possess positive dichroism of absorption. Thus the cross polarized probe transmission in the steady state excitation regime is significantly reduced below its initial value.

The second jump (decrease) in the probe transmission (when excitation beam is switched off) should be related to the rapid relaxation of excited molecules from higher (mainly triplet) excitation states to the trans and cis forms that increase the probe absorption (Fig.1.5(a)). Thus the characteristic lifetimes of these states should be less than or at the order of 0.1 sec. This relaxation brings to the increase of absorption for both cross- and parallel-polarized probes (Figs.1.5(a) and 1.5(b)). The further cis⇒trans thermal back relaxation and the orientational equilibration of the trans forms decrease the cross-polarized probe absorption and bring the system to its initial state.

The main difference of the case with parallel polarized signal and pump beams is achieved in the steady-state excitation regime (Fig. 1.5(b)). After the first transient jump the change of the probe transmission is neither smooth nor monotone, showing the presence of different (mutually canceling) mechanisms of the absorption modulation that have approximately the same characteristic times and contributions. We obtain in this case almost

the same transmission in the ground-state and steady-state excitation regimes. This difference from the cross geometry (Fig. 1.5(a)) is due to the dye's reorientation (out of the probe beam polarization) which reduces its absorption. At the same time, the trans⇒cis isomerization increases the probe absorption as in the previous case. Thus the probe absorption modulations due to reorientation and isomerization mutually cancel each other. When the pump is switched off the transmission decreases suddenly (because of the relaxation of molecules from excited triplet states) and then increases back gradually due to the orientational equilibration (which increases the probe absorption) and cis⇒trans thermal relaxation (which decreases the probe absorption).

1.4 Conclusion

In this chapter we presented a new polymerization technique for fabrication of high optical quality thick polymer films. Our results indicate the potential interest represented by the polymerization technique for fabrication of dynamic volume holograms. The data obtained show several important characteristics of the dye behavior in our polymer matrix, which will be used for interpretation of the holographic study results in the next Chapter. First, the thermal cis⇒trans relaxation and orientational equilibration have almost the same characteristic times. Second, the photoisomerization (or angular hole burning) and reorientation have a canceling contribution in the absorption changes (at the probe wavelength). Third, the trans⇒cis photoisomerization takes place via intermediate excited (triplet) states, which have characteristic lifetimes less than 0.1 sec. Finally, rapid transient excitation states should have dichroic absorption at the probe wavelength under excitation by means of a linearly polarized beam.

CHAPTER 2

THIN AND THICK DYNAMIC POLARIZATION GRATINGS

Traditional holography uses the interference phenomenon to record the amplitude and phase of light [1]. Very often in such cases, the polarization state of light remains out of the scope of the recording and reconstruction problems since only parallel polarized components of light may interfere. The complete optical recording *(holography),* including the storage of information about the phase, amplitude and polarization of light, would require the use of a complex (in general, elliptic) polarized reference beam. A light wave, which is a vector field, can be characterized by its intensity and its state of polarization. If two coherent recording elliptically polarized beams intersect they will produce a total light field (a polarization ellipse), which may have different intensity and polarization state from either of two recording beams. Because the phase difference between two recording beams is spatially varying, the polarization ellipse of the total field varies spatially in both in intensity (scalar holograms) and state of polarization (vector holograms). In conventional scalar holography the two recording beams have parallel polarizations i.e. we have only intensity modulation. But if the two recording beams are orthogonally polarized (linear or circular) then the variation of phase difference induces a pure polarization modulation with no intensity modulation which was demonstrated using photoanisotropic materials for the first time by Kakichashvili [40-43].

In this chapter we used azo-dye doped polymer materials to record thin and thick holograms (scalar and vector). We theoretically and experimentally demonstrated that one could successfully store (using a linearly and an elliptically polarized beams) and reconstruct an elliptical polarization state of light using photoanisotropic materials, even if a plane polarized reference beam is used for the recording and readout [52, 53].

2.1 Polarization gratings

2.1.1 Polarization gratings in photoanisotropic materials

We consider the case in which two recording arbitrary (elliptically) polarized plane waves are symmetrically incident in transmission geometry at an angle θ from the normal on a recording medium. These two recording beams form a total vectorial field. The polarization state of this total field is a planar ellipse that spatially varies because the phase between recording beams varies spatially. The influence of such a complex field on the medium may be represented (in the local coordinate system x'Oy') as follows. We suggest that the elliptically polarized light induces dichroism and birefringence (see later) which are proportional to its total intensity $I_0 = \frac{\varepsilon_0 cn}{2}\left(\left\langle E_{x'}^2 \right\rangle + \left\langle E_{y'}^2 \right\rangle\right)$, where $\left\langle E_{x'}^2 \right\rangle = a^2$ and $\left\langle E_{y'}^2 \right\rangle = b^2$ are the energies of the components on major and minor axes of the polarization ellipse, respectively. Note that the major and minor axes of the photoinduced dichroism and birefringence vary spatially. The modulated dielectric constant of the medium (in the local coordinate system x'O y'), may be represented using the Kakichashvili model [40-43] in the following form $\varepsilon_{ij}(r) = \varepsilon_0 + \chi_{ijkl}\delta_{ij}\delta_{kl}E_k E_l^*$, $(i,j,k,l = x', y')$ where χ_{ijkl} is a complex (in the general case) parameter, $\chi_{iiii} = \chi_{\|}$, $\chi_{iijj} = \chi_{\perp}$, $\chi_{\|}$ and $\chi_{\perp}$ are the coefficients of contribution of the parallel and perpendicular polarizations in photoanisotropic refractive index modulation of the medium, ε_0 is the initial complex dielectric constant of the medium before recording the grating. The real part of χ corresponds to a pure phase hologram, while the imaginary part χ corresponds to the absorption hologram. The medium with such spatial distribution of the photo induced anisotropy and dichroism can be described by means of the spatially varying dielectric tensor. We can use a 2×2 spatially varying dielectric tensor instead of 3×3 full tensor, since we have assumed small recording and readout angles. We can choose our local coordinate system to coincide with main axes of the polarization ellipse so that the recorded polarization hologram is given by a dielectric tensor (without circular anisotropy) [41]:

$$\Delta\hat{\varepsilon}_{x'y'} = \begin{pmatrix} \Delta\varepsilon_{x'x'} & 0 \\ 0 & \varepsilon_{y'y'} \end{pmatrix} = \begin{pmatrix} \chi_{\parallel}a^2 + \chi_{\perp}b^2 & 0 \\ 0 & \chi_{\parallel}b^2 + \chi_{\perp}a^2 \end{pmatrix} \tag{2.1}$$

Let us describe the orientation angle between the major axis of the polarization ellipse with respect to the x axis (in laboratory coordinates) by an angle β. The dielectric tensor describing the polarization grating in the laboratory system is: $\Delta\varepsilon_{xy} = R(-\beta)\Delta\varepsilon_{x'y'}R(\beta)$, where R(β) is the rotation matrix:

$$R(\beta) = \begin{pmatrix} \cos\beta & \sin\beta \\ -\sin\beta & \cos\beta \end{pmatrix} \tag{2.2}$$

then we obtain polarization hologram in the laboratory system:

$$\Delta\varepsilon_{xy} = \begin{pmatrix} \Delta\varepsilon_{x'x'} + \Delta\varepsilon_{y'y'} + (\Delta\varepsilon_{x'x'} - \Delta\varepsilon_{y'y'})\cos 2\beta & (\Delta\varepsilon_{x'x'} - \Delta\varepsilon_{y'y'})\sin 2\beta \\ (\Delta\varepsilon_{x'x'} - \Delta\varepsilon_{y'y'})\sin 2\beta & \Delta\varepsilon_{x'x'} + \Delta\varepsilon_{y'y'} - (\Delta\varepsilon_{x'x'} - \Delta\varepsilon_{y'y'})\cos 2\beta \end{pmatrix} \tag{2.3}$$

The orientation angle β is given by:

$$\begin{aligned} \cos(2\beta(x)) &= \frac{J_{xx}(x) - J_{yy}(x)}{a^2(x) - b^2(x)}, \\ \sin(2\beta(x)) &= \frac{J_{xy}(x) + J_{yx}(x)}{a^2(x) - b^2(x)} \end{aligned} \tag{2.4}$$

$J_{ij}(x) = \frac{\varepsilon_0 cn}{2} E_i(x)E_j^*(x)$ (i,j=x,y) is the intensity correlation , where E_x and E_y are the components of the total field $\bar{E}$ along the X and Y axes in the laboratory system. So the recorded polarization grating can be presented as [41, 45, 46]:

$$\Delta\varepsilon = \frac{\varepsilon_0 cn}{2}\begin{pmatrix} \chi_{\|}|E_x|^2 + \chi_{\perp}|E_y|^2 & (\chi_{\|} - \chi_{\perp})\dfrac{E_x E_y^* + E_x^* E_y}{2} \\ (\chi_{\|} - \chi_{\perp})\dfrac{E_x E_y^* + E_x^* E_y}{2} & \chi_{\|}|E_y|^2 + \chi_{\perp}|E_x|^2 \end{pmatrix} \tag{2.5}$$

Polarization coupling is possible because of existence of off-diagonal elements. The polarization grating described by Eq.2.5 can be presented as a sum of four gratings: 2 gratings recorded by parallel-polarized beams

$$\Delta\varepsilon_{paral.} = \frac{\varepsilon_0 cn}{2}\begin{pmatrix} \chi_{\|}|E_x|^2 + \chi_{\perp}|E_y|^2 & 0 \\ 0 & \chi_{\|}|E_y|^2 + \chi_{\perp}|E_x|^2 \end{pmatrix} \tag{2.6}$$

if $\chi_{\|} = \chi_{\perp}$ the diffraction from these gratings will be isotropic. The second pair of gratings recorded by orthogonal polarized beams:

$$\Delta\varepsilon_{orthogonal} = \frac{\varepsilon_0 cn}{2}\begin{pmatrix} 0 & (\chi_{\|} - \chi_{\perp})\dfrac{E_x E_y^* + E_x^* E_y}{2} \\ (\chi_{\|} - \chi_{\perp})\dfrac{E_x E_y^* + E_x^* E_y}{2} & 0 \end{pmatrix} \tag{2.7}$$

These gratings are responsible for polarization coupling and they are recorded only in the case $\chi_{\|} \neq \chi_{\perp}$ i.e. when the anisotropy is induced in the medium.

2.1.2 Thin and thick gratings

We consider the medium containing a phase grating and an absorption grating. The diffraction gratings may be classified into three regimes [22, 23, 26, 27]: Raman-Nath, intermediate, and Bragg regime. The distinction between thin (Raman-Nath regime) and thick (Bragg regime) gratings and corresponding diffraction behavior may be described in terms of

the factor Q' given by $Q' = Q/\cos\theta = 2\pi\lambda L/(\sqrt{\varepsilon_0}\Lambda^2\cos\theta)$ where λ is the vacuum wavelength of the light, L is the medium thickness, $n = \sqrt{\varepsilon_0}$ is the average refractive index, Λ is the grating spacing. This is a geometrical factor; it can be expressed using the definition of the Fresnel length: let us denote the transverse scale of the inhomogeneity of the field as Λ, then by the uncertainty relationship it corresponds to the angular divergence $\Delta\theta \sim \lambda/\Lambda$. The light rays at the distance $L_{fr} \sim \Lambda/\Delta\theta \approx \Lambda^2/\lambda \approx \lambda/(\Delta\theta)^2$ (Fresnel length) extend beyond of the limits of the original homogeneity. At distances $z \le L_{Fr}$ the simple laws of geometrical optics are applicable, while when $z >> L_{Fr}$ diffraction processes become substantial.

Thin gratings have sometimes defined as gratings with Q<<1 ($L << L_{Fr}$) and thick gratings as gratings with Q>>1 ($L >> L_{Fr}$). However the modulation level must also be specified in determining the type of diffraction behavior. If the modulation parameter is sufficiently small, thin grating can be observed even at large values of Q. An exact definition of thin gratings is [26]:

$$\begin{aligned} Q' &= \frac{Q}{\cos\theta} = \frac{2\pi\lambda L}{\sqrt{\varepsilon_0}\Lambda^2\cos\theta} < 1 \\ Q'\gamma &\le 1 \end{aligned} \tag{2.8}$$

where γ is strength of the grating given by $\gamma = \pi\Delta\varepsilon L/(2\lambda\sqrt{\varepsilon_0}\cos\theta)$ for s-polarization, and $\gamma = \pi\Delta\varepsilon L\cos 2\theta/(2\lambda\sqrt{\varepsilon_0}\cos\theta)$ for p-polarization, and $\Delta\varepsilon \approx 2\tilde{n}\Delta\tilde{n} \approx 2n(\Delta n + i\Delta\alpha/(2k_0))$ [8]. An exact definition of thick gratings is [27]:

$$\begin{aligned} Q' &= \frac{Q}{\cos\theta} = \frac{2\pi\lambda L}{\sqrt{\varepsilon_0}\Lambda^2\cos\theta} > 1 \\ \rho &\equiv \frac{Q'}{2\gamma} \ge 10 \end{aligned} \tag{2.9}$$

where $\rho = \dfrac{2\lambda^2}{\Lambda^2\Delta\varepsilon}$ for s-polarization , and $\rho = \dfrac{2\lambda^2}{\Lambda^2\Delta\varepsilon\cos 2\theta}$ for p-polarization.

2.1.3 Thick scalar holograms

Scalar holograms are recorded by two coherent linearly polarized recording beams that are parallel to each other. Scalar recording geometry is probably the most frequently used experimental situation, in which two recording beams are linearly polarized perpendicular to the plane of incidence (s-polarized). The polarization state of the total field remains as same as the recording beams i.e. linear and its direction remains unchanged. The spatially varying phase difference in this case causes only in intensity modulation. The incident intensity modulates spatially the population of the electronic states of the azo-dye molecules, leading to photoinduced anisotropy. This population density grating affects the amplitude of a probing beam and was originally called amplitude grating. According to the Kramers-Kroning relation also a phase contribution exists. Since the rate of photochemically induced transformations depends on light intensity, when a spatially varying intensity pattern incident to the azo-dye-doped polymer system, the intensity variation results in a variation of the extent of isomeric transformations in the sample. This spatially varying nonuniform photochemistry results in a spatial variation of the index of refraction and the absorption coefficient. Because both the index of refraction and absorption coefficient are functions of wavelength then by proper choice of the recording and reconstruction wavelength of the laser we may obtain a good compromise of low absorption, medium sensitivity and large index changes.

First we will consider the case of thick gratings. In this case the higher orders of diffraction do not satisfy the Bragg condition and hence are not excited. Therefore only two waves are present in the volume of the hologram in the process of reconstruction : the reference wave $\vec{E}_R$ and the object wave $\vec{E}_S$ [24]. When the diffraction efficiency is high, we must take into account of the change of amplitude of the reference wave due to outlow of energy into the object wave. The reference beam $\vec{E}_R$ and object beam $\vec{E}_S$ can be represented by Jones vectors (plane waves):

$$\vec{E}_R = \begin{pmatrix} 0 \\ E_{Ry} \end{pmatrix} \exp(i\vec{k}_R \vec{r} - i\omega t); \quad \vec{E}_S = \begin{pmatrix} 0 \\ E_{Sy} \end{pmatrix} \exp(i\vec{k}_S \vec{r} - i\omega t) \tag{2.10}$$

where $\vec{k}_s = k_0 n(-\sin\theta, 0, \cos\theta)$, $\vec{k}_R = k_0 n(\sin\theta, 0, \cos\theta)$, $k_0 \equiv \frac{2\pi}{\lambda_0}$, λ_0 is the wavelength in vacuum and n is the uniform refractive index of the medium. The total electric field amplitude is given by $\vec{E}_T = \vec{E}_S + \vec{E}_R$ and this wave has to fulfill the time-independent vector wave equation:

$$\vec{\nabla} x \vec{\nabla} x \vec{E} - k_0^2 \varepsilon \vec{E} = 0 \tag{2.11}$$

where ε is a complex dielectric tensor given by

$$\varepsilon = \frac{\varepsilon_0 cn}{2} \begin{pmatrix} \varepsilon_0 + \chi_{\parallel} |E_x|^2 + \chi_{\perp} |E_y|^2 & (\chi_{\parallel} - \chi_{\perp}) \frac{E_x E_y^* + E_x^* E_y}{2} \\ (\chi_{\parallel} - \chi_{\perp}) \frac{E_x E_y^* + E_x^* E_y}{2} & \varepsilon_0 + \chi_{\parallel} |E_y|^2 + \chi_{\perp} |E_x|^2 \end{pmatrix} \tag{2.12}$$

That includes the effects of the material refractive index and absorption, and $k_0 = \frac{\omega}{c}$ is the free space wave number. From now on the explicit time dependence exp(-iωt) will be dropped. We can rewrite the Eq.2.11 as

$$\nabla^2 \vec{E} + \vec{\nabla}(\vec{E} \cdot \frac{\vec{\nabla}\varepsilon}{\varepsilon}) = -k_0^2 \varepsilon \vec{E} \tag{2.13}$$

Then for two s-polarized recording beams we obtain [45, 46] :

$$\nabla^2 \vec{E} + k_0^2 (\varepsilon_0 + \chi_{\parallel} I) \vec{E} = 0 \tag{2.14}$$

where the total recording intensity is

$$I = \frac{\varepsilon_0 cn}{2} (E_S E_S^* + E_R E_R^* + E_S E_R^* \exp(i(\vec{k}_S - \vec{k}_R)\vec{r} + E_R E_S^* \exp(i(\vec{k}_R - \vec{k}_S)\vec{r}) \tag{2.15}$$

First, we will consider the case when we readout the recorded grating with a sufficiently weak s-polarized probe. Then we will readout the same grating by p-polarized probe beam when the Bragg condition satisfied in two cases. We will assume that linear absorption is negligible. This assumption is valid because for λ=633nm the azo-dye doped polymer films have practically no absorption (see Fig.1.4, $\alpha \approx 0.04$ mm^{-1}). We recorded the gratings with $I_S=I_R \approx I_0$ (we assume that strength of the grating is small). If we readout the grating with s-polarized probe beam then we obtain (second order derivatives can be neglected applying the slowly varying amplitude approximation):

$$\begin{aligned} \frac{dE_{S\|}}{dz} &= 2i\tilde{\gamma}_{\|} I_0 E_{S\|} + i\tilde{\gamma}_{\|} I_0 E_{R\|} \\ \frac{dE_{R\|}}{dz} &= 2i\tilde{\gamma}_{\|} I_0 E_{R\|} + i\tilde{\gamma}_{\|} I_0 E_{S\|} \end{aligned} \tag{2.16}$$

where $\tilde{\gamma}_{\|} = \gamma'_{\|} + i\gamma''_{\|} = \frac{k_0}{2n}\chi_{\|}$ (taking into account that $\cos\theta \approx 1$) is a complex nonlinear coupling constant where γ' is responsible for photoinduced refractive index change and γ'' is responsible for photoinduced absorption change. The general solution of the differential equation 2.16 has the form :

$$E_{S\|} = C_1 \exp(\xi_1 z) + C_2 \exp(\xi_2 z) \tag{2.17}$$

then using the boundary conditions $E_{S\|}(0) = 0$ and $E_{R\|}(0) = E_{R\|0}$ we obtain the diffraction efficiency :

$$\eta_{\|} = \frac{\left|E_{S\|}(L)\right|^2}{\left|E_{R\|}(0)\right|^2} = \left(\sinh^2(\gamma'_{\|} I_0 L) + \sin^2(\gamma''_{\|} I_0 L)\right)\exp(-4\gamma''_{\|} I_0 L) \tag{2.18}$$

where the first term represents the absorption grating and the second term denotes the phase grating. In this case there are no polarization switching diffraction, since the dielectric

perturbation tensor is diagonal. Considering that the amplitude part of the grating is negligible in our azo-dye-doped polymer films while reading it by a probe beam (λ=633nm) and that the strength of the grating is small ($\gamma''_{\parallel} I_0 L << 1$), then we obtain:

$$\eta_{\parallel} = (\gamma''_{\parallel} I_0 L)^2 = \left(\frac{\pi}{\lambda} \frac{\chi''_{\parallel} I_0}{n} L \right)^2 \tag{2.19}$$

which is similar to the classic Kogelnik results (using $\varepsilon = \varepsilon_0 + 2\Delta\varepsilon \cos \vec{qr}$) [24] .

Now we will consider that we readout the grating by a p-polarized probe beam under Bragg condition. In this case we obtain the following coupled wave equations:

$$\begin{aligned} \frac{dE_{S\perp}}{dz} &= 2i\tilde{\gamma}_{\perp} I_0 E_{S\perp} + i\tilde{\gamma}_{\perp} I_0 E_{R\perp} \cos 2\theta \\ \frac{dE_{R\perp}}{dz} &= 2i\tilde{\gamma}_{\perp} I_0 E_{R\perp} + i\tilde{\gamma}_{\perp} I_0 E_{S\perp} \cos 2\theta \end{aligned} \tag{2.20}$$

then the diffraction efficiency for p-polarized beam is:

$$\eta_{\perp} = \frac{|E_{S\perp}(L)|^2}{|E_{R\perp}(0)|^2} = \left(\sinh^2(\gamma'_{\perp} I_0 L \cos 2\theta) + \sin^2(\gamma''_{\perp} I_0 L \cos 2\theta) \right) \exp(-4\gamma''_{\perp} I_0 L) \tag{2.21}$$

then considering that the amplitude part of the grating is negligible in our azo-dye-doped polymer films while reading it by a probe beam (λ=633nm) and that the strength of the grating is small, then we obtain:

$$\eta_{\perp} = (\gamma''_{\perp} I_0 L \cos 2\theta)^2 = \left(\frac{\pi}{\lambda} \frac{\chi''_{\perp} I_0}{n} L \cos 2\theta \right)^2 \tag{2.22}$$

Finally we obtain that the ratio of the diffraction efficiencies for s-polarized beam and p-polarized beams is:

$$\frac{\eta_{\parallel}}{\eta_{\perp}} = \left(\frac{\gamma'_{\parallel}}{\gamma'_{\perp} \cos 2\theta} \right)^2 = \left(\frac{\Delta n_{\parallel}}{\Delta n_{\perp} \cos 2\theta} \right)^2 \tag{2.23}$$

2.1.4 Thick vector holograms

When two recording beams are orthogonally polarized (vector holograms) then the variation of phase difference induces a pure polarization modulation with no intensity modulation. Fig. 2.1 illustrates recording of vector holograms using two orthogonally polarized beams, horizontal and vertical. The phase difference between two recording beams is $\Delta\phi = 2k_0 x \sin\theta$, where 2θ is the angle between recording beams. When two recording beams have equal intensities then the polarization ellipse of total field changes from linear to circular, orthogonal linear, orthogonal circular, etc. (see Fig2.1 (b)). It should be noted that the polarization ellipse of the total field does not change the directions of its principal axes, but only their ratio. In only linear anisotropy is induced in the material then the regions which illuminated by a circularly polarized beam remain isotropic. In some materials one could induce circular anisotropy. If the polarization hologram is written in the medium with both linear and circular photoanisotropy then all four parameters (intensity, ellipticity, orientation of the major axis and rotation direction) of polarization ellipse of the total field can be recorded [40-43]. However if the photoanisotropic material does not possess the circular photoanisotropic effect which leads to optical activity and circular dichroism, than only the first three parameters of polarization ellipse can be recorded. The information about the rotation direction of the polarization ellipse will be completely lost. From the orientational distribution of excited dye-molecules we will not be able to tell whether it was produced by right- or left-handed polarization ellipse.

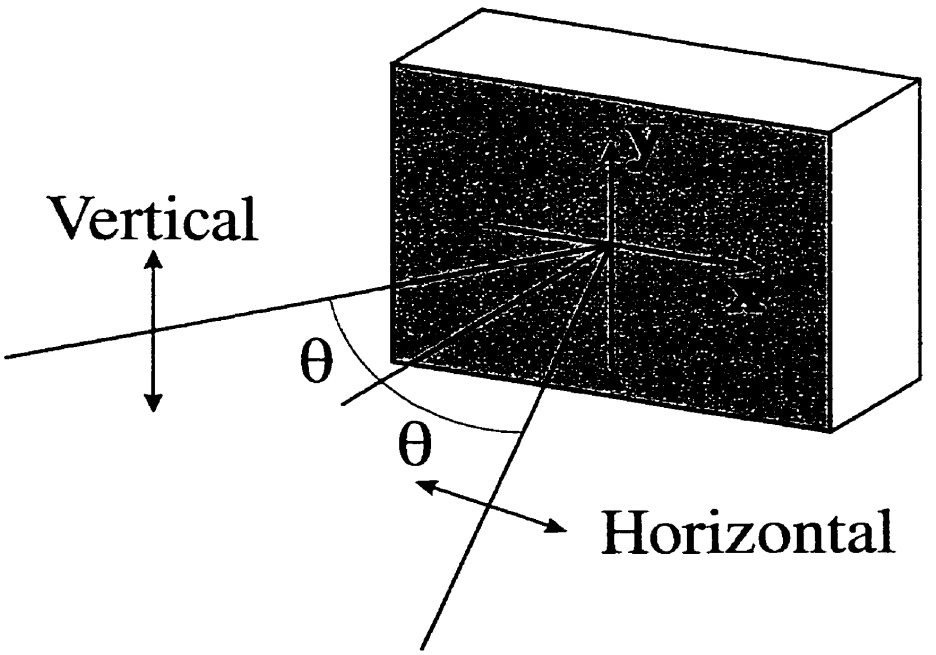

(a)

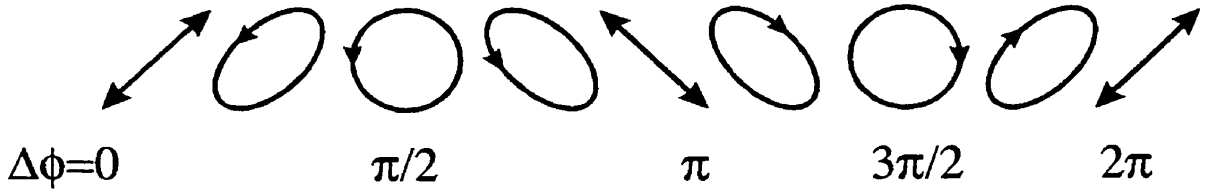

(b)

Figure 2.1 (a) Sketch of the recording geometry; (b) the periodic modulation of light polarization at holographic recording with two orthogonally linearly polarized beams, horizontal and vertical.

The reference beam $\vec{E}_R$ and object beam $\vec{E}_S$ can be represented by Jones vectors:

$$\vec{E}_R = \begin{pmatrix} E_{Rx} \\ 0 \end{pmatrix} \exp(i\vec{k}_R \vec{r} - i\omega t); \quad \vec{E}_S = \begin{pmatrix} 0 \\ E_{Sy} \end{pmatrix} \exp(i\vec{k}_S \vec{r} - i\omega t) \tag{2.24}$$

where $\vec{k}_s = k_0 n(-\sin\theta, 0, \cos\theta)$, $\vec{k}_R = k_0 n(\sin\theta, 0, \cos\theta)$. The total electric field amplitude is given by $\vec{E}_T = \vec{E}_S + \vec{E}_R$. The components of the complex dielectric tensor are

$$\begin{aligned} \Delta\varepsilon_{xx} &= \frac{\varepsilon_0 cn}{2}\left(\chi_{\|}|E_{Rx}|^2 + \chi_{\perp}|E_{Sy}|^2\right) \\ \Delta\varepsilon_{xy} = \Delta\varepsilon_{yx} &= \left((\chi_{\|} - \chi_{\perp})\frac{\varepsilon_0 cn}{2}\frac{E_{Rx}E_{Sy}^* e^{i(\vec{k}_R - \vec{k}_S)\vec{r}} + E_{Rx}^* E_{Sy} e^{-i(\vec{k}_R - \vec{k}_S)\vec{r}}}{2}\right) \\ \Delta\varepsilon_{yy} &= \frac{\varepsilon_0 cn}{2}\left(\chi_{\|}|E_{Sy}|^2 + \chi_{\perp}|E_{Rx}|^2\right) \end{aligned} \tag{2.25}$$

We recorded the grating with two beams of equal intensities. We will readout the recorded grating by reference beam E_{Rx} and we will use the following relations for the filed amplitudes in terms of the intensities and phases:

$$\begin{aligned} E_{Rx} &= \sqrt{\frac{2}{\varepsilon_0 cn} I_{Rx}}\exp(i\phi_{Rx}) \\ E_{Sy} &= \sqrt{\frac{2}{\varepsilon_0 cn} I_{Sy}}\exp(i\phi_{Sy}) \end{aligned} \tag{2.26}$$

therefore, assuming small grating strength which permits take $I_{Rx}=I_{Sy}=I_0$ and using the Eq.2.13 and assuming small angle of recording which enables neglect the term $\vec{\nabla}(\vec{E}\cdot\vec{\nabla}(\ln\varepsilon))$ compared with $k_0^2\Delta\varepsilon\vec{E}$:

$$\frac{dE_{Sy}}{dz} = -i(\tilde{\gamma}_{\parallel} + \tilde{\gamma}_{\perp})I_0 E_{Sy} + \frac{i}{2}(\tilde{\gamma}_{\parallel} - \tilde{\gamma}_{\perp})I_0 E_{Rx}\exp(-i(\phi_{Rx} - \phi_{Sy}))$$
$$\frac{dE_{Rx}}{dz} = -i(\tilde{\gamma}_{\parallel} + \tilde{\gamma}_{\perp})I_0 E_{Rx} + \frac{i}{2}(\tilde{\gamma}_{\parallel} - \tilde{\gamma}_{\perp})I_0 E_{Sy}\exp(i(\phi_{Rx} - \phi_{Sy})) \quad (2.27)$$

The first term in this equation describes the influence of self $\tilde{\gamma}_{\parallel}$ and cross $\tilde{\gamma}_{\perp}$ bleaching on the beam intensity and phase, the second term is responsible for polarization coupling between the recording beams. We see that the p-polarized readout beam E_{Rx} reconstruct the s- polarized signal beam and there is no coupling to E_{Sx} and E_{Ry} from E_{Rx}. Then by symmetry of the recording geometry we see that the s-polarized readout beam E_{Ry} will reconstruct the p-polarized signal beam E_{Sx}. Under the boundary conditions $E_{Rx}(0)=E_{Rx0}$, $E_{Ry}(0)=0$, $E_{Sx}(0)=0$, $E_{Sy}(0)=0$ and assumptions $\Delta\phi = \phi_{Rx} - \phi_{Sy} = \phi_{Rx0} - \phi_{Sy0}$ the solutions of Eq.2.27 are found to be:

$$E_{Sy}(z) = E_{Rx0}\exp(i\Delta\phi)\frac{e^{i\frac{(\tilde{\gamma}_{\parallel}-\tilde{\gamma}_{\perp})}{2}I_0 z} + e^{-i\frac{(\tilde{\gamma}_{\parallel}-\tilde{\gamma}_{\perp})}{2}I_0 z}}{2i}\exp(i(\tilde{\gamma}_{\parallel} + \tilde{\gamma}_{\perp})I_0 z) \quad (2.28)$$

we see that reading the grating by a p-polarized beam we generate s-polarized beam i.e. the polarization direction is switched by $\frac{\pi}{2}$. The diffraction efficiency is given by:

$$\eta = \frac{|E_{Sy}(L)|^2}{|E_{Rx}(0)|^2} = \left[\sinh^2\left(\frac{(\gamma'_{\parallel} - \gamma'_{\perp})}{2}I_0 L\right) + \sin^2\left(\frac{(\gamma''_{\parallel} - \gamma''_{\perp})}{2}I_0 L\right)\right]\exp(-2(\gamma''_{\parallel} + \gamma''_{\perp})I_0 z) \quad (2.29)$$

considering that the amplitude part of the grating is negligible in our azo-dye-doped polymer films while reading it by a probe beam (λ=633nm) and that the strength of the grating is small, then we obtain :

$$\eta = \frac{((\gamma''_{\parallel} - \gamma''_{\perp})I_0 L)^2}{4} = \left(\frac{\pi}{\lambda}\frac{(\chi''_{\parallel} - \chi''_{\perp})}{2n}I_0 L\right)^2 \quad (2.30)$$

we see that photoanisotropy permits the coupling between the two orthogonally polarized beams. The coupling is impossible in the case $\tilde{\gamma}_{\parallel} = \tilde{\gamma}_{\perp}$.

2.2 Experimental results

2.2.1 Experimental set-up and conditions

The experimental setup we used for holographic characterization of the azo-dye-doped polymer films is schematically represented in Fig. 2.2. We used Disperse Red 1 (DR1) doped poly(methyl methacrylate) (PMMA) film with thickness L=1mm obtained by free-radical polymerization technique (see Ch.1) which had good optical quality over the whole surface. Two linearly polarized coherent beams, obtained from a CW Argon ion laser (operating at 488 nm, P=8.3mW), were crossed (at 2θ=10 degrees in air) at the plane of the polymer film to form intensity or polarization spatial modulation, when their polarizations were parallel and perpendicular, respectively. The half-wave plate $\lambda/2$ placed on the path of one of the recording beams (the E_1) was used to fulfill these two recording conditions. The overlapping spot diameter at the polymer film was 2.5 mm. The linearly polarized probe beam with waist smaller than the waist of the recording beams was obtained from a 11 mW power He-Ne laser operating at 632.8 nm ($I=180mW/cm^2$). The second half-wave plate $\lambda/2$ (at the probe beam path) was used for rotation of its polarization plane to study the anisotropy of diffraction for the scalar recording case. Two pairs of lenses (f-f and F-F) were used to find angular selectivity and Bragg angle. A mirror (M) was fixed at the rotation stage in the focal plane of one of the lenses f, the second lens f was placed at distance L from the first lens, where L is the twice of the focal length of the lens f. The sample was placed at the focal plane of the second lens f. Thus, the rotation of the stage changed the incidence angle of the probe beam at the film, keeping the probe beam spot at the same place. The second mirror and the F-F system provided the same operation for the first order of probe beam diffraction, keeping the diffracted spot at the photodetector (PD) surface. The diaphragm D was used for noise level reduction.

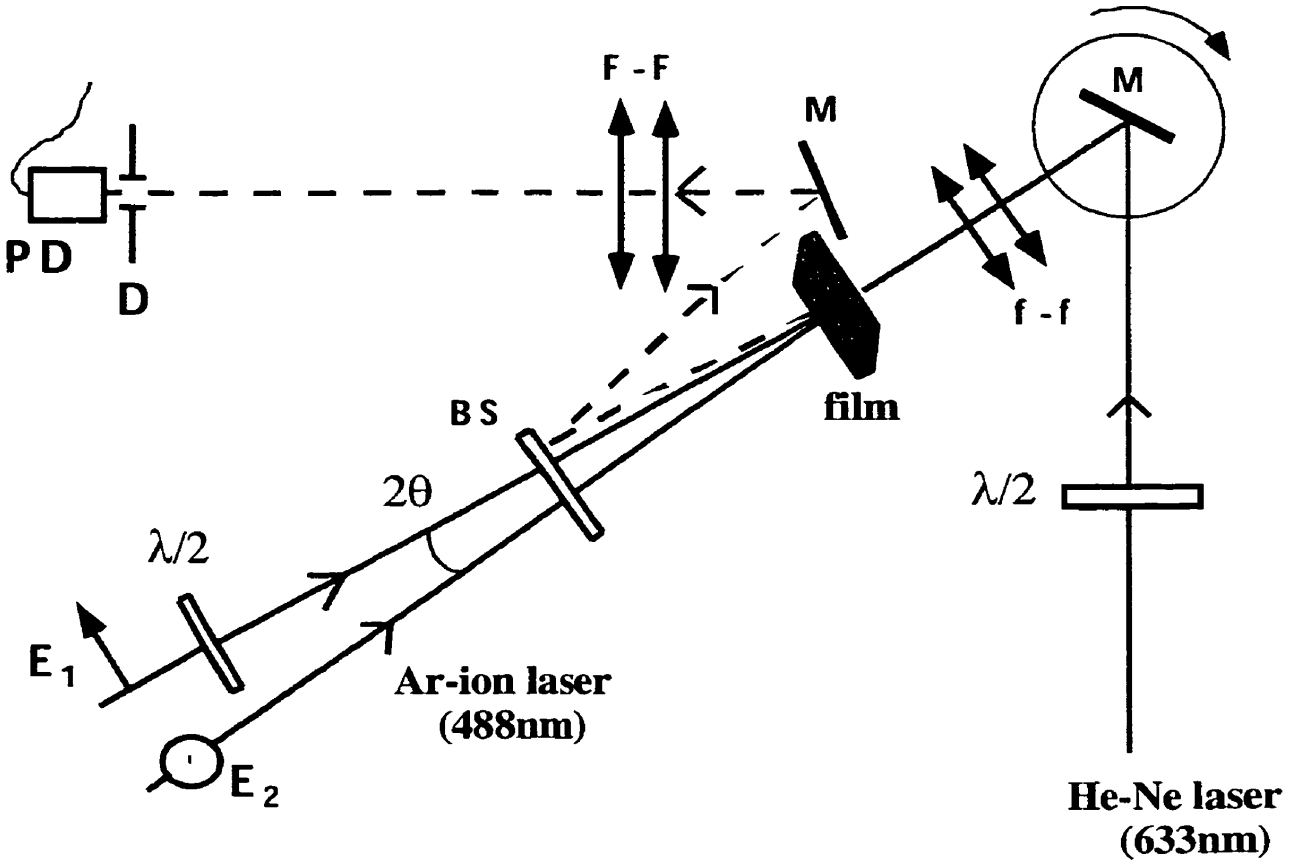

Figure 2.2 Experimental setup for holographic characterization of DR1-doped PMMA films. E1 and E2- recording beams from a CW Argon ion laser (operating at 488 nm); 2θ - angle between recording beams (10 degrees in air); λ/2 - half wave plates; BS - beam splitter; M – mirrors; f-f (and F-F) - the 4f (and 4F) systems for adjusting Bragg angle; D – diaphragm; PD - photodetector.

2.2.2 Intensity gratings (scalar holograms)

We recorded the dynamic gratings with two parallel linear polarized excitation beams with intensities I_1=I_2=170 mW/cm^2. Thus, the intensity of the total light field was modulated in space while its polarization was uniform. We recorded thick gratings i.e. the conditions of Eq.2.9 was satisfied, namely $Q' \approx 257 > 1$ and $\rho \approx 2 \cdot 10^3 > 10$. Both intensity and polarization dependent photoexcitation mechanisms could be used here to create refractive index and absorption periodic modulations. Figure 2.3 illustrates the diffraction signal (in arbitrary units) as a function of exposure time. Taking into account the losses due to absorption and reflection at both surfaces of the sample, it is preferable to define the diffraction efficiency as the ratio of the first order diffracted probe beam intensity to the intensity of the transmitted beam at normal incidence when the sample was unexposed to recording beams. The maximum diffraction efficiency reached at steady state excitation regime was $\eta = 0.23\%$ (reading with the He-Ne laser wavelength which is outside of the absorption band) which corresponds to $\Delta\phi_{\|} = 0.03\pi$ $(\Delta n_{\|} \approx 10^{-5})$ from Eq.2.19. Two graphs were obtained when the polarization of the He-Ne laser beam was parallel (filled circles, marked by $\|$) and perpendicular (open squares, marked by $\perp$) to the polarization of recording beams. One can see a strong anisotropy of diffraction efficiency. For perpendicular polarization from Fig.2.3 and using Eq.2.23 we obtain $\Delta n_{\perp} = \frac{\Delta n_{\|}}{2.15}$. Reasons for such anisotropy may be explained in terms of refractive index and absorption modulation. As it was shown in the chapter 1 (see the fig. 1.5 (b)), the absorption of the probe beam (having parallel with the excitation beam polarization) is lightly changed since the dye reorientation and trans-cis isomerization mechanisms mutually cancel the probe beam absorption changes. At the same time, the changes of the real part of the azo-dye-doped polymer film refractive index are not compensated due to the different distances of the absorption lines of the *trans* and *cis* forms of DR1 from the probe wavelength. In addition, the dielectric susceptibility change due to reorientation of a cigar-shaped molecule is more significant for the probe beam polarization that is parallel to the excitation beam rather than for the one that is perpendicular to it [19-20, 31-39]. This is because the DR1 dye molecules have positive dichroism (no gain) and the most efficient reorientation takes place for molecules whose principal axis are initially parallel to the pump polarization [19, 20, 34].

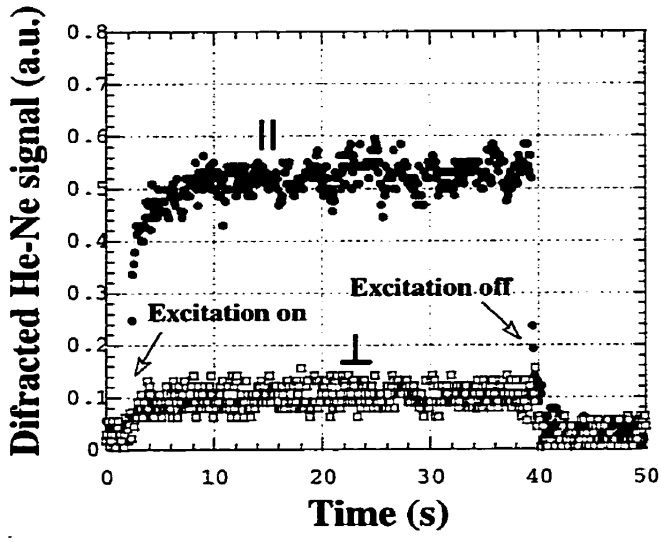

Figure 2.3 Diffraction signal of the probe beam in the case of scalar holograms. Filled circles and open squares correspond to probe polarization, parallel and perpendicular to the excitation beam polarizations, respectively.

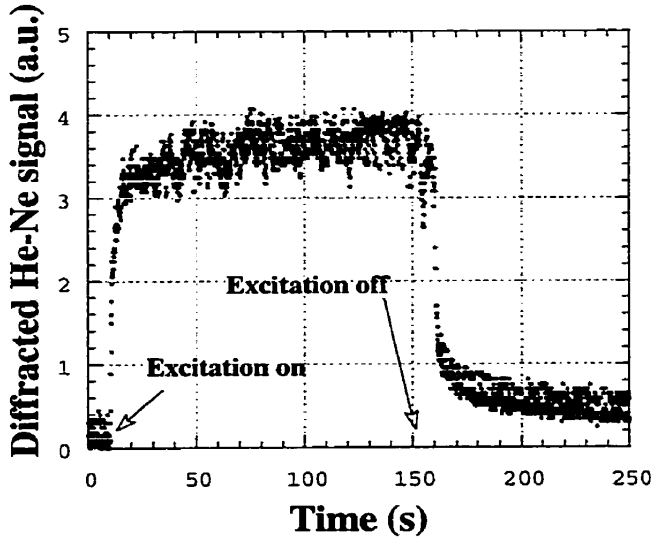

Figure 2.4 Diffraction signal of the probe beam in the case of polarization gratings (vector holograms).

The probe beam (which has polarization perpendicular to the excitation beam polarization) detects absorption modulation (spatially periodic increase of absorption) in the steady state excitation regime (see the fig. 1.5(a)), seeing amplitude gratings, which are less efficient. In addition, the same molecular reorientation leads to smaller refractive index modulation for perpendicular-polarized probe beam [34]. The values of the refractive index are $n_{\|} > n$ and $n_{\perp} < n$, and $|n_{\perp} - n|$ is smaller than $|n_{\|} - n|$. This explains the dependence of the diffraction efficiency on the readout He-Ne laser beam polarization. The angular selectivity of holograms was qualitatively tested by rotation of the mirror that was fixed on the rotation stage under continued exposition by Argon laser beams. The angular selectivity of recorded gratings is about 0.8 degrees.

2.2.3 Polarization gratings (Vector holograms)

We recorded thick polarization gratings ($Q' \approx 257 > 1$ and $\rho \sim 10^3 > 10$, see Eq.2.9) with two orthogonally polarized (vertical and horizontal) beams, with intensities I_1=I_2=170 mW/cm^2. The intensity of the total light field was thus uniform in space while its polarization state was periodically modulated. Both dye reorientation and angular selective photoisomerization may contribute in the excitation. Figure 2.4 illustrates the diffraction signal (in arbitrary units) as a function of the exposure time. The graph shows a monotone increase and stabilization of the probe beam diffraction signal when the excitation beams were switched on, and a monotone decrease of diffraction when the excitation beams were switched off. One can see that the intensity of the diffracted signal decreases to a non-zero stationary value, which indicates some memory effect. The maximal value obtained for the diffraction efficiency η at steady state excitation regime was η = 0.38% while reading by He-Ne laser beam (633nm, see Fig.1.4). This value corresponds to $\Delta\phi = 0.039\pi$ or $n_{\|} - n_{\perp} = 2.5 * 10^{-5}$. The induced birefringence is greater than any of the differences $n_{\|} - n$ and $n_{\perp} - n$ (see section 2.2.2) because the concentration of the molecules along the polarization direction of the recording light diminishes and along the perpendicular direction increases. From values of

diffraction efficiencies for different cases we obtain: $|n_{\parallel} - n_{\perp}| = 2.5|n_{\parallel} - n|$ and $|n_{\parallel} - n| \approx 2.15|n_{\perp} - n|$.

The significant difference of characteristic relaxation times in scalar and vector holograms excitation conditions could be explained by diffusion phenomena. Namely, the fast relaxation in the case of scalar recording may be related to the presence of intensity gradients. This supposes some relaxation mechanisms that can be described by diffusion model [14], thus depending upon the spatial scale of the intensity modulation. For example, diffusion of the heat, excited dye or polymer chains could be the origin of rapid grating relaxation.

2.3 Analysis of the recording and reconstruction of the polarization state of light in Disperse Red 1 (DR1) doped cellulose acetate polymer film

2.3.1 Theoretical analysis

The geometry of our experiment is schematically illustrated in Fig.2.5 [53, 54] . Two coherent beams of equal intensity (the reference and the signal beams) obtained from a cw Ar-ion laser are used for holographic recording. The reference beam is plane polarized (along y axis) while the object beam has an elliptical polarization. Both beams are propagating in the xz plane and the photoanisotropic film is placed in the xy plane. The reference beam $\vec{E}_R$ and object beam $\vec{E}_S$ can be represented by Jones vectors:

$$\vec{E}_R = \begin{pmatrix} 0 \\ E_{Ry} \end{pmatrix} \exp(i\vec{k}_R \vec{r} - i\omega t); \quad \vec{E}_S = \begin{pmatrix} E_{Sx}\cos\theta \\ E_{Sy}\exp(i\phi) \end{pmatrix} \exp(i\vec{k}_S \vec{r} - i\omega t) \qquad (2.31)$$

where $\vec{k}_s = k_0 n(-\sin\theta, 0, \cos\theta)$, $\vec{k}_R = k_0 n(\sin\theta, 0, \cos\theta)$, $k_0 \equiv \frac{2\pi}{\lambda_0}$, λ_0 is the wavelength in vacuum and n is the uniform refractive index of the medium.

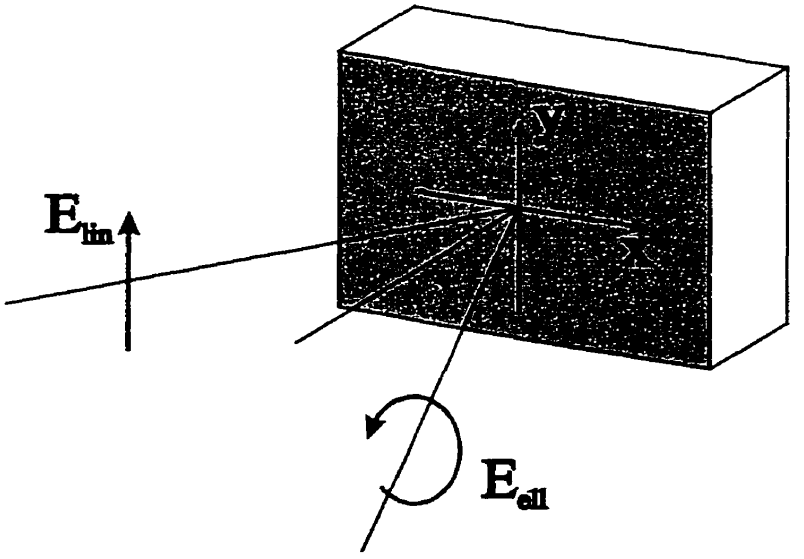

Figure 2.5 Sketch of the recording geometry

The corresponding Jones vector of the total field is given by:

$$\bar{E}_T = \bar{E}_S + \bar{E}_R = \begin{pmatrix} E_x \\ E_y \end{pmatrix} = \begin{pmatrix} E_{Sx}\cos\theta e^{-i\delta} \\ E_{Ry}e^{i\delta} + E_{Sy}e^{i(\phi-\delta)} \end{pmatrix} \exp(-i\omega t + ikz\cos\theta) \qquad (2.32)$$

where E_x and E_y are the components of the total field E_T along the x and y axes in the laboratory system xOy and $\delta \equiv x\,k_0 n \sin\theta$. We shall make an approximation assuming that the cross angle 2θ between beams is small, so that the polarization ellipse lies almost in the xy plane (orthogonal to the recording beams wave vectors, see section 2.1). Note that both the intensity and the state of polarization of the total field varies spatially. Namely, the y component of the reference beam $\vec{E}_R$ forms two gratings with x and y polarization components of the object beam $\vec{E}_S$. The first grating is recorded due to the modulation of polarization and the second one due to the modulation of intensity. These two gratings are shifted relative to each other by the phase ϕ. With aforementioned assumption of small angle between beams, we can represent these changes as periodic modulations, which vary spatially

along the x axis as a function of the angle δ (which is equal to one-half phase difference between two recording beams).

The influence of such a complex field on the medium may be represented using a 2×2 spatially varying dielectric tensor Eq. 2.1 (see section 2.1) We assume that $\Delta n', \Delta n'' << n$, where $\Delta n'$ and $\Delta n''$ represent the amplitudes of modulation of the real and imaginary parts of the complex refractive index of the medium, respectively. Then the Jones matrix that describes the complex transmittance of the medium may be represented as $\tilde{M} = \tilde{M}_0 + \Delta\tilde{M}$, where $\tilde{M}_0$ is a complex (uniform) transmittance at the initial state and $\Delta\tilde{M}$ is the modulated part of the matrix. Using Eq.2.1 we obtain the Jones matrix in the laboratory system that describes the periodically modulated part of the matrix:

$$\Delta\tilde{M}_{diffr} = \frac{ik_0 L}{2n}\frac{\varepsilon_0 cn}{2} e^{ik_0 nL} * \begin{pmatrix} \chi_\perp \left(E_{Ry} E^*_{Sy} e^{-i(\phi-2\delta)} + E^*_{Ry} E_{Sy} e^{i(\phi-2\delta)}\right) & \frac{\cos\theta(\chi_\parallel - \chi_\perp)}{2}\left(E^*_{Ry} E_{Sx} e^{-i2\delta} + E^*_{Sx} E_{Ry} e^{i2\delta}\right) \\ \frac{\cos\theta(\chi_\parallel - \chi_\perp)}{2}\left(E^*_{Ry} E_{Sx} e^{-i2\delta} + E^*_{Sx} E_{Ry} e^{i2\delta}\right) & \chi_\parallel \left(E_{Ry} E^*_{Sy} e^{-i(\phi-2\delta)} + E^*_{Ry} E_{Sy} e^{i(\phi-2\delta)}\right) \end{pmatrix} \quad (2.33)$$

As we can easily see that this grating consists of two gratings which are shifted by phase ϕ : the first grating recorded by two s-polarized beams (y-polarized beams) and the second two orthogonally polarized beams, E_{Ry} and E_{Sx}. We shall further assume that the conditions of Eq.2.8 are satisfied that is the following range of the parameters $Q' = 2\pi\lambda L/(n\Lambda^2 \cos\theta) < 1$ and $\gamma = (\pi\Delta\tilde{n}L)/(\lambda\cos\theta) << 1$ (so that the condition $Q'\gamma \le 1$ is satisfied). The conditions mentioned above would allow us to consider only the directly transmitted E_0 (the 0 order) and the ± 1-order diffracted beams $E_{\pm 1}$ [64, 65]. Then, we can represent the output field as $E_{out} = \tilde{M}E_R$, which will be generated when the same reference beam E_R (that was used for recording) is incident on the film. We obtain the E_{out} performing the corresponding multiplication and separating the angularly deviated and non deviated (0 order) terms:

$$E_0 \propto C\begin{pmatrix}0\\ E_{Ry}\end{pmatrix}e^{i\delta} \tag{2.34}$$

$$E_{-1} = C\frac{|E_{Ry}|^2}{2}\begin{pmatrix}(\chi_{\|}-\chi_{\perp})E_{Sx}\cos\theta\\ 2\chi_{\|}E_{Sy}\exp(i\phi)\end{pmatrix}e^{-i\delta} \tag{2.35}$$

where $C = ik_0L\varepsilon_0 ce^{ik_0nL}/4$. It is easily seen that the directly transmitted light has the same polarization as the reference beam. The polarization of the elliptically polarized object beam may be reconstructed (in E_{-1}) if the following condition is satisfied:

$$\chi_{\|} = -\chi_{\perp} \tag{2.36}$$

The diffraction efficiency in the –1-st order diffraction beam is given by:

$$\eta_{-1} = \frac{|E_{-1}|^2}{|E_{Ry}|^2} = \left(\frac{k_0L}{2n}\right)^2\left(\frac{(\chi_{\|}-\chi_{\perp})^2}{4}I_R I_{Sx} + (\chi_{\|})^2 I_R I_{Sy}\right) \tag{2.37}$$

if we used circularly polarized beam for recording and $\frac{\varepsilon_0 cn}{2}|E_{Sx}|^2 = \frac{\varepsilon_0 cn}{2}|E_{Sy}|^2 = \frac{\varepsilon_0 cn}{2}|E_{Ry}|^2 = I_0$ then we obtain:

$$\eta_{-1} = \left(\frac{\pi L}{\lambda n}I_0\right)^2\left(\frac{(\chi_{\|}-\chi_{\perp})^2}{4} + (\chi_{\|})^2\right) \tag{2.38}$$

which is in agreement with Eq.2.19 and Eq.2.30. Another interesting feature of our holograms is their capacity to efficiently distinguish left and right circularly polarized light [3]. Thus, if the hologram was recorded with a right circularly polarized object beam ($\phi=\pi/2$ and $E_{Sx}=E_{Sy}$) then the readout of the hologram by a left circularly polarized object beam gives $E_{+1} \approx 0$

(under condition $\chi_{\perp} = -\chi_{\parallel}$ and the angle between recording beams is small cosθ≈1). If we readout the grating with a circularly polarized beam, the same as the recording beam, then we obtain the following equation :

$$E_t = C\frac{|E_S|^2}{2}E_{Ry}\begin{pmatrix}\chi_{\parallel} - 3\chi_{\perp}\\ 3\chi_{\parallel} - \chi_{\perp}\end{pmatrix}e^{i\delta} \tag{2.39}$$

i.e. the condition of reconstruction is:

$$\chi_{\parallel} = 3\chi_{\perp} \tag{2.40}$$

Let us now consider the photochemical mechanisms that could satisfy the condition (2.26). Physically, this condition means that refractive index changes must be of opposed direction (bipolar [67]) along the major and minor axes of excitation light's polarization. This is a well-known situation when the medium is composed by anisotropic molecular units that may be reoriented when being photoexcited. This is the case of liquid crystals [67], dichroic dye containing polymers [19]. We have chosen an azo-dye-doped polymer materials which satisfy to condition of 2.26 to realize our polarization holograms.

2.3.2 Experiment

We have fabricated samples from cellulose acetate doped with DR1 azo-dye [51-53]. The cellulose acetate with an average molecular weight of 30,000 and containing an average of 2.4 acetyl groups per repeat unit, was obtained commercially (from Eastman Kodak Company). The glass transition temperature T_g, as measured by a differential scanning calorimeter, is 192°C for the pure polymer and 171°C for samples doped with 7.5% (by weight) DR1. Polymer films were prepared by dip coating. Cellulose acetate (10.00 g) and DR1 (0.750 g) were dissolved together in 100.00 mL of 1,4-dioxane. Ultra clean glass substrates were dipped into the homogeneous solution at a rate of 50 mm/min, and withdrawn at 15 mm/min. After drying the samples, we obtained high-optical-quality films (with uniformity and low scattering) of cellulose acetate with a thickness of 4 μm.

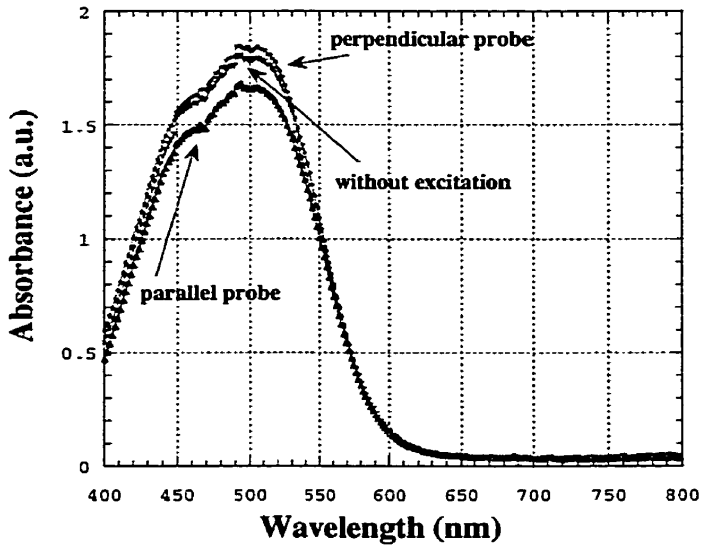

Figure 2.6 Ground state and photoexcited anisotropic absorption of the polymer film. The absorption of the perpendicular polarized probe beam is increased while the absorption of the parallel polarized probe is decreased confirming the bipolar response of the medium.

Time resolved absorption study of this compound (in excited and ground states) have shown, that the resonant photoexcitation (for example, at 514 nm) of DR1 dye leads to efficient trans→cis isomerization. Multiple cycles of trans→cis photo isomerization and cis→trans thermal and photoisomerization lead also to the reorientation of dye molecular axes. Both excitation mechanisms depend upon the light polarization and intensity, and both of them lead to the induction of strong birefringence in our compound. In addition, their relative contribution in the complex refractive index modulation changes with time. A simple experiment was performed to verify the possibility of bipolar excitation of the medium. The excitation was made with a plane polarized beam and spectral modifications were detected with probe beams having parallel and perpendicular (with respect to the excitation field) polarizations. Before the irradiation the absorption spectra for the film are identical for parallel and perpendicular directions. After 30 min of irradiation by a vertically polarized Verdi laser beam (λ=532nm, I=68mW/cm^2), we observed that the absorbance decreases in the parallel direction and increases in the perpendicular direction, see Fig.2.6 [19, 31-36, 51-52]. From

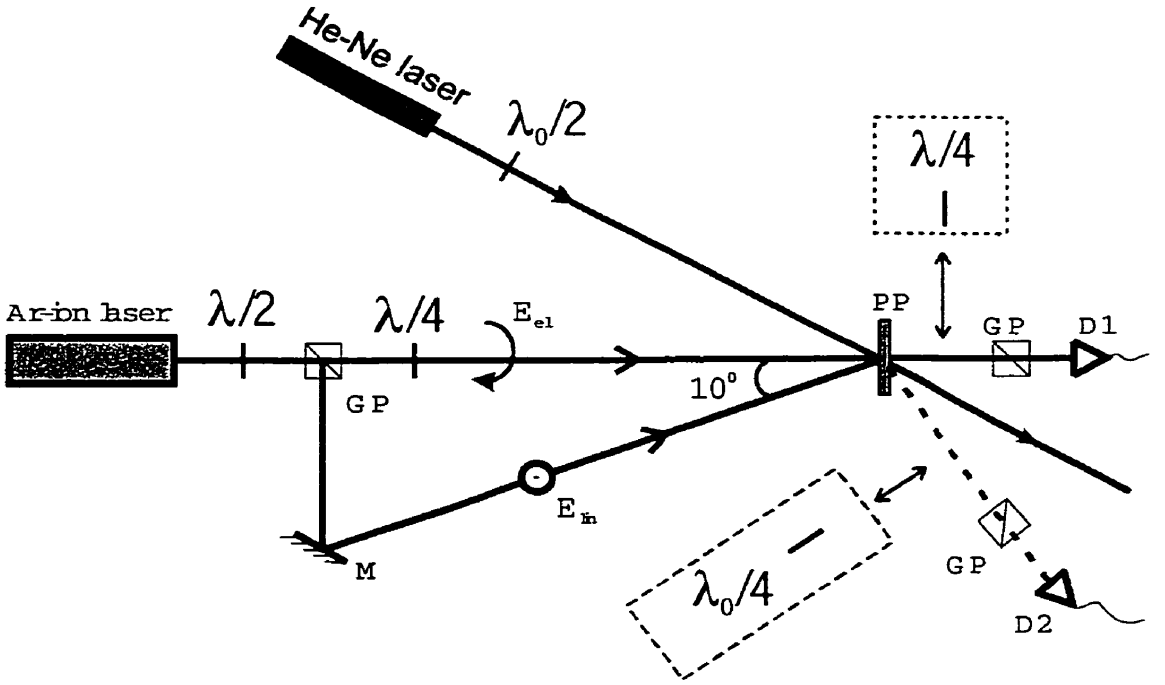

Figure 2.7 The experimental setup. The cw Ar-ion laser provides a plane polarized beam (at 514 nm). GP's, Glan prism; PP, photosensitive polymer sample; M, mirror; Eel, elliptically polarized object beam; Elin, linearly polarized reference beam; D1 and D2, photodetectors. The index 0 is used to distinguish wave plates for the He-Ne probe beam (at λ=632.8 nm).

this data one can optimise the wavelength to be used for the best matching with the condition that we have derived above.

The experimental setup of holographic recording was simple (Fig.2.7): a cw Ar-ion laser that provides linearly polarized emission (at 514 nm) was used for recording (the total coefficient of absorption $\alpha L \approx 1.5$). The output beam from the laser was divided into two beams (reference and object) by a Glan prism (GP). Rotating the $\lambda/2$-plate controls the intensity ratio in both arms. The two beams were crossed on the photosensitive polymer compound by means of a mirror. A $\lambda/4$ plate was introduced into the path of the object beam (initially horizontally polarized) to transform it into an elliptically (or circularly) polarized beam. The angle 2θ between two beams was 10 degrees in air. The recording light intensities were $I_{lin}=I_{circ}=0.2$ W/cm^2. He-Ne laser was also used to probe the grating at the wavelength $\lambda=632.8$ nm. The wavelength of the He-Ne laser was outside from the dye's absorption band, and its influence on the grating was relatively small. To analyse the polarization state of the diffracted and/or transmitted object beams, some

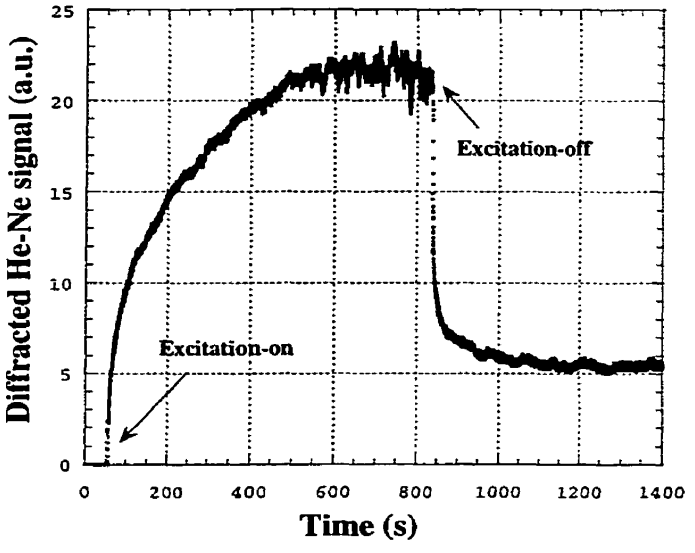

Figure 2.8 Illustration of the diffraction signal (growth, stabilization and partial relaxation) of the He-Ne laser as a function of the exposure (by argon ion laser) time.

additional elements (Glan polarizers (GP) and detectors D1, D2) were installed into the paths of these beams.

Our measurements were performed in the following manner: We first recorded the holographic grating (using Ar-ion laser beams) and then studied its partial relaxation (removing both recording beams and using the He-Ne probe beam) to identify the time of stabilization. This process took of several minutes (see Fig.2.8). The residual diffraction efficiency in this regime was of the order of η=0.1 % which corresponds to $\Delta\phi = 0.02\pi$ or $\Delta n \approx 1.6 \cdot 10^{-3}$. Then we studied the grating using the attenuated Ar-ion reference beam or the He-Ne probe beam. The polarization state of the circularly polarized object beam (before the grating was recorded) is shown in Fig.2.9 (triangles). The polarization state of the -1st-order diffracted beam (the reconstructed object beam) generated by readout of the grating with a linearly polarized reference beam is shown by the circles (Fig.2.9). As one can see, the circularity of the diffracted beam is very close to the circularity of the object beam used for recording. The -1st-order diffracted beam has the same-handed circular polarization as the recording circularity. To verify this we installed a $\lambda/4$ plate in the path of the reconstructed

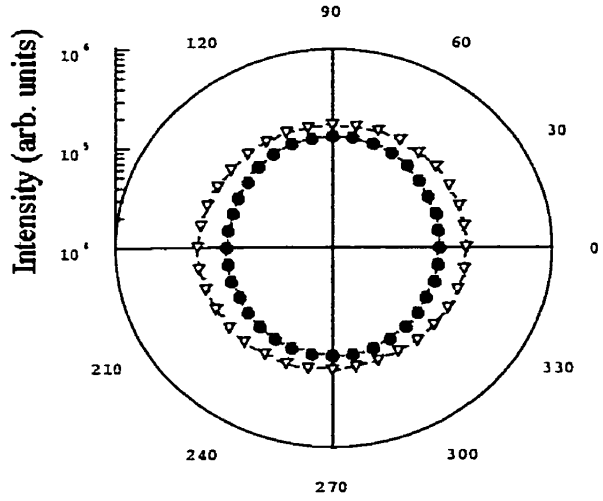

Figure 2.9 Polarization states of recording (open triangles) and reconstructed (filled circles) object beams (argon-ion laser beams are used for both measurements).

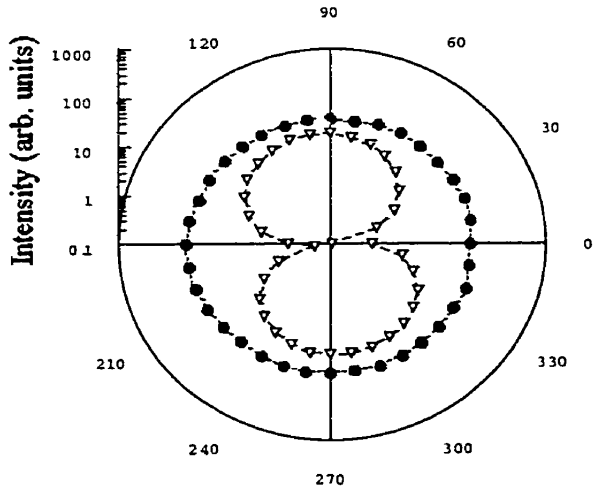

Figure 2.10 Polarization states of reconstructed object beam before (circles) and after (triangles) the plate $\lambda_0/4$. Argon-ion laser beams are used for recording and the He-Ne probe beam is used for reconstruction.

beam, which allowed us to transform the diffracted circularly polarized beam into a linearly polarized beam. Thus, we could compare the reconstructed plane-polarized beam with the initial direction of the beam polarization on the object arm to confirm that two polarization components of the diffracted beam indeed are shifted by a $\pi/2$ phase.

The recorded grating was relatively thin, and higher-order diffractions were also observed. The grating parameters were $Q' \approx 0.8$ and $\gamma \approx 2.5 \cdot 10^{-2}$. We then tried to readout the grating using a plane polarized He-Ne probe beam. The polarization of the probe beam was parallel to that of the green reference beam. As one can see in Fig.2.10 (circles), the diffracted beam was circularly polarized. The same experiment with a $\lambda/4$ plate (for λ=632.8 nm) was performed. The $\lambda/4$ plate transformed the reconstructed beam polarization into plane polarization (Fig.2.10, triangles), showing that the diffracted beam polarization components are also shifted by a $\pi/2$ phase.

Finally, we verified the polarization discrimination of our holograms with respect to the object beam. The hologram was recorded with a right circular polarized object and plane polarized reference beam. Then the readout of the hologram by a left circularly polarized beam diffracts 10 times weaker (by intensity) in +1-order than the right circularly polarized readout. This also confirms the predictions of our theory.

2.4 Macroscopic light-induced chirality in a bulk azo-dye-doped polymer

2.4.1 Holographic reflection gratings in dye-doped polymer materials

Helical structures are often observed in nature. Very often the molecular packing interaction is chiral (i.e. mirror asymmetric) as in cholesteric or twisted-nematic liquid crystals. It is known that in isotropic films of azobenzene polymers linearly polarized beam induces a reorientation of the chromophores perpendicular to the direction of polarization of the light (see chapter 1). This induces an optical anisotropy. However the material remains

optically achiral. We show in this section that macroscopic optical chirality may be generated in such systems with a proper choice of excitation beam polarization state [68].

In this section we will consider the case of thick reflection gratings i.e. the conditions of Eq.2.8 are satisfied. We will use two counter-propagating beams to record the grating. These beams may be represented by Jones vectors :

$$\vec{E}_R = \begin{pmatrix} E_{Rx} \\ E_{Ry} \end{pmatrix} \exp(-i\vec{k}_R \vec{r} - i\omega t); \quad \vec{E}_S = \begin{pmatrix} E_{Sx} \\ E_{Sy} \end{pmatrix} \exp(i\vec{k}_S \vec{r} - i\omega t) \tag{2.41}$$

where $\vec{k}_s = k_0 n(0,0,1)$, $\vec{k}_R = k_0 n(0,0,1)$, $k_0 \equiv \frac{2\pi}{\lambda_0}$, λ_0 is the wavelength in vacuum and n is the uniform refractive index of the medium. We shall further assume that these beams are right circular polarized (the total angular momentum of the field is zero) i.e. E_{Rx}=-iE_{Ry} and E_{Sx}=iE_{Sy}. We can easily see that the form of the total field is helicoidal standing wave [68, 69, 70]. The intensity of helicoidal standing wave is uniform in space but polarization direction is spatially rotates around the z axis, like a helix, which caused by the spatially varying phase difference between the two orthogonal circular polarized beams. To record the polarization grating we used photoanisotropic material which is placed in the xy plane. The recorded polarization grating can be described by a spatially varying dielectric tensor given by Eq. 2.5. The intensity correlation components in Eq.2.5 of dielectric tensor are given by:

$$\begin{aligned}
|E_x|^2 &= \left(|E_{Rx}|^2 + |E_{Sx}|^2 + E_{Rx}E_{Sx}^* e^{-i(\vec{k}_R+\vec{k}_S)\vec{r}} + E_{Rx}^* E_{Sx} e^{i(\vec{k}_R+\vec{k}_S)\vec{r}}\right) \\
E_x E_y^* &= E_{Rx}E_{Ry}^* + E_{Sx}E_{Sy}^* + E_{Rx}E_{Sy}^* e^{-i(\vec{k}_R+\vec{k}_S)\vec{r}} + E_{Sx}E_{Ry}^* e^{i(\vec{k}_R+\vec{k}_S)\vec{r}} \\
E_x^* E_y &= E_{Ry}E_{Rx}^* + E_{Sy}E_{Sx}^* + E_{Ry}E_{Sx}^* e^{-i(\vec{k}_R+\vec{k}_S)\vec{r}} + E_{Sx}E_{Ry}^* e^{i(\vec{k}_R+\vec{k}_S)\vec{r}} \\
|E_y|^2 &= \left(|E_{Ry}|^2 + |E_{Sy}|^2 + E_{Ry}E_{Sy}^* e^{-i(\vec{k}_R+\vec{k}_S)\vec{r}} + E_{Ry}^* E_{Sy} e^{i(\vec{k}_R+\vec{k}_S)\vec{r}}\right)
\end{aligned} \tag{2.42}$$

We will readout the recorded grating by reference beam E_R and substituting Eq.2.5 into scalar wave equation:

$$\nabla^2\bar{E}+k_0^2\tilde{\varepsilon}\bar{E}=0 \tag{2.43}$$

we can find the following amplitude wave equations in order to describe the recording process when Bragg condition is satisfied (second order derivatives can be neglected applying the slowly varying amplitude approximation):

$$\begin{aligned}
&\frac{dE_{Sx}}{dz}-\left(-\frac{\alpha}{2}+i(\tilde{\gamma}_{\|}+\tilde{\gamma}_{\perp})2I_0\right)E_{Sx}=i(\tilde{\gamma}_{\|}-\tilde{\gamma}_{\perp})I_0(E_{Rx}-iE_{Ry})\\
&\frac{dE_{Sy}}{dz}-\left(-\frac{\alpha}{2}+i(\tilde{\gamma}_{\|}+\tilde{\gamma}_{\perp})2I_0\right)E_{Sy}=i(\tilde{\gamma}_{\|}-\tilde{\gamma}_{\perp})I_0(-E_{Ry}-iE_{Rx})\\
&\frac{dE_{Rx}}{dz}-\left(\frac{\alpha}{2}-i(\tilde{\gamma}_{\|}+\tilde{\gamma}_{\perp})2I_0\right)E_{Rx}=-i(\tilde{\gamma}_{\|}-\tilde{\gamma}_{\perp})I_0(E_{Sx}+iE_{Sy})\\
&\frac{dE_{Ry}}{dz}-\left(\frac{\alpha}{2}-i(\tilde{\gamma}_{\|}+\tilde{\gamma}_{\perp})2I_0\right)E_{Ry}=-i(\tilde{\gamma}_{\|}-\tilde{\gamma}_{\perp})I_0(iE_{Sx}-E_{Sy})
\end{aligned} \tag{2.44}$$

where $\tilde{\gamma}_j=\gamma_j'+i\gamma_j''=\frac{k_0}{2n}\chi_j$ (j=| | , ⊥) is the complex nonlinear coupling constant and $I_0=I_R=I_S$. The first term in the bracket (containing α) in the left side of Eq.2.44 is the linear background absorption constant. The second term in this bracket describes the influence of self $\tilde{\gamma}_{\|}$ and cross $\tilde{\gamma}_{\perp}$ bleaching on the beam intensity and phase, the term in the right hand is responsible for polarization coupling between the recording beams. Using the following boundary conditions $E_{Rx}(z=0)=E_{Rx}(0)$, $E_{Ry}(z=0)=E_{Ry}(0)$, $E_{Sx}(z=L)=0$, $E_{Sy}(z=L)=0$ and that the reconstruction beam is right circular polarized. These conditions result in the following analytical solutions of Eq.2.44:

$$\begin{aligned}
&E_{Sx}(z)=\beta_{ac}\frac{E_{Rx}(0)-iE_{Ry}(0)}{\beta_{dc}\sinh(\xi L)-i\xi\cosh(\xi L)}\sinh(\xi(z-L))\\
&E_{Sy}=-iE_{Sx}
\end{aligned} \tag{2.45}$$

where $\beta_{ac} = I_0(\tilde{\gamma}_{\|} - \tilde{\gamma}_{\perp})$ is responsible for *ac* complex refractive index modulation, $\beta_{dc} = \left[2I_0(\tilde{\gamma}_{\|} + \tilde{\gamma}_{\perp}) + i\frac{\alpha}{2} \right]$ is responsible for *dc* complex refractive index change the imaginary term of this term includes any absorption, scatter loss and $\xi = \sqrt{4\beta_{ac}^2 - \beta_{dc}^2}$. The solution of Eq.2.44 shows that the reflected beam is right circular polarized $E_{Sy} = -iE_{Sx}$ (see below the experiment) when we read the grating with right circular polarized beam (the same as recording beam). In this case the diffraction efficiency is given by:

$$\eta = \frac{|E_S(0)|^2}{|E_R(0)|^2} = \frac{2|\beta_{ac}|^2}{|\beta_{dc} - i\xi\coth(\xi L)|^2} \tag{2.46}$$

we see that photoanisotropy permits the coupling between the recording beams (in the case of either right-handed or left-handed two circular polarized counter-propagating beams). The coupling is impossible in the case $\tilde{\gamma}_{\|} = \tilde{\gamma}_{\perp}$. Note that ξ can be real or imaginary and the expression for diffraction efficiency contains both the refractive index grating and absorption grating.

If we read the grating with left polarized reference beam $E_{Rx}(0)=iE_{Ry}(0)$ (i.e., the opposite of the recording beam) then in this case we do not get a reflected beam. If we read the grating with a linearly polarized reference beam, when Bragg condition is satisfied, then we obtain from Eq.2.44 that the reflected beam is right circular polarized $E_{Sy} = -iE_{Sx}$. For this case the diffraction efficiency is two times smaller then for circularly polarized read out case (we assumed that strength of the grating is small $I_0(\tilde{\gamma}_{\|} - \tilde{\gamma}_{\perp})L << 1$).

2.4.2 Experimental results

The geometry of the experiment is shown in Fig. 2.11 [66]. We studied the interaction of two coherent counter-propagating beams (helicoidal standing wave) with cellulose acetate

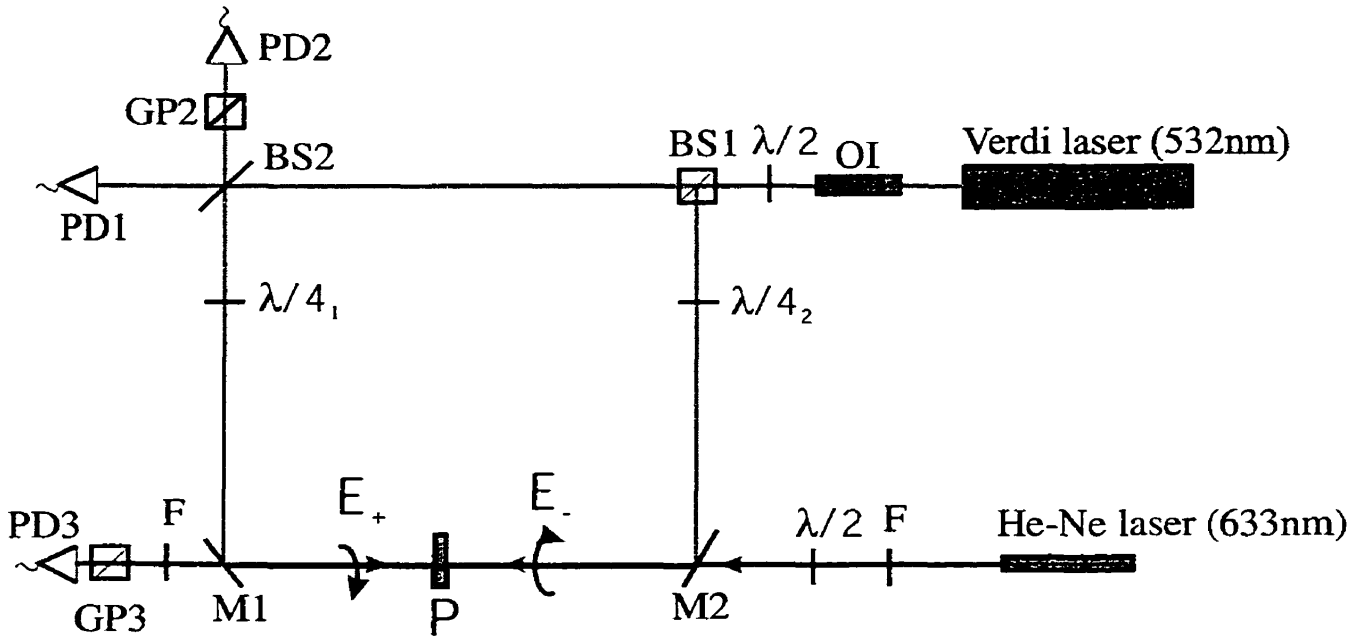

Figure 2.11 Schematic representation of the experimental set-up. OI, optical isolator; BS, beam splitter; λ/2, half wave plate; λ/4, quarter wave plate; PD, photodetector; M1, M2, dichroic mirrors; F, interferential filter (λ=632.8nm); E_+, E_-, circularly polarized beams of Verdi laser.

polymer film doped with Disperse Red 1 (DR1) azo-dye (material fabrication is presented in Ch.2). As a light source we used a coherent Verdi laser providing a linearly polarized single mode emission (at 532 nm). The output beam from the laser was divided into two beams by a beam splitter (BS1). Two circular polarized conterpropagating beams were obtained using quarter wave plates and two dichroic mirrors M1 and M2. A helicoidal (in the case of either right-handed or left-handed two circular polarized beams) electromagnetic field was used for excitation [18]. A slightly tilted incidence angle was used to separate the Fresnel reflection and the holographic grating diffraction. The recording light intensities were $I_{left}=I_{right}=54$ mW/cm^2. A He-Ne (P=2 mW) laser beam with waist smaller than the waist of the Verdi laser beams was also used to measure an optical activity at a different wavelength (λ=632.8 nm). These measurements were performed at normal incidence to helix. The wavelength of the He-Ne laser was out from the dye's absorption band and its influence on the grating was relatively small [51-53]. When we recorded the grating using helicoidal standing wave (HSW) we observe, when we read out the grating with the beam the same as recording, that the reflected light is circularly polarized (the same circularity as recording beam) i.e., with the same

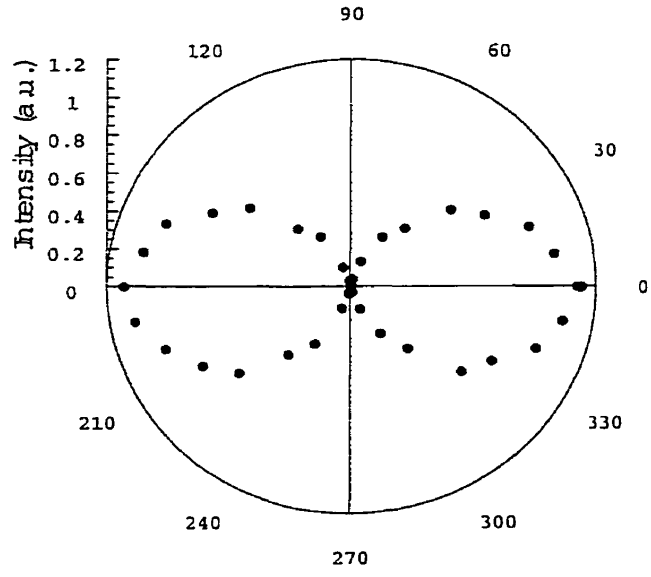

Figure 2.12 Demonstration that the polarization state of the reflected beam is linear after the quarter wave plate ($\lambda/41$) showing that the reflected beam is a circular polarized beam (the same as recording).

handedness as the helical structure of the polymer material, and the reflection peak is centered at wavelength λ_0=nP=2nΛ (Bragg condition), where n is the average refractive index, $P = 2\pi/q_0 = 2\Lambda$ is the pitch of the polymer material and Λ is the periodicity interval along z axis. The experiment was performed as follows: first we recorded the grating during 12-15 minutes then we switch off the beam E. for analyze the reflected beam when we read the grating by a beam E_+. We verify (rotating the Glan prism GP2) that the polarization state of the reflected beam is linear after the quarter wave plate ($\lambda/4_1$) while reading the grating by a circular polarized beam (see Fig.2.12). We verified that the polarization state of the reflected beam is the same as the recording beam polarization i.e. right circular polarized which is in agreement with the predictions of the theory. We measured the relaxation time of the grating by switch off one of the recording beams and reading it by another beam. The relaxation time t~2 min. of the grating while reading by a circularly polarized beam is shown in Fig.2.13. Then we measured the coefficient of reflection of the system (HSW) (5 minutes after switching off one of the recording beams).

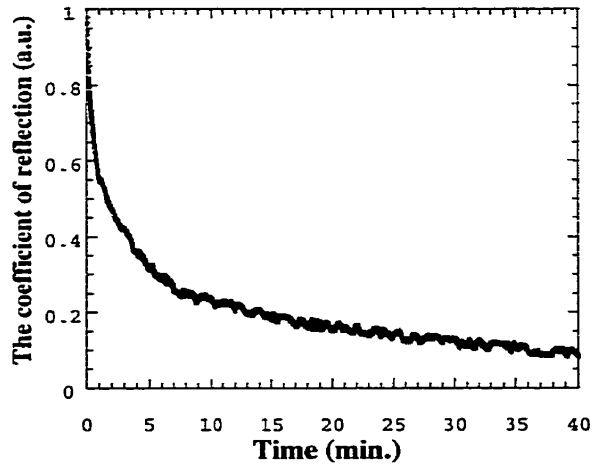

Figure 2.13 The relaxation time of the grating.

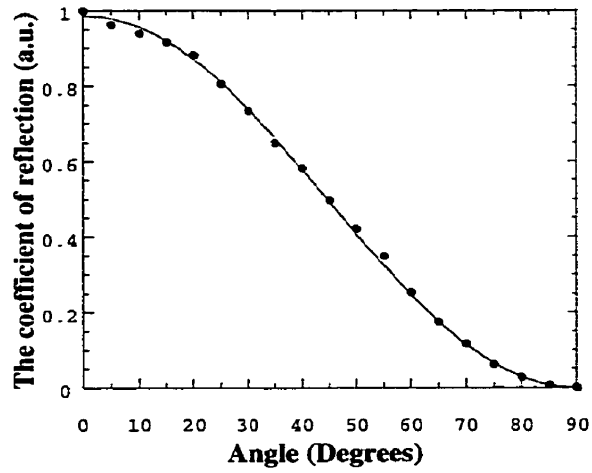

Figure 2.14 Dependence of the coefficient of reflection of the grating on the polarization state of the reading beam.

Fig.2.14 demonstrates that the grating reflectance strongly depends on the polarization state of the reading beam, which was obtained by rotating the quarter wave plate ($\lambda/4_1$). Maximum reflectance R_{max}=1.3% corresponds to the reading beam with the same polarization as the recording circular polarized beam. The coefficient of reflection $R=R_{max}/2$ for the linearly polarized reading beam. For the orthogonal circular polarization of the reading beam the reflectance is zero.

The optical properties of the structure that we created are similar to cholesteric liquid crystals or twisted nematic liquid crystals i.e. an optical axis gradually rotates around the z axis. In the case

$$\lambda >> P(n_{\parallel} - n_{\perp}) \tag{2.47}$$

where P is the pitch of the spiral, the film acts as an optical active medium i.e., it will rotate the polarization of linearly polarized light by an angle ψ which does not depend on the input polarization direction. To measure the optical activity effects we used a linearly polarized He-Ne laser beam. The measurements were performed using a Glan prism GP3 (Fig.2.11) which cut the linearly polarized He-Ne laser beam before the recording of the grating. Small ellipticity e=0.052 of the He-Ne laser beam, which transmitted the film, was observed due to the linear birefringence of the polymer film $n_{\parallel} - n_{\perp} \approx 2 \cdot 10^{-3}$ (conditions of Eq.2.9 are satisfied $Q' = 126$ and $\rho \approx 6 \cdot 10^3$). But we did not observe any optical rotation because it was very small. Under the condition (2.47) two circularly polarized beams of opposite senses and different wave vectors propagate along z axis. The optical rotation is given by the de Vries formula [71]:

$$\frac{\psi}{L} = \frac{k_0}{16}\left(\frac{n_{\parallel}^2 - n_{\perp}^2}{n_{\parallel}^2 + n_{\perp}^2}\right)^2 \frac{1}{\lambda'(1-\lambda'^2)} \tag{2.48}$$

where $\lambda' = \frac{\lambda}{nP}$, λ being the wavelength of incident light. Namely, $\lambda' = 1.19$, then $\psi \approx 4 \cdot 10^{-4}$ degrees.

2.5 Conclusion

In this chapter thin and thick dynamic photoanisotropic gratings are presented. The kinetics of holographic excitation of these samples is studied in intensity and polarization recording conditions. Simple theoretical coupled wave equations for thick samples are obtained.

A simple theoretical model that describes the recording and reconstruction of the polarization state of light in photoanisotropic materials is developed. The conditions to reconstruct the polarization state of an object beam using a plane polarized reference beam are obtained. We have shown that a cellulose acetate matrix provides bipolar response to the photoexcitation (due to the high angular mobility of chromophores, etc.). We used this matrix to record and reconstruct the polarization state of an elliptically polarized object beam. The particularity of our realization is the response of the medium, which permits the use of a single plane polarized reference beam for both recording and reconstruction. The experimental results are in agreement with the theory. We believe that this work would be useful for various polarization manipulation systems.

Another interesting results obtained is the light-induced helicoidal structure. Using photoanisotropic materials we have demonstrated a macroscopic light-induced helicoidal structure in a non-chiral polymer films i.e. an optical axis that gradually rotates around the normal of the film, like a helix. Polarization properties of the recorded reflection polarization gratings are similar to cholecteric liquid crystals where the response of the system is different to left and right circularly polarized light. Two counter-propagating circular polarized beams were used for excitation. Theoretical analysis using coupled wave equations for reflection photoanisotropic gratings was made for the first time.

CHAPTER 3

ASYMMETRIC DIFFRACTION BY SPATIAL MODULATION OF ABSORPTION AND REFRACTION

The discovery of the photorefractive mechanism of nonlinearity has provided a rather surprising example of asymmetric light diffraction [12]. The exposition of a photorefractive medium by a light interference pattern leads to the spatially periodic photoexcitation of carriers, spatial separation of positive and negative charges, and refractive index modulation via linear [13-17] or quadratic [72-73] electro-optic effects. The resultant modulation of the real part of the dielectric constant may be spatially shifted with respect to the light interference pattern [13, 15] and to the corresponding modulation of the imaginary part of the dielectric constant, see for example Ref. [25]. Diffraction of light in such structures may be strongly asymmetric (exchange of energy) [13, 16, 17, 25].

In this chapter we describe linear diffraction gratings that provide strongly asymmetric diffraction without surface modulation. Asymmetric diffraction may be achieved using blazed gratings. But in our case the spatial phase shift of the refractive index grating relative to the absorption grating is the origin of asymmetric behavior. Experimental results made with thin mixed phase and absorption gratings in azo-dye-doped polymer films are in good quantitative agreement with our theoretical results.

3.1 Asymmetric diffraction

3.1.1 Coupled wave analysis for mixed phase and absorption gratings in photoanisotropic materials

In this section we will consider the case of thick holograms only i.e. the holograms which satisfy the conditions of Eq.2.9. For thick gratings, as we already mentioned in chapter 2, it is sufficient to consider the propagation of only two plane waves R and S. The total electric field amplitude is given by:

$$\vec{E}(\vec{r},t) = \vec{E}_{Ry}(\vec{r})\exp(i\vec{k}_R\vec{r} - i\omega t) + \vec{E}_{Sy}(\vec{r})\exp(i\vec{k}_S\vec{r} - i\omega t) \tag{3.1}$$

where $\vec{k}_s = k_0 n(-\sin\theta, 0, \cos\theta)$, $\vec{k}_R = k_0 n(\sin\theta, 0, \cos\theta)$, $k_0 \equiv \frac{2\pi}{\lambda_0}$, λ_0 is the wavelength in vacuum and n is the uniform refractive index of the medium. We consider the medium containing phase and amplitude plane holographic gratings, which are shifted relative to each other by phase Δ. The thick grating is assumed to be recorded in photoanisotropic medium by two s-polarized beams of equal intensities I_R=I_S=I_0. The complex dielectric tensor can then be expressed as (using Eq.2.5):

$$\tilde{\varepsilon}(\vec{r}) = \varepsilon_0' + 2\chi_{\|}' I_0(1+\cos(\vec{q}\cdot\vec{r})) + i(\varepsilon_0'' + 2\chi_{\|}'' I_0(1+\cos(\vec{q}\cdot\vec{r}+\Delta))) \tag{3.2}$$

where $\vec{q} = \vec{k}_R - \vec{k}_S$ and the superscript 0 denotes the constant component. It is interesting to compare the complex dielectric tensor in photoanisotropic medium with the complex dielectric tensor in isotropic medium:

$$\tilde{\varepsilon}(\vec{r}) = \varepsilon_0' + 2\Delta\varepsilon'\cdot\cos(\vec{q}\cdot\vec{r}) + i(\varepsilon_0'' + 2\Delta\varepsilon''\cdot\cos(\vec{q}\cdot\vec{r}+\Delta)) \tag{3.3}$$

Two key differences are apparent. First, the complex photoanisotropic grating in (3.2) is directly proportional to the local intensity. Second, the bulk photoanisotropic material is

affected by the *dc* component of the interference pattern, while the complex dielectric tensor (3.3) is not. Using the time-independent vector wave equation 2.11 for two s-polarized beams we obtain two coupled wave equations (second order derivatives can be neglected applying the slowly varying amplitude approximation):

$$\begin{aligned}
&\frac{dE_R}{dz}+\left[\frac{k_0\varepsilon_0''}{2n}-i\frac{k_0(\chi_{\|}'+i\chi_{\|}'')I_0}{n}\right]E_R=i\frac{k_0I_0}{2n}(\chi_{\|}'+i\chi_{\|}''e^{i\Delta})E_S\\
&\frac{dE_S}{dz}+\left[\frac{k_0\varepsilon_0''}{2n}-i\frac{k_0(\chi_{\|}'+i\chi_{\|}'')I_0}{n}\right]E_S=i\frac{k_0I_0}{2n}(\chi_{\|}'+i\chi_{\|}''e^{-i\Delta})E_R
\end{aligned} \tag{3.4}$$

these equations were derived when exact Bragg condition is satisfied. To find the spatial evolution of the signal wave S we extract E_R from second equation of (3.4) and insert it into first equation of 3.4 to get the second-order differential equation:

$$\begin{aligned}
&\frac{d^2E_S}{dz^2}+2\left[\frac{k_0\varepsilon_0''}{2n}-i\frac{k_0(\chi_{\|}'+i\chi_{\|}'')I_0}{n}\right]\frac{dE_S}{dz}+\left[\frac{k_0\varepsilon_0''}{2n}-i\frac{k_0(\chi_{\|}'+i\chi_{\|}'')I_0}{n}\right]^2E_S+\\
&\left(\frac{k_0I_0}{2n}\right)^2\left(\chi_{\|}'^2-\chi_{\|}''^2+2\cdot i\chi_{\|}'\cdot\chi_{\|}''\cos\Delta\right)E_S=0
\end{aligned} \tag{3.5}$$

we will denote $M=\left(\chi_{\|}'^2-\chi_{\|}''^2+2\cdot i\chi_{\|}'\cdot\chi_{\|}''\cos\Delta\right)$. The boundary conditions for diffraction from a transmission grating are:

$$E_S(0)=0 \quad \text{and} \quad E_R(0)=E_{R0} \tag{3.6}$$

The general solution of the differential equation 3.5 has the form:

$$E_S=C_1\exp(\xi_1 z)+C_2\exp(\xi_2 z) \tag{3.7}$$

where C_1 and C_2 are complex constants. Then using boundary conditions 3.6 we obtain

$$E_S(z) = i\frac{E_{R0}}{\sqrt{M}}(\chi'_{\|} + i\chi''_{\|}e^{-i\Delta})\exp\left(-\frac{k_0\varepsilon''_0 z}{2n} + i\frac{k_0(\chi'_{\|} + i\chi''_{\|})I_0 z}{n}\right)\left(\frac{e^{i\frac{k_0 I_0}{2n}z\sqrt{M}} - e^{-i\frac{k_0 I_0}{2n}z\sqrt{M}}}{2i}\right) \quad (3.8)$$

the expression for diffraction efficiency is given by

$$\eta = \frac{|E_S(L)|^2}{|E_R(0)|^2} = e^{-\left(\frac{k_0\varepsilon''_0 L + 2k_0\chi''_{\|}I_0 L}{n}\right)} \cdot \frac{(\chi'^2_{\|} + \chi''^2_{\|} + 2\cdot\chi'_{\|}\cdot\chi''_{\|}\sin\Delta)}{|M|} \cdot \left\{\sin^2\left(\frac{k_0 I_0}{2n}L\,\mathrm{Re}\left[\sqrt{M}\right]\right) + \sinh^2\left(\frac{k_0 I_0}{2n}L\,\mathrm{Im}\left[\sqrt{M}\right]\right)\right\} \quad (3.9)$$

That describes the diffraction at a mixed thick phase and absorption transmission grating in photoanisotropic material. In the case of small grating strength $\frac{k_0 I_0}{2n}\chi'_{\|}L << 1$ $\left(\frac{k_0 I_0}{2n}\chi''_{\|}L << 1\right)$ we obtain:

$$\eta = \frac{|E_S(L)|^2}{|E_R(0)|^2} = e^{-\frac{k_0\varepsilon''_0 L}{n}} \cdot \left[\frac{k_0 I_0}{2n}L\right]^2 \left(\chi'^2_{\|} + \chi''^2_{\|} + 2\cdot\chi'_{\|}\cdot\chi''_{\|}\sin\Delta\right) = e^{-\frac{k_0\varepsilon''_0 L}{n}} \cdot \left[\frac{k_0 L}{2n}\right]^2 \left(\Delta\varepsilon'^2_{\|} + \Delta\varepsilon''^2_{\|} + 2\cdot\Delta\varepsilon'_{\|}\cdot\Delta\varepsilon''_{\|}\sin\Delta\right) \quad (3.10)$$

where $\Delta\varepsilon'_{\|} = \chi'_{\|}I_0$ and $\Delta\varepsilon'' = \chi''_{\|}I_0$. Kogelnik's expression [24] may be obtained for the special case when $\Delta=2\pi m$, m is an integer. We can easily see the lack of symmetry between the positive dephasing, $\Delta[0,\pi]$ and the negative dephasing, $\Delta[0,-\pi]$ i.e. the diffraction efficiency increases or decreases depending on whether the phase difference between the two gratings is positive or negative. This behavior is easily explained by the interference of the waves scattered off the phase and absorption grating, respectively. The maximum asymmetry of diffraction corresponds to $\Delta=\pi/2$.

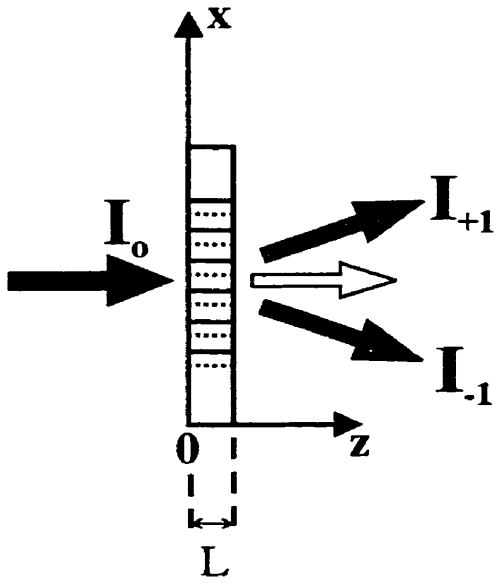

Figure 3.1 Schematic illustration of the diffraction of light.

3.1.2 Raman-Nath approximation

We will consider the case when the conditions of Eq.2.8 are satisfied. We will take the complex dielectric constant of the photoanisotropic medium (which is infinite in the x and y directions, see Fig.3.1) as:

$$\tilde{\varepsilon} = \varepsilon_0' + 2\Delta\varepsilon_{\|}'(1+\cos(qx)) + i(\varepsilon_0'' + 2\Delta\varepsilon_{\|}''(1+\cos(qx+\Delta))) \tag{3.11}$$

where $2\Delta\varepsilon_{\|}' = 2\chi_{\|}' I_0$ and $2\Delta\varepsilon'' = 2\chi_{\|}'' I_0$ are the amplitudes of modulation of the real and imaginary parts of the complex dielectric constant of the medium, respectively, Δ is the spatial phase shift between these modulations and q is the grating wave vector. We will adopt the wave equation 2.11 describing the propagation of complex amplitude $E(\vec{r})e^{-i\omega t}$ in the form of scalar wave equation (Helmholtz equation):

$$\nabla^2\vec{E} + k_0^2\tilde{\varepsilon}\vec{E} = 0 \tag{3.12}$$

We consider a normally incident (at z=0) s-polarized plane wave (see Fig.3.1). The fields and the gratings are unchanging in the y direction. We will expand the field inside the modulated medium in terms of space harmonic components (m) of the field in periodic structure. Notice that the individual space harmonics do not satisfy the wave equation 3.12, but the sum of all space harmonics does satisfy the wave equation. These space harmonics inside the grating correspond to the diffracted orders outside of the grating. Then we will search for Helmholtz equation solutions in the following form [14, 28, 29]

$$E = \sum_{m=-\infty}^{\infty} S_m(z)\exp(ikz - imqx) \tag{3.13}$$

The theory of Raman-Nath may be obtained directly from rigorous coupled wave equations if second derivatives of the field amplitudes (assuming slow variations for the amplitudes S_m) and dephasing from the Bragg condition are neglected. Then we obtain the following set of coupled-wave equations [64, 65]:

$$\begin{aligned} &2ik_0 n\frac{dS_m}{dz} + \left[i k_0^2 \Delta\varepsilon_0'' - (mq)^2 + 2k_0^2\left(\Delta\varepsilon_{\|}' + i\Delta\varepsilon_{\|}''\right)\right]S_m + \\ &k_0^2\left[\left(\Delta\varepsilon_{\|}' + i\Delta\varepsilon_{\|}'' e^{i\Delta}\right)S_{m+1} + \left(\Delta\varepsilon_{\|}' + i\Delta\varepsilon_{\|}'' e^{-i\Delta}\right)S_{m-1}\right] = 0 \end{aligned} \tag{3.14}$$

This set of equations is completed by the following boundary conditions:

$$\begin{aligned} &S_0(z=0) = S_0, \\ &S_m(z=0) = 0, \text{ for } |m| \geq 1, \end{aligned} \tag{3.15}$$

We solved the problem of Eqs.3.14 and 3.15, assuming, that the conditions of Eq.2.8 are satisfied. These assumptions allow us to take into account only first orders of diffraction because the amplitudes of higher orders decrease rapidly with the diffraction order m (as $\gamma^{|m|}$) [74]); i.e. we take $S_m \equiv 0$ for all $|m| > 1$. Solutions of Eqs (3.14) with boundary conditions (3.15) give the diffraction efficiencies of +1st- and –1st-order diffracted beams at the output of the medium z = L [64, 65]:

$$\eta_{\pm 1} = e^{-\frac{k_0 \varepsilon_0'' L}{n}} \cdot \left[\frac{k_0 L}{2n}\right]^2 \left(\Delta\varepsilon_{\|}'^2 + \Delta\varepsilon_{\|}''^2 \mp 2 \cdot \Delta\varepsilon_{\|}' \cdot \Delta\varepsilon_{\|}'' \sin\Delta\right) \qquad (3.16)$$

Two important consequences follow from equation 3.16: the asymmetric diffraction and oscillatory dependence of diffraction upon the grating parameters Δ, $\Delta\varepsilon_{\|}'$ and $\Delta\varepsilon_{\|}''$. The optimal condition of the asymmetry, as it can be easily seen, corresponds to the case $|\Delta| = \pi/2$ and $\Delta\varepsilon_{\|}' = \Delta\varepsilon_{\|}''$. Note that the same results we could obtain simply using amplitude transmittance theory. Because the diffraction inside the medium is inessential then the hologram behaves like a transparency (thin mask). Then $E_{out}(\bar{r}) = t(\bar{r})E_{in}(\bar{r})$ where $t(\bar{r})$ is determined by the local value of the complex dielectric constant.

Various possibilities of the application of similar shifted gratings in linear photonic systems have been discussed [25, 75]. However, to our knowledge, there have been no reports of corresponding experimental realizations because of the difficulty of obtaining the desired phase shift between the modulations of the real and imaginary parts of $\tilde{\varepsilon}$. Let us emphasize, that this is not the case of non-linear materials with photorefractive nonlinearity where the grating shift is often naturally obtained as a result of the particular microscopic mechanism of photoexcitation [3, 16].

We show below, for the first time to our knowledge, that one can artificially create such shifted gratings and obtain asymmetric diffractive elements in almost any kind of host matrix (glasses, sol-gels, polymers) in which the introduction of active guest species (dyes, ions) is possible by doping, implantation, evaporation, etc.

3.2 Experimental results

The experimental solution that we proposed is based on spatial management of dispersion and may be qualitatively explained by Kramers-Kroning relations. We achieve our

goal in the following manner. First, we uniformly dope the desired matrix (see below) with two dyes, and then used double-exposure technique for recording the shifted gratings. The initially uniform mixture of two spectrally different dyes (which have absorption or gain lines centered at wavelengths λ_1 and λ_2) provides spatially uniform dielectric constants $\tilde{\varepsilon}(\lambda_1)$ and $\tilde{\varepsilon}(\lambda_2)$. The exposure of this medium to the periodic pattern of an excitation light, at the wavelength λ_1, creates a spatial hole burning pattern (dye isomerization, bleaching, etc., see chapters1 and 2) [47-49, 51, 52], with corresponding gratings of ε' and ε''. The consecutive exposure of the same medium to the excitation light of the same periodicity, but at wavelength λ_2 and with a spatial shift at desired distance δx, creates a second spatial hole burning pattern, with corresponding gratings of ε' and ε''. Thus, an incident (reading) light with wavelength λ_1 will see mainly a modulation of ε'' at spatial points, that correspond to the maximum of the first exposed (at wavelength λ_1) grating. In contrast, the same wave will see mainly modulations of ε' at spatial points, that correspond to the maxima of the second grating, in agreement with Kramers-Kroning relations.

We recorded phase ($\Delta\varepsilon'$) and amplitude ($\Delta\varepsilon''$) gratings upon cellulose acetate films doped with two dyes, 5% (by weight) Disperse Red 1 (DR1) and 7% (by weight) Methylene Blue (MB), with absorption lines centered at $\lambda = 500$ nm and $\lambda = 666$ nm, respectively (see Fig.3.2). Polymer films were prepared by dip coating (see chapter 2). The thickness of film obtained was measured to be 2μm.

The experimental setup for recording of diffractive gratings is shown in Fig. 3.3. Light beams with 514.5- and 632.8 nm wavelengths were generated by means of single mode cw Ar-ion and He-Ne lasers, respectively. These wavelengths and dyes were chosen to produce a significant absorption of DR1 at 514.5 nm and much less absorption at 632.8 nm. In contrast, MB absorbs significantly at 632.8 nm, and its absorption is much less at 514.5 nm (see Fig.3.2). The Ar-ion laser and He-Ne laser beams were aligned collinearly using a beam splitter (BS) and a diaphragm (Dph). Intensities and polarizations of beams were controlled by combining Glan prisms (GP) with $\lambda/2$ plates. The exposure of the polymer film (P) was

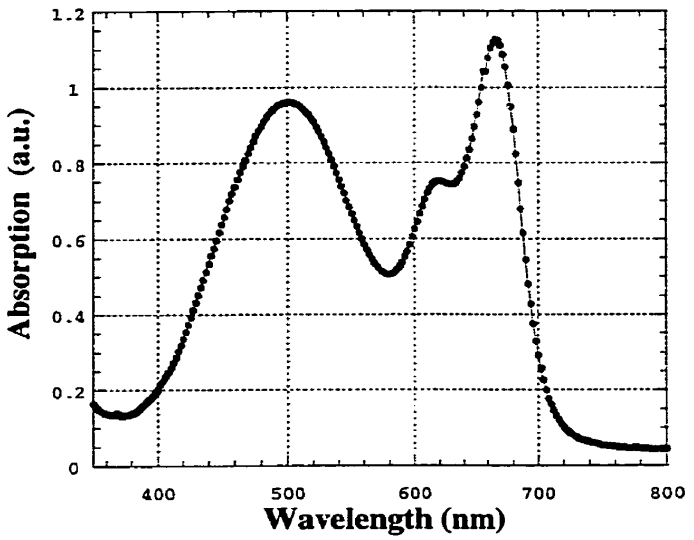

Figure 3.2 Absorption spectra of DR1/MB doped cellulose acetate film.

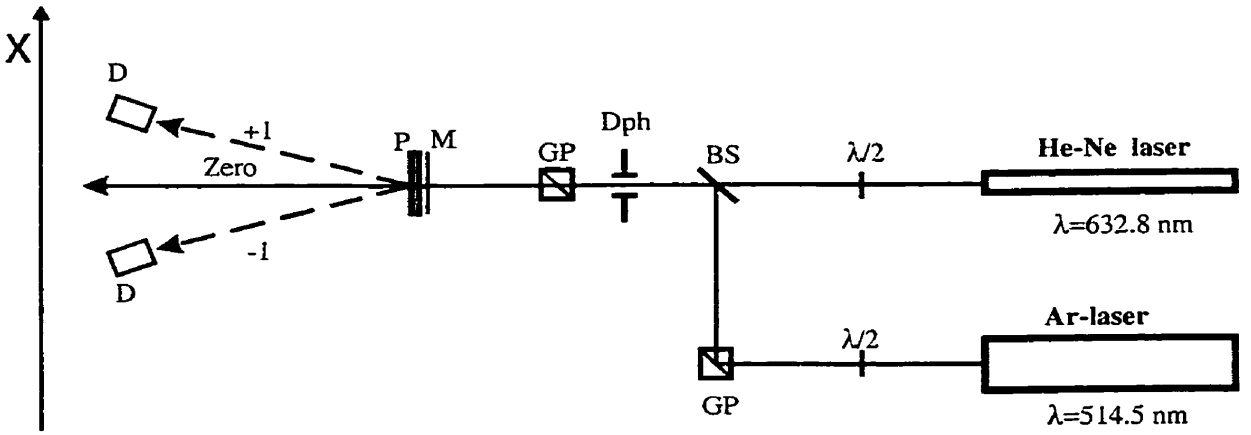

Figure 3.3 The experimental set-up for grating recording. GP's, Glan prisms; λ/2, half-wave plates; BS, beam splitter; Dph, diaphragm; M, mask; P, polymer film; D, detectors.

made at normal incidence via a binary amplitude mask (M) with a period Λ = 40 μm. The mask was placed on the surface of the polymer film (in the vertical plane). The polymer film was illuminated by s-polarized laser beams. The readout of obtained gratings was always performed by strongly attenuated (20 times by intensity) laser beams.

The diffraction efficiencies of gratings were experimentally measured as $\eta = \frac{I_{diffracted}}{I_{incident}} 100\%$, where the $I_{diffracted}$ is the intensity of the +1st-order or −1st-order of diffraction without losses in the diffracted beam caused by absorption and Fresnel reflection. Losses owing to surface reflectivity R_{Fr} (at $\varepsilon_{0film} \approx 2.56$) were of the order of 5.3%. The linear transmission of the sample was $(1\text{-}R_{Fr})^2 \exp(-k_0 \varepsilon_0'' L/n) \approx 0.12$, and it corresponds to the absorption coefficient $\varepsilon_0'' = 0.162$.

Before the creation of the shifted gratings we measured the relative contributions of phase and amplitude gratings separately. That is, we exposed (through the mask) the fresh polymer film by He-Ne laser beam (with intensity 0.57 W/cm^2) for 30 minutes. Then we removed the mask and we read out the amplitude grating with a weak He-Ne laser beam. Measured diffraction efficiency was η_{He-Ne} = 0.01% (on an amplitude grating of bleached MB). Thus we obtained $2\Delta\varepsilon_{\|}'' = 0.0088$ using the Eq.3.16 (for $\Delta\varepsilon_{\|}' = 0$ and $\Delta = 0$). Afterwards we exposed the fresh polymer film (through the same mask) to an Ar-ion laser beam (with intensity 0.39 W/cm^2) for 30 min. We removed the mask and we read out the phase grating with a He-Ne laser beam. Measured diffraction efficiency was η_{He-Ne} = 0.036% (phase grating) from which (using Eq.3.16 with $\Delta\varepsilon_{\|}'' = 0$ and $\Delta = 0$), we obtained $2\Delta\varepsilon_{\|}' = 0.0167$. We found from these data the values of parameters $Q' = 0.003$ and γ=0.05, that confirm the validity of our theoretical approximation.

The next step in our experiment was recording of shifted gratings and their readout. The polymer film was illuminated by s-polarized He-Ne laser beam with 0.57 W/cm^2 intensity for 30 min. Then we shifted the mask in a given direction (collinear with the grating wave

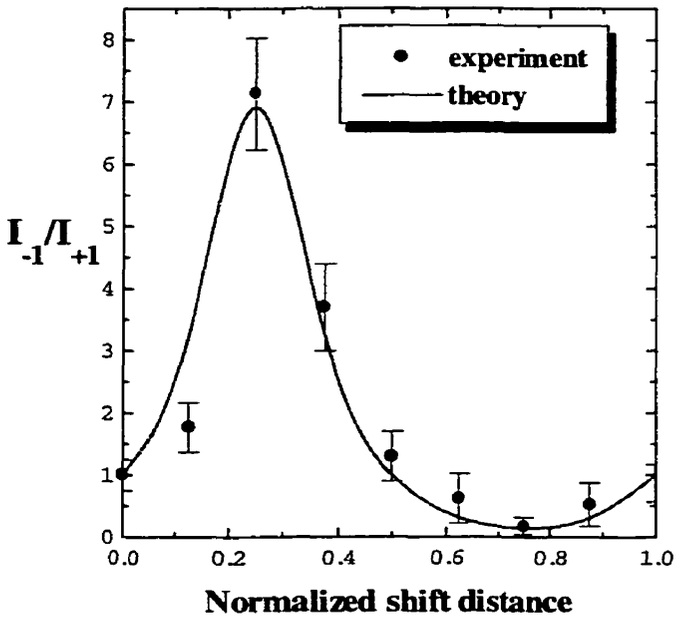

Figure 3.4 Ratio of the intensity of the −1st-order diffracted beam to the intensity of the +1st-order diffracted beam as a function of the normalized (to the period of the mask) shift distance. The theoretical fit was obtained with Eq.3.15.

vector) for a distance δx (in steps $\delta x = \Lambda/8$) and illuminated the grating with an s-polarized Ar-ion laser beam with 0.39 W/cm^2 intensity for 30 min. Readout of the gratings (with mask removed) was performed by the He-Ne laser beam with strongly attenuated intensity. Fig.3.4 illustrates the ratio of the intensity of the −1st-order diffracted beam to the intensity of the +1st-order diffracted beam as a function of the normalized (to the period of the mask) shift distance $\delta x/\Lambda$ when the grating read out by a He-Ne laser beam. Circles correspond to the experimental results and the solid curve corresponds to the theoretical fit using the Eq. 3.16. As one can see, the most significant asymmetry (with maximum ratio $I_{+1}/I_{-1} = 7.1$) of diffraction takes place for $\Lambda/4 = 10\ \mu$m. This corresponds to the case when the amplitude grating is $\pi/2$ out of phase with respect to the phase grating. The minimum $I_{+1}/I_{-1} = 0.18$ corresponds to $3\Lambda/4 = 30\ \mu$m, i.e. when the shift between the phase and amplitude gratings is $3\pi/2$, in agreement with our theoretical predictions (see also [13, 25, 64, 65, 75]). The theoretically obtained (from the fit) value of $\Delta\varepsilon_{\|}' / \Delta\varepsilon_{\|}''$ is 2.23, whereas the experimentally measured (from the experiment described above) value is $\Delta\varepsilon_{\|}' / \Delta\varepsilon_{\|}'' \approx 1.9$.

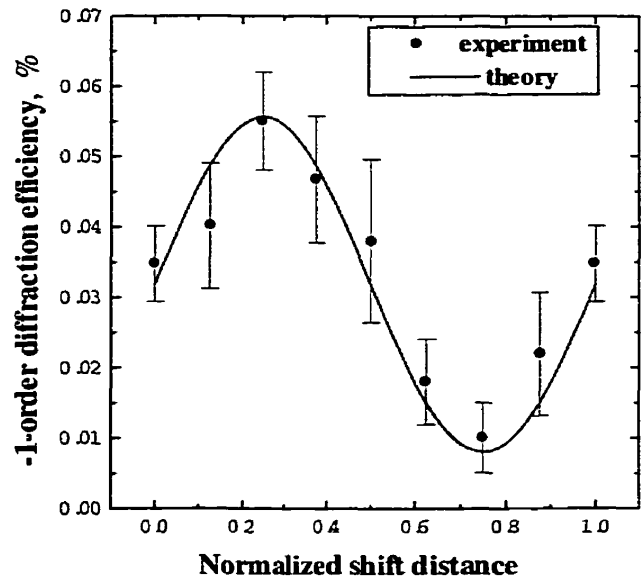

Figure 3.5 Oscillatory character of the –1st-order diffraction versus the grating shift. The theoretical fit was obtained with Eq.3.15.

Diffraction efficiencies in +1st and –1st diffracted orders demonstrate an oscillatory character as predicted by Eq.3.16. Such behavior for the –1st-order diffraction is presented in Fig.3.5 for the same experiment as described above. Circles correspond to the experimental results and the solid curve is the theoretical fit made by using the same (as in the previous experiment) value $\Delta\varepsilon_{\|}' / \Delta\varepsilon_{\|}'' \approx 2.23$. Therefore we obtained from the theoretical fit the values $2\Delta\varepsilon_{\|}' = 0.0143$ and $2\Delta\varepsilon_{\|}'' = 0.0064$, whereas the experimentally measured values were $\Delta\varepsilon_{\|}' = 0.0167$ and $\Delta\varepsilon_{\|}'' = 0.0088$. We believe that the reason for the difference between experimental and theoretical data is the residual absorption of light by both dyes, because their absorption bands are relatively large and partially overlap (see Fig.3.2). Another problem is the presence of undesirable gratings due to the presence of a strip mask and the diffraction of light on it during recording, whereas the theory was developed for sinusoidal gratings. We could use also a holographic recording technique that would give us (along with the use of new dyes) much stronger asymmetric diffraction.

The surfaces of our polymer films were scanned (by a Dektak profile meter) for each experiment, and no relief modulations were observed. This result confirms that our gratings were indeed recorded in the volume of the film and the asymmetric diffraction resulted only

from the controlled spatial shift between the phase and amplitude gratings and not from the blazed surface modulation.

3.3 Conclusion

In this chapter we described linear diffraction gratings that provide asymmetric diffraction without surface modulation. Asymmetric diffraction may be achieved using blazed gratings. But in our case the spatial phase shift of the refractive index grating relative to the absorption grating is the origin of asymmetric behavior. The spatial phase shift between the absorption and the phase grating present in photoanisotropic materials has been discussed for thick and thin gratings. Experimental results made with thin mixed phase and absorption gratings in azo-dye-doped polymer films are in good quantitative agreement with our theoretical results. It has been demonstrated that diffraction efficiency show strong dependence on dephasing. The most significant asymmetry (with maximum ratio $L_{+1}/L_{-1} = 7.1$) of diffraction takes place when the amplitude grating is $\pi/2$ out of phase with respect to the phase grating. Similar results may be expected to be obtained for slanted gratings and for reflection gratings (that could find interesting applications).

We believe that the proposed approach and the results obtained may find interesting applications. This device is not expensive and is easy to control. The application of lasing dyes or ions (for example, erbium) would permit their use in optical data communication systems for which asymmetric reflection and amplification are needed.

PART II

STUDY OF STIMULATED DIFFUSION BACKSCATTERING IN PHOTOREFRACTIVE CRYSTALS

In these part of thesis we analyzed the stimulated diffusion backscattering (SDS) in photorefractive crystals based on the advantages of the reflection photorefractive gratings. The material parameters were measured. We believe that optimal crystal (its processing procedure and doping density) is still unknown even for visible range.

In the following chapters we discussed:

1. General analysis of the stimulated diffusion backscattering.
2. Characterization of crystal parameters: gain, reflectivity, response rate, dark conductivity and grating decay.
3. Clarification of the possibility of obtaining self-phase conjugation at backward SDS in the steady-state conditions.
4. Comparison of sensitivities of different geometries with respect to pump energy.

CHAPTER 4

STIMULATED DIFFUSION BACKSCATTERING IN PHOTOREFRACTIVE CRYSTALS

4.1 The photorefractive effect

4.1.1 Introduction

Photorefractive effect leads to a variety of nonlinear optical phenomena in certain types of crystals. The basic mechanism of the effect is the excitation and redistribution of charge carriers inside a crystal upon nonuniform illumination. The redistributed charges give rise to a nonuniform internal electric field and thus spatial variations in the refractive index of the crystal through the electro-optic effect (Pockels). A qualitative model of the photorefractive effect was discovered by Ashkin [12]. When we illuminate the crystal with periodic pattern the excited photoelectrons leave the illuminated region through diffusion or drift due to an externally applied electric field (or by the photovoltaic effect). They are trapped in nonilluminated regions to give rise to a nonuniform space charge, which lead to an electric field distribution within the crystal.

Important photorefractive materials include barium titanate ($BaTiO_3$), bismuth silicon oxide ($Bi_{12}SiO_{20}$), lithium niobate ($LiNbO_3$), potassium niobate ($KNbO_3$), gallium arsenide (GaAs), and strontium barium niobate (SBN) and photorefractive polymers. The materials

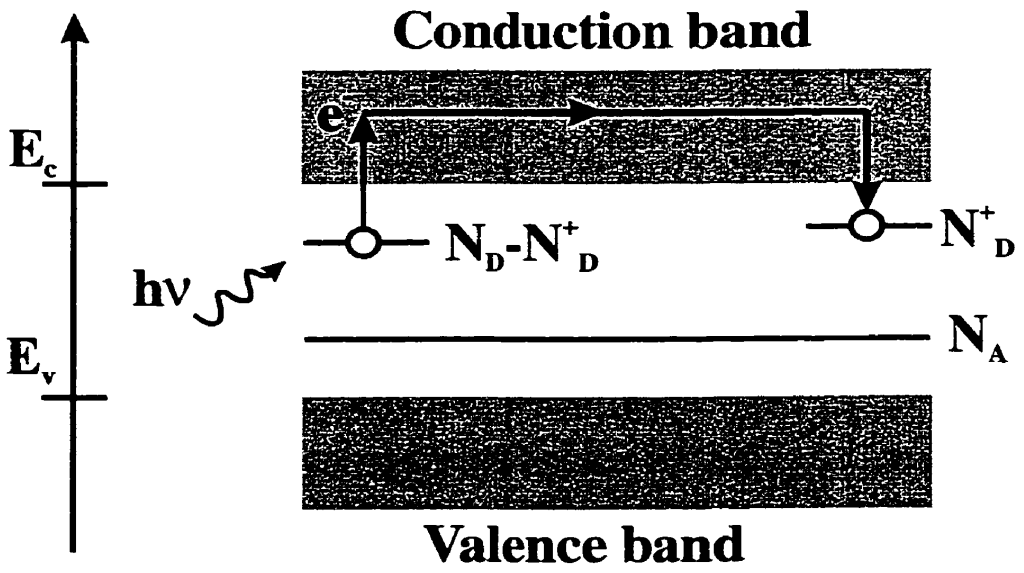

Figure 4.1 Schematic of charge transport model of photorefractivity. $N_D - N_D^+$ is the number of neutral (filled) donors (Fe^{2+}, for example); N_D^+ is the number density of ionized donors (Fe^{3+}, for example); N_A is the number density of negative charges that compensate for the charge N_D^+ under dark conditions ($N_D^+(I=0) = N_A$).

have a large non-linear response even at low intensities in the mW range. They are typically sensitive at a broad range of wavelengths, and their properties depend on the concentration of impurities ions. They typically have a moderate to slow time response ranging from microseconds to seconds.

4.1.2 Basic equation for hologram recording amplitude

First complete model (the band transport model) of the photorefractive effect was given by Kukhtarev in 1979 [13]. The band transport model assumes that electrons (or holes) are optically excited from filled donor (or acceptor) sites to the conduction (or valence) band, where they migrate to dark regions in the crystal by drift or diffusion before recombining into an empty trap (Fig.4.1). In the following analysis the complex amplitudes for all space-varying periodic values will be used [16]. The sinusoidal distribution of light intensity in the recorded interference pattern is:

$$I(x) = I_o(1 + |m|\cos(qx + \varphi_0)) = I_0\left[1 + \frac{m}{2}\exp(iqx) + \frac{m^*}{2}\exp(-iqx)\right] \quad (4.1)$$

where $m = |m|\exp(i\varphi_0)$. The electric field E(x) is given by:

$$E(x) = E_0 + \frac{1}{2}\left[E_{sc}\exp(iqx) + E_{sc}^*\exp(-iqx)\right] \quad (4.2)$$

concentration of electrons in the conduction band n(x) is given by:

$$n(x) = n_0 + \frac{n_0}{2}\left[a\exp(iqx) + a^*\exp(-iqx)\right] \quad (4.3)$$

the density of positively charged acceptor centers $N_A(x)$ is given by:

$$N_A(x) = N_A + \frac{N_A}{2}\left[A\exp(iqx) + A^*\exp(-iqx)\right] \quad (4.4)$$

and also other spatially periodic values relevant to the process, namely, charge density $\rho(x)$, current density j(x) [16]. Higher spatial harmonics were neglected taking into account that $|m| << 1$.

The basic equation that gives the time evolution of the complex amplitude of the electric filed grating E_{sc} can be obtained through a self-consistent solution of a set of equations [12, 13, 16, 17]:

Poisson equation

$$\frac{\partial E_{sc}(x)}{\partial x} = \frac{1}{\varepsilon_0\varepsilon}\rho(x) \quad (4.5)$$

continuity equation

$$\frac{\partial \rho(x)}{\partial x} = -\frac{\partial j(x)}{\partial x} \tag{4.6}$$

current density is a sum of three components : the drift, diffusion, and photovoltaic

$$j(x) = e\mu n(x)E(x) + eD\frac{\partial n(x)}{\partial x} + \alpha GI(x) \tag{4.7}$$

rate equation

$$\frac{\partial n(x)}{\partial t} = g(x) - \frac{1}{\tau}n(x) + \frac{1}{e}\frac{\partial j(x)}{\partial x} \tag{4.8}$$

where e is the charge of electron, D is diffusion coefficient, μ is the mobility, α is the optical absorption coefficient, and G is Glass constant characterizing the photovoltaic effect. For ferroelectric crystals (for polar crystals) an essential mechanism that controls the electron transport in the absence of the electric field is the photovoltaic effect [3, 4]. The physics of the phenomenon is that the probability of the excited electron motion in one or another direction is anisotropic, and a preferred electron motion generates a resulting electromagnetic field. The important conditions for the photovoltaic effect to arise are that the photoactive center itself be spatially asymmetric, that it has a dipole moment, and that such centers be preferentially oriented to prevent the total averaging of the directions of the photoexcited electron transfer. Equally important contributions to the photorefractive effect come from the anisotropy of carrier recombinations, scattering anisotropy. Such conditions exist in polar crystals. In this thesis we will consider just the crystals in which only diffusion mechanism of grating recording (birefringent photorefractive crystals) dominates. Therefore we will neglect the photovoltaic effect, and we will assume that the external electric field is not applied E_o=0.

We will neglect the contribution of mobile electrons to the amplitude of hologram electric field i.e. we assume that the lifetime of a photoelectron τ is much shorter than the characteristic time of hologram recording τ_{sc} ($\tau \ll \tau_{sc}$). Then using the equations (4.1)-(4.8) we find the expression for the hologram complex amplitude [16, 17]:

$$\frac{\partial E_{sc}}{\partial t} = -\frac{imE_D + E_{sc}(1+q^2r_D^2)}{\tau_M(1+q^2L_D^2)} \tag{4.9}$$

where $E_D = qD/\mu = k_BTq/e$ is the diffusion field (T is the temperature), $L_D = \sqrt{D\tau}$ is the photoelectron diffusion length, $r_D = \sqrt{\varepsilon\varepsilon_0 k_B T/(e^2 N_A)}$ is the Debye screening length (k_B is Boltzmann's constant), and $\tau_M = \varepsilon\varepsilon_0/(e\mu n_0)$ is the Maxwell relaxation time. The physical meaning of the Debye screening length is well-known [16]. It's a typical steady-state depth of penetration of mobile charge carriers into the dark region of the crystal illuminated by a sharp light-to-dark transition. The hologram amplitude for the steady-state regime of recording $\left(\frac{dE_{sc}}{dt} = 0\right)$ is given by:

$$E_{sc} = -\frac{imE_D}{1+q^2r_D^2} \tag{4.10}$$

Equation (4.10) also predicts saturation of the acceptor traps (i.e. violation of the quasi-neutrality condition) and stationary hologram amplitude in the case when $qr_D \geq 1$ for diffusion holographic recording.

Taking m=0 we obtain an equation describing optical erasure:

$$\frac{\partial E_{sc}}{\partial t} = -\frac{E_{sc}(1+q^2r_D^2)}{\tau_M(1+q^2L_D^2)} \tag{4.11}$$

with a decay time:

$$\tau_d = -\frac{\tau_M(1+q^2L_D^2)}{(1+q^2r_D^2)} \tag{4.12}$$

We will make an assumption that $qL_D \ll 1$ because the average electron lifetime in the conduction band is rather short $\tau \approx 10^{-6} \div 10^{-9}$ seconds, and also of the low electron mobility in this material [16, 17]. We rewrite Eq. 4.12 for decay time as

$$\tau_d = -\frac{\tau_M}{(1+q^2r_D^2)} \tag{4.13}$$

4.2 Stimulated Diffusion Backscattering (SDS)

4.2.1 Reflection gratings

Photorefractive waves mixing processes are usually associated with dynamic gratings of transmission type, i.e. the gratings which are recorded by codirectional coupling of coherent beams, Fig.4.2(a). This is due to the Debye screening effect [16, 17] that restricts a minimal period Λ of grating fringes by the condition $\Lambda \geq r_D$, where $r_D = \sqrt{\varepsilon\varepsilon_0 k_B T / e^2 N_A}$ is the Debye length which is given by a density N_A of trapping centers in the material. Normally $N_A \approx 10^{15}$-10^{16} cm^{-3} and $r_D \geq 0{,}5$ μm so that the reflection gratings spacing $\Lambda \approx \lambda/2n \approx 0{,}1$ μm, see Fig.4.2(b), is usually much shorter. Nevertheless both theoretical and experimental aspects of the two-wave mixing problem for reflection gratings were studied [76-90, 103, 104].

First experiment of effective two-wave mixing in the backward geometry was made in ref. [58]. Nonlinear backscattering was observed at illuminating Fe:$LiNbO_3$ crystal by a pump beam, which propagated along $\vec{C}$ - axis of the crystal. The backward wave was originated from linear reflection of the pump at the facet of the crystal.

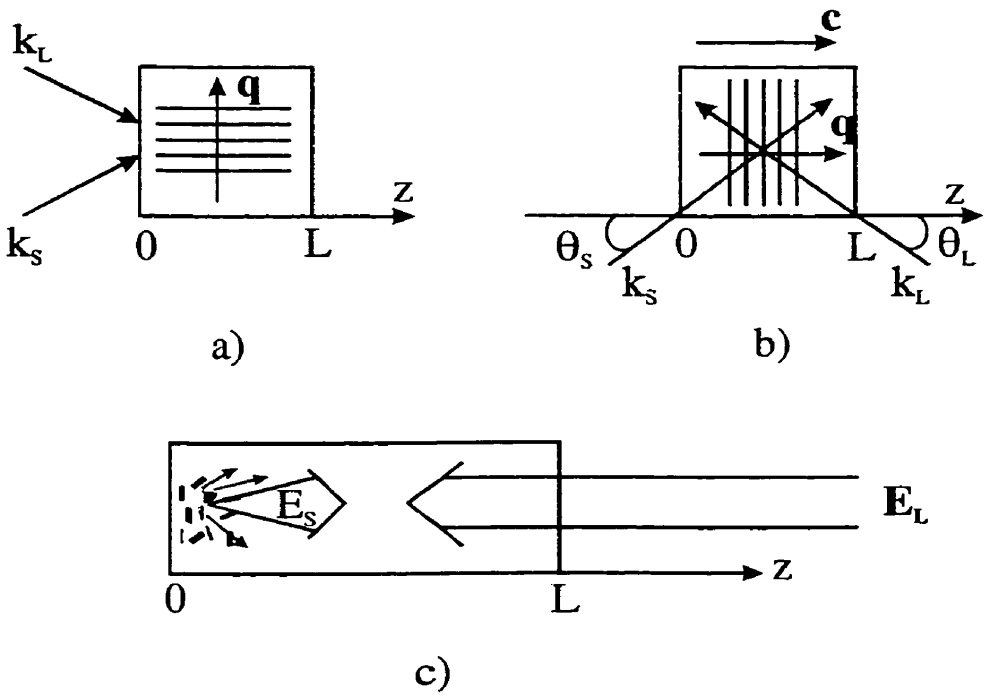

Figure 4.2 a) Transmission grating geometry; b)reflection grating geometry; c) stimulated backscattering geometry.

Stimulated diffusion backscattering (SDS) is similar to the well-known stimulated Brillouin backscattering (SBS) [8, 10]. Both SBS and SDS, can be explained as two-wave mixing process which takes place via $\pi/2$-shifted [3] dynamic gratings. Therefore it is accompanied by energy exchange between two participating beams. Energy exchange results in a sharp exponential growth of the backward signal beam at the expense of the pump beam. Note, that the reflected signal is self-generated inside a sample. It is seeded at an extremely low level by spontaneous scattering of the pump beam at medium nonuniformities (see Fig.4.2(c)).

Self-reflection takes place due to efficient two-wave coupling between the small backward signal and the pump beam. All experimental results of different scientific groups [82-106] directly indicate that the dynamic gain at the contradirectional geometry of the two-wave mixing can be very strong. Furthermore, linear absorption does not affect the process in some crystals such as $LiNbO_3$:Fe, $KNbO_3$:Fe and $BaTiO_3$.

4.2.2 Stimulated Brillouin Scattering (SBS) versus Stimulated Diffusion Backscattering (SDS)

For SBS a running hypersound wave serves as the dynamic grating and the signal beam is frequency shifted. For SBS the signal beam originates from thermal fluctuations of a medium density while for SDS the corresponding grating does not move in space. It is produced by a light-induced charge separation which is produced by diffusion of free carriers. It results in spatially modulated electric field. SDS process is frequency degenerated and seeded by scattering at static defects of a crystal either at its surface or in the bulk. The main observable consequence of this difference is that the reflected signal in SBS is frequency shifted (at about GHz) but SDS does not demonstrate any frequency shift at accuracy about Hz [91].

Second difference is in the physical nature of the medium excitation. For SBS the steady-state local gain is directly proportional to the local pump intensity [8]. But for SDS it is normally a constant, which depends on beam's orientations with respect to optical axes of the crystal. At the same time, for SBS the hypersonic grating decay time is intensity independent and it is a constant of the material, which depends only on a grating spacing. For SDS the electric field grating decay time depends on crystal conductivity and therefore, it is usually inversely proportional to local instantaneous pump intensity.

The main consequence of the gain independence on intensity for SDS is that the effect of stimulated backscattering can be observed even at low pump intensity using cw pump beam with several mW. It is very unusual comparing to SBS case where backscattering effect can be attained at very high pump power to exceed the threshold of SBS (about several MW). The photorefractive backscattering does not have an intensity threshold. Nevertheless, it demonstrates some threshold which related to the dopant densities, crystal orientation with respect to the pump beam, and pump polarization state.

Note also that for SBS a typical time, which takes for grating relaxation, is about several nanoseconds (in visible and in near infrared regions) [8]. For SDS at cw pumping

intensity which is equal to about 1 W/cm^2 the dielectric relaxation time of grating decay is about several seconds (depending on a particular material). We could compare typical energy $P\tau$ that is required to start stimulated scattering processes in both cases. For SBS the threshold power is $P_{th} \sim 10^5$-10^6 W, the hypersound relaxation time is $\tau \approx 10^{-8}$ s. For SDS the product of a pump power and the relaxation time is equal to 0.1-10 mJ i.e. the results are very comparable for both cases [8, 82-86].

4.2.3 Physical origin of SDS

Stimulated diffusion backscattering is a particular case of the well-known fanning effect [16, 17] but in backward direction with respect to a wavevector of the pump beam. Both the fanning and SDS are initiated by the frequency degenerated seed of spontaneous scattering of the pump in crystal microdefects. Both the fanning and SDS effects are observed due to very high amplification of this spontaneous seed at the expense of the pump wave. This amplification is stimulated by the pump wave via dynamic gratings which are recorded due to interference of the pump and scattered signal in a nonlinear crystal and which provide power transfer from pump to signal. Sometimes effects of dynamic amplification of scattered waves in photorefractive crystals are unified by a common term "photorefractive stimulated scattering" [92].

As we already mentioned above the space-charge gratings in the crystals could be originated by three different charge transfer processes - diffusion, drift and photovoltaic current [16]. The drift mechanism is usually effective for samples with external electric field applied. The latter is used to increase the photorefractive response time for materials with low electrooptical coefficients (such as selinits and semiconductors). Two other mechanisms can be easily distinguished in a steady-state of any two-wave mixing process. The diffusion response corresponds to $\pi/2$-shift of material gratings with respect to the light interference pattern while photovoltaic gratings correspond to local type of recording [16, 17]. As it is well known the steady state frequency degenerated energy transfer via two-wave mixing is possible only for spatially shifted photorefractive gratings [16]. SDS experiments, which will be

discussed in this thesis, correspond to materials and geometries that demonstrate maximal reflectivity in the steady-state i.e. SDS with purely diffusion gratings. Beside that, for $BaTiO_3$ and $KNbO_3$ crystals where this effect had been observed the photovoltaic effect is negligibly small [16, 17].

4.2.4 Interaction equations and advantages of reflection gratings

We consider two plane waves, the pump beam $E_L e^{-i\omega t+i\vec{k}_L\vec{R}}$ and the signal beam $E_S e^{-i\omega t+i\vec{k}_S\vec{R}}$, which are coupled by means of a first spatial harmonic of the $\pi/2$-shifted diffusion type volume grating $Q_1(\vec{R}) \propto E_L^* E_S e^{i\vec{q}\vec{R}}$, $\vec{q} = \vec{k}_S - \vec{k}_L$. For reflection gratings ($\vec{n}_S = -\vec{n}_L$ where $\vec{n}_{L,S} = \vec{k}_{L,S}/|k|$) where z-axis is chosen along $\vec{n}_S$ we have [16]:

$$\frac{\partial E_S}{\partial z} = Q_1 E_L, \quad \frac{\partial E_L}{\partial z} = Q_1^* E_S \tag{4.14}$$

Within the frameworks of the most common zone model, the relaxation equation of the first order for diffusion grating $Q(\vec{R},t)e^{i\vec{q}\vec{R}} + c.c.$, which is excited by the interference patter $E_L^* E_S e^{i\vec{q}\vec{R}} + c.c.$, is given by [16]:

$$\frac{\partial Q}{\partial t} + \xi[I_d + I(\vec{R})]Q(\vec{R},t) = \xi(\Gamma/2)E_L^* E_S \tag{4.15}$$

where $\xi(I_d + I) = \tau_{di}^{-1}$ is the relaxation rate, which is directly proportional to the crystal conductivity, Γ is the steady-state two-wave coupling gain. The crystal conductivity σ includes two contributions: dark and photoinduced conductivities.

The grating response time for SDS is intensity dependent. If the pump wave is undepleted, $E_L \approx$const and $|E_L|^2 >> |E_S|^2$ then $\tau_{di} \approx [\xi(I_d+I_L)]^{-1}$ is constant parameter. The

response time is inversely proportional to the input pump intensity when $I_L >> I_d$. Therefore, we could control the response rate by varying pump intensity.

The grating response rate $\tau_{di}^{-1}(\vec{R})$ depends on spatial coordinates $\vec{R}$. The latter can happen evidently due to the spatial nonuniformity of the illuminating intensity profile $I(\vec{R}) = \left| E_L e^{i\vec{k}_L\vec{R}} + E_S e^{i\vec{k}_S\vec{R}} \right|^2$ and therefore the photoconductivity. The fringes of the grating $Q(\vec{R})e^{i\vec{q}\vec{R}} + \text{c.c.}$ don't have a sinusoidal profile when $I_S \sim I_L$ even for plane interacting waves. The steady-state solution of Eq.(4.15) has the form

$$Q(z)e^{i\vec{q}z} + \text{c.c.} = \frac{\Gamma}{2}\left[\frac{E_L^* E_S e^{iqz}}{I_d + I(z)} + \text{c.c.}\right] \tag{4.16}$$

where the intensity $I(z) = I_L + E_L^* E_S e^{iqz} + \text{c.c.} + I_S$ is the fast periodical function. It means that the grating (4.16) constituted by a number of spatial harmonics, $\delta\varepsilon(\vec{R}) \propto \sum_{m=-\infty}^{\infty} Q_m e^{imqz}$. The coupling efficiency for the volume grating regime (see Eq.2.9) is controlled by first harmonic $Q_1 e^{iqz}$ because it is Bragg-matched.

Another point to mention is that for transient regime different spatial harmonics, as it is seen from the Eq.(4.15), are growing at different rates. They are dependent on a contrast $m = 2|E_L E_S|/(I_L + I_S)$ of the local interference pattern. Thus the build-up dynamics at pump depletion is much more complicated than the one described by first order temporal equation at constant response rate as it takes place for SBS. The steady state two-wave coupling in the plane-wave model is described using the following set of equations:

$$\frac{dE_s}{dz} = Q_1 E_L, \quad \frac{dE_L}{dz} = Q_1^* E_s, \quad Q_1 = \frac{1}{(2\pi/q)}\int_0^{2\pi/q}\left[Q(z)e^{iqz} + \text{c.c.}\right]e^{-iqz}dz \tag{4.17}$$

where the harmonic amplitude Q_1 is defined by a weighted integration of the grating fringe profile over the grating period $\Lambda=2\pi/q$.

To simplify the problem different approximations are used. The simplest and the most common approach is to neglect in the denominator of the right-hand-side of the Eq.(4.16) both the dark conductivity contribution and the interference modulation term. Then we have, from Eqs.(4.17):

$$\frac{dE_S}{dz}=\frac{\Gamma}{2}\frac{I_L}{I_L+I_S}E_S, \quad \frac{dE_L}{dz}=\frac{\Gamma}{2}\frac{I_S}{I_L+I_S}E_L \tag{4.18}$$

Eq. (4.18) are only valid for low contrast conditions and for high intensity of the pump beam. Nevertheless, they are actively utilized for analysis of pump depleted situations as well [12, 103, 104]. Unfortunately it is done without any justifying discussions so that a degree of actual applicability of such theoretical results is not clear enough.

More sophisticated approach, see for instance [92] for the transmission gratings, deals with taking the interference modulation of the response rate into account. Integration of (4.17) with Q(z) from (4.16) and neglecting I_d results easily in the following couple of the equations

$$\frac{dE_S}{dz}=\frac{\Gamma}{2}\frac{\hat{O}}{|E_S|^2}E_S, \quad \frac{dE_L}{dz}=\frac{\Gamma}{2}\frac{\hat{O}}{|E_L|^2}E_L, \quad \hat{O}=\min\left(|E_L|^2,|E_S|^2\right) \tag{4.19}$$

instead of the Eq. (4.18). If the amplified signal wave E_S is not seeded from the outside but appears as backward SDS then $|E_L|^2>|E_S|^2$ over the whole sample. In this case Eq.(4.19) results in the modified nonlinear system:

$$\frac{dE_S}{dz}=\frac{\Gamma}{2}E_S, \quad \frac{dE_L}{dz}=\frac{\Gamma}{2}\frac{|E_S|^2}{|E_L|^2}E_L \tag{4.20}$$

These equations give purely exponential solution for the signal wave spatial growth even in the conditions of the pump depletion: $E_S(z) = E_S(0)\exp(\Gamma z/2)$.

We can easily see that the difference between the simplest system (4.18) and the system (4.19) is noticeable at $I_S \sim I_L$. The most interesting point is that this enhancement of the equations accuracy resulted in optimistic predictions to increase the coupling efficiency. Indeed, the system (4.18) gives the exponential gain for the signal at $I_L \approx I_S$. And this gain is two times smaller than the gain within the frameworks of the more delicate system (4.19). The corresponding enhancement of coupling at high contrast were demonstrated experimentally, see for example [19].

However the effect of the dark conductivity to this enhancement hadn't still been discussed in the literature for reflection gratings geometry. As we will see below in the experimental results the dark conductivity contribution can be very critical for phase conjugation ability of SDS.

The last step we have to elucidate formulating a theoretical part of the problem is a generalization of the plane wave equations for the case of the spatially structured interacting waves, i.e. taking into account three additional factors: diffraction of the waves, angular dependence of the gain Γ and spatial nonuniformity of the local response rate. The last factor is easily taken into account if we will adopt that a pattern of the photoconductivity and the response rate, $\tau_{di}^{-1}(\vec{R})$, is spatially modulated because both $I_L(R)$ and $I_S(R)$ contributions are dependent on spatially coordinates R.

As far as the diffraction process is concerned we can use the parabolic equation approximation [8, 92]. This approximation used for description of small-distant propagation of beams with a small divergence. Both these conditions are valid for SDS actual experiments: the interaction length is short, $L \leq 0{,}5$ cm, and the divergence inside a crystal is also small enough, $\Delta\theta \leq 3.10^{-2}$. The terms in phase increments which are neglected in the parabolic

approximation [8] are here very small even at highest values of these parameters: $\delta\varphi \sim n\frac{\omega}{c}\Delta\theta^4 L \le 0{,}1$.

If one or both of the counter-propagating waves consist of many angular components then the resulting dynamic grating $Q(\vec{R})e^{iqz}$ can be presented as a superposition of elementary gratings. These gratings recorded by pair of elementary plane wave components from different waves which aren't strictly counter-propagating. The gain is a function of both wavevectors $\bar{q}$ and their orientation [16] and it results in differences in gains for different pairs. We will show that for the conditions of our experiment this angular dependence of gain Γ is very smooth and gain Γ can be taken as a constant for any pair of separate angular components.

There are two different contributions to this dependence. First of them is related to the dependence of the amplitude of the electric field E_{sc} of the space-charge grating on the spacing Λ, see Eq. 4.10:

$$E_{sc} = \frac{2qr_D}{1+(qr_D)^2}E_{max}, \quad E_{max} = \frac{k_B T}{e}\frac{1}{2r_D} \tag{4.21}$$

For our samples used, which are heavily doped, the parameter qr_D for reflection gratings $qr_D \approx 2n\frac{\omega}{c}r_D$ is close to unity. It means that E_D is very close to its maximum value E_{max} and the derivative $\frac{dE_q/dq}{E_{max}r_D} \ll 1$. At the same time for the contrapropagation geometry some angular variations $\delta\theta$ of components directions with respect to z-axis result in very tiny variations of the wavenumber of the corresponding gratings, $\delta q = q\delta\theta^2$. Note that the corresponding spread δq is much smaller here than for the transmission geometry where δq is of the first order of $\delta\theta$. In the conditions of typical SDS experiments $\delta\theta$ is hardly higher than 3.10^{-2} and thus the

relative variations of the elementary gratings electric field amplitude due to the angular spread in propagation directions is very small: $\frac{\delta E_{sc}}{E_{sc}} \leq 10^{-3}$.

The second factor concerns an angular dependence of effective electrooptical coefficient r_{eff} which is proportional to the refractive index variation $\delta n(\bar{R}) = r_{eff} E_{sc}(\bar{R})$. The parameter r_{eff} depends on many factors including values of components of the electrooptical tensor of the crystal, orientations of the participating waves and their states of polarization. All these factors are specified for any particular interaction. In our case such specification is rather obvious because all known experiments on SDS, as well as those which will be discussed in this thesis, were made using the same geometry for all crystals. These geometries shown in the Fig.4.2 (b) where both directions $\bar{k}_L$ and $\bar{k}_s$ are positioned near z-axis of the crystal, and $\theta_L << 1$, $\theta_S << 1$. For this geometry and for x-polarized beams (that produces for the $KNbO_3$ crystal the highest gain) r_{eff} can be presented as [16]:

$$r_{eff} \approx -\left[r_{13} \cos\theta_L \cos\theta_S - 2r_{42} \sin\left(\frac{\theta_L + \theta_S}{2} \right) + r_{33} \sin\theta_L \sin\theta_S \right] \qquad (4.22)$$

At small angles θ_L and θ_S, the first term in the right-hand-side of Eq.(4.22) will be dominant. However for the most interesting samples, such as $KNbO_3$ and $BaTiO_3$, the situation is more complicated since $r_{42} >> r_{13}, r_{33}$. As a result the term proportional to r_{42} can be effective even at small angles. In particular, for $BaTiO_3$ [16, 17] where $r_{13} \approx 8$ pm/V, $r_{33} \approx 28$ pm/V, and $r_{42} \approx 820$ pm/V, the parameter r_{eff} even changes its sign at $\theta_L \approx \theta_S \approx 5°$.

In the experiments presented in this thesis Fe:$KNbO_3$ sample is used in the geometry of Fig.4.2 (b),(c). For $KNbO_3$ crystals the difference between r_{13} and r_{42} isn't tremendously high [106]: $r_{13} \approx 20$ pm/V, $r_{33} \approx 35$ pm/V, $r_{42} \approx 360$ pm/V and the angular dependence $r_{eff}(\theta_L, \theta_S)$ is much smoother than for $BaTiO_3$ crystal. In our case both θ_L and θ_S are not higher than 3.10^{-2} rad, then an effective electrooptical coefficient is constant for all angles used and $r_{eff} \approx r_{13}$ at accuracy about several percents.

We may conclude that all elementary plane-wave gratings that contribute to the reflection grating of two waves $E_L(\vec{R})e^{-ikz}$ and $E_S(\vec{R})e^{ikz}$ are presented with the same weight. It means that in the right-hand side of the interaction equations instead of Fourier-convolution operator one may use the same expressions for grating amplitude. It was derived for plane interacting waves implying that the wave amplitudes $E_L(\vec{R})$ and $E_S(\vec{R})$, which control the local grating amplitude $Q(\vec{R})$, are slow functions of the spatial coordinate $\vec{R}$.

The resulting interaction equations can be presented in the steady state as:

$$\frac{\partial E_S}{\partial z}-\frac{i}{2k}\Delta_\perp E_S = Q_1(\vec{R})E_L, \quad \frac{\partial E_L}{\partial z}+\frac{i}{2k}\Delta_\perp E_L = Q_1^*(\vec{R})E_S,$$
$$Q_1(\vec{R}) = \frac{1}{\Lambda}\int_0^{\Lambda}\left(Q(\vec{R})e^{iqz}+\text{c.c.}\right)e^{-iqz}dz, \tag{4.23}$$
$$Q(\vec{R}) = \frac{\Gamma}{2}\frac{E_L^*(\vec{R})E_S(\vec{R})}{I_d+|E_L|^2+E_L^*E_S e^{iqz}+E_L E_S^* e^{-iqz}+|E_S|^2}$$

where Γ is the steady-state two wave coupling gain that could be observed at zero dark conductivity, at undepleted pump and at precisely counter-propagating signal. Several simplified versions of this most general system had been proposed and used earlier [91, 103-105].

4.2.5 Choice of the crystal

Until now effective enough reflection gratings were reported for four types of photorefractive crystals: $LiNbO_3$ [58, 86], $BaTiO_3$ [83, 86, 92], $KNbO_3$ [87, 105] and SBN [81]. All crystals used were either heavily doped or annealed to reduce the Debye radius. We will further justify the choice of our crystal.

$LiNbO_3$ is very distributed and rather cheap crystal. It demonstrates, at heavy iron doping, very good reflectivity even in the self-seeded SDS geometry, see Fig 4.2 (c). It is due

to, obviously, rather high photorefractive gain along with low absorption. However the photoconductivity is very small in such samples and the resulting build-up time is extremely high, up to tens of minutes at about 0,1 W incident power, resulting in very low sensitivity and demonstrating no practical value.

SBN samples, at least at doping by Rh, are able to provide the contra-directional coupling gain up to 15 cm^{-1} [81]. Unfortunately it is accompanied by very strong absorption in visible region that significantly decrease the output efficiency making this sample of low value from the practical point of view as well.

The experiments definitely show that two types of crystals $BaTiO_3$ and $KNbO_3$ are the most effective ones. The evident advantage of $BaTiO_3$ is that it could be able to provide highest possible gain at oblique propagation having the highest electrooptical coefficient r_{42}. $BaTiO_3$ at Rh doping can, beside that, be more sensitive in the near infrared region [116, 117]. However $KNbO_3$ is usually faster, at least in visible region, comparing to $BaTiO_3$. Depending on particular samples and on a procedure of their treatment a difference in a dielectric relaxation time τ_{di} between $BaTiO_3$ and $KNbO_3$ can amount from about ten to about thousand or even more, see for example [16, 17, 82, 108].

Our choice was the iron doped $KNbO_3$ crystal. The gain for contra-directional geometry at beams propagation along $\bar{C}$ - axis was high enough in our sample in visible region to observe SDS in the pump depletion regime even at spontaneous seed.

4.2.6 Advantages of SDS geometry

For phase conjugation and signal processing applications of photorefractive wave mixings, the crystal sensitivity is the key parameter. It controls the condition of switching of operation and speed of operation. Below we present arguments that the conter-directional geometry (reflection gratings) has lower sensitivity and higher gain than the transmission gratings geometry. For photorefractive crystals the grating response rate is given mostly by the

dielectric relaxation time τ_{di} which is, roughly, inversely proportional to illumination intensity I. Thus we must compare the pump energy density $I\tau_{di}$, which is independent on intensity.

The sensitivity of a non-threshold signal processing device is characterized by the value $I\tau_{di}$, i.e. by the τ_{di} at intensity of 1 W/cm^2. For devices that are based on instability, like photorefractive PC generators, the response rate can be enhanced or reduced depending on a relative excess over a threshold. The latter is controlled by an absolute value of the steady-state total gain ΓL parameter. Anyway, to increase sensitivity one has to decrease dielectric relaxation time τ_{di} but to increase the steady state total gain ΓL.

It is well known that both these parameters depend on the grating spacing $\Lambda=2\pi/q$ in the following manner [section 4.1]:

$$\tau_{di} \propto \frac{1}{(1+q^2 r_D^2)}, \quad \Gamma \propto \frac{q r_D}{1+q^2 r_D^2} \tag{4.24}$$

Reflection gratings correspond to the shortest spacing $\Lambda_{min}=\pi/k$ possible at given wavelength. Thus for reflection gratings the dielectric relaxation time τ_{di} is always shorter than for the transmission gratings. And this effect is most essential at $q \geq r_D^{-1}$ where the rate enhancement factor can achieve several times. The right-hand-side function for the steady state total gain ΓL in (4.24) is also growing with q up to a value $q = r_D^{-1}$, and then it drops with q. Equations (4.24) indicate that if $2kr_D \sim 1$, just the reflection gratings are preferable providing both shortest τ_{di} and highest gain.

The optimal situation, $r_D \approx (2k)^{-1} \approx 0.1-0.2\,\mu$m, requires samples of rather high density N_A of effective trapping centers, up to $N_A \sim 10^{17}$ cm^{-3}, since $r_D \propto N_A^{-1/2}$. It is usually achieved by doping or annealing procedures that is accompanied by some additional effects. It seems that rather serious and independent study of the effect of impurities on both response rate and gain would be very desirable for each particular material and impurity. Additional density of impurities increase, first of all, maximal possible density of trapped charge, $N_A e$. It

decreases, as we already mentioned above the Debye radius. However this desirable effect is evidently accompanied by a drop of a free carriers lifetime τ_e which, for the case of linear recombination, is inversely proportional to N_A. At fixed absorption and quantum efficiency of photoionization it would result in the drop of photoconductivity and, as a consequence, in the drop of the response rate since $\tau_{sc} \propto \sigma^{-1} \propto \tau_e^{-1}$.

However additional impurities are usually responsible also for additional absorption which is proportional to impurity densities. If this additional absorption leads also to photoconductivity it will evidently increase a rate of photocarriers generation and make it proportional to impurity densities. In this case the drop of the lifetime can be completely compensated by the growth of the photoionization rate. In this case τ_{sc}, at a given I, will be independent on doping density. However, there is also rather negative effect of additional doping: the growth of linear absorption increases thresholds of devices and decreases their efficiency due to losses of light energy and transformation of this energy into heat.

4.2.7 Geometrical factor

Another advantage of reflection gratings is connected to pure geometrical conditions of interactions of focused pump beams, i.e. the situation when the length of the interaction area is much higher than its width restricted by beams' diameter, Fig.4.3. Strong focusing is very desirable which provides higher illumination intensity and, therefore, smaller dielectric relaxation time of the gratings and a device itself.

There are two aspect of this problem which both are related to the dependence of the two-wave coupling gain Γ on the angle θ between directions of the beams, Eq.(4.24). The grating wavenumber q can be expressed as the function of the angle θ between the waves for the transmission geometry, or as the function of the angle of counter-propagation also denoted here as θ, Fig.2.2. At small angles $q \approx 2k\sin\theta/2 \approx k\theta$ for transmission gratings, and

$q = 2k\cos(\theta/4) = 2k(1-\theta^2/32)$ reflection gratings. Gain is approximately proportional to θ for transmission gratings, but it is θ - independent for reflection gratings:

$$\Gamma_{tr} \approx \Gamma_{max} 2(\theta/\theta_D), \quad \Gamma_{refl} \approx \Gamma_{max} \frac{4kr_D}{1+4(kr_D)^2} \tag{4.25}$$

where $\theta_D = (kr_D)^{-1}$.

To provide sufficient gain Γ via transmission gratings we have to choose high enough angle θ. But if this angle is higher than d/L, Fig.4.3, the actual length l of beams coupling is much shorter than the crystal thickness L: $l=d/\sin\theta \approx d/\theta$. Therefore, the total gain Γl, which control the efficiency of coupling, is limited by the value $\Gamma l = \Gamma(2\theta/\theta_D)(d/\theta) = 2\Gamma d/\theta_D$. Then, in the interval $d/L \le \theta \le \theta_D$ this total gain is practically independent on the angle. Thus, to provide effective transmission gratings coupling at a proper optimal angle and long interaction distance we have to avoid sharp focusing and to utilize wide enough beams that evidently result in a failure of the device response rate.

For the reflection gratings, gain is a constant at any counter-propagation angles θ. So we can easily choose this angle small enough to provide highest interaction length l=L. Note that for phase conjugate experiments the angle θ of the counter-propagation is zero that automatically results in maximal possible total gain. It means that the fundamental limit for a strength of focusing for the reflection gratings is to embed the beam's neck into the sample, $d_{min} \approx \sqrt{L\lambda}$, that for common samples gives $d_{min} \sim 10^{-2}$ cm. It corresponds to about 100 times additional enhancement of the response rate comparing to transmission gratings interactions where beams diameters are normally about 1 mm. In practice however such strong focusing is not available, at least for multi-waves interactions, since it creates serious problems with a set-up adjustment. Usually $d \approx 0{,}3$ mm is the most convenient diameter and the enhancement factor, in this case, is equal to about ten. Nevertheless, for self-seeded SDS such a strong focusing does not create any problems providing good beams overlapping at any focusing and gives as a result the fastest nonlinear retroreflection.

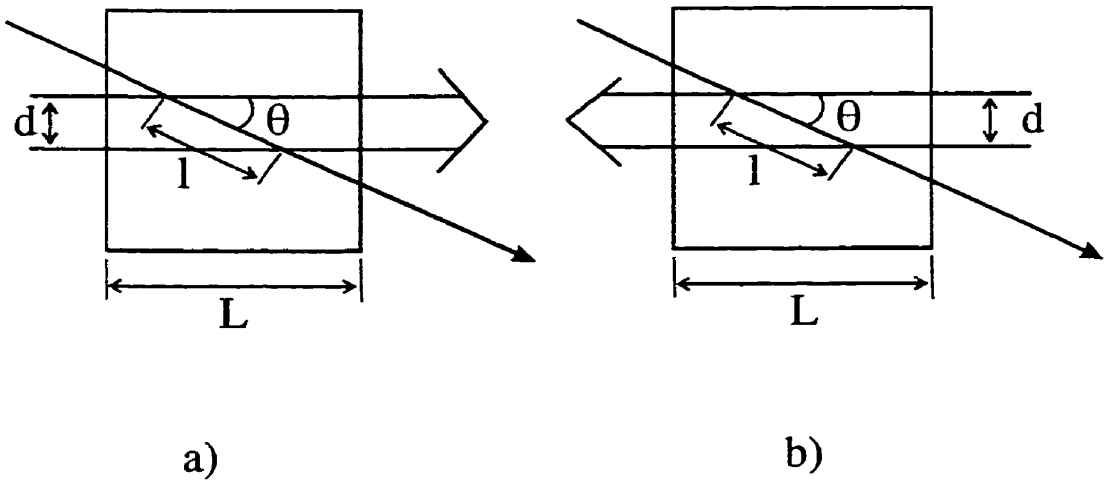

Figure 4.3 a) Transmission grating; b) reflection grating

Second aspect of the geometrical factor concerns an efficiency of the fanning waves generation. The fanning waves can compete with a radiation directed into feedback generation channel for pump wave energy. Hence, they can decrease a generation efficiency [17]. They also can create coherent speckle noise at amplified images [17] reducing its quality. This fanning problem is important for the most interesting interaction geometries with high total gain $\Gamma L \geq 10$. This noisy fanning is effective just in directions which provide highest gain. Since the fanning is seeded by spontaneous scattering, its output power is strongly dependent on the seed power. This seed power, in turn, is directly proportional to a solid angle that corresponds to highest total gain. The difference between the transmission and reflection geometries consists in solid angles of effective fanning seed. For the reflection case due to the gain independence on θ for $\theta > d/L$ a total gain Γl drops approximately as θ^{-1}, since $l = L/\theta$. As a result the effective angle of the fanning seed ΔO_f could be here very small, $\Delta O_f \approx (d/L)^2$, and it is especially small reducing total fanning efficiency at sharp focusing of the pump beam. For the transmission gratings geometry the fanning solid angle is usually much higher since it occupies almost all the range from the pump wave direction to the angles about $\theta_D = (kr_D)^{-1}$.

ΔO_f could be roughly estimated as θ_D^2 and it amounts up to 10^{-1} steradian for commercial high-gain samples.

4.3 Conclusion

In this we gave an introduction into physics of stimulated diffusion backscattering, and derived general equations, which are used in the following chapters for the theoretical study and estimates. We also made comparison between the well-known stimulated Brillouin scattering and stimulated diffusion backscattering. We performed also a comparative analysis of the reflection and transmission geometries to emphasize potential advantages of the reflection gratings. We also tried to consider the material parts of this problem, and to derive not only general prospects of the effect but also those particular directions of research, which can be interesting in future. And finally we underlined those of them, which can be studied using actual facilities of the laboratories where I worked.

All the advantages of the reflection photorefractive gratings presented in this chapter resulted in actual achievements of the practical value [81, 83-95, 100-105]. These experimental demonstrations as well as many other experiments, together with the discussion presented above, are convincing enough to pay special attention to photorefractive geometries, which utilize reflection gratings.

CHAPTER 5

EXPERIMENTAL STUDY OF STIMULATED DIFFUSION BACKSCATTERING IN PHOTOREFRACTIVE CRYSTALS

In this chapter we measured the material parameters of heavily iron doped potassium niobate samples in stimulated diffusion backscattering geometry. Specifically, we measured stimulated diffusion backscattering gains, response rate, and polarization characteristics. Dark decay effects are carefully monitored to characterize the process.

5.1 Material constants of $KNbO_3$ crystal

5.1.1 Introduction

Active investigations of the contrapropagating two-wave mixing started when it had been recognized that an effect of self-seeded nonlinear backscattering is possible [77, 82-95, 100-105]. Just the reflection gratings, which provide minimal possible fringes spacing, are responsible for maximal possible amplitude of the space-charge electric field. [9]. The reason is that, as we already discussed in chapter 4, this amplitude for heavily doped samples is inversely proportional to this spacing. Hence for the doped samples the reflection gratings are more effective compared to the transmission gratings. This statement has been included to explain extremely high nonlinear self-reflectivity observed in the works [77, 82-95, 100-105].

5.1.2 Heavily iron doped potassium niobate crystal $KNbO_3$:Fe

$KNbO_3$ is the ferroelectric oxide, with a photorefractive response caused by Fe-impurities in the energy bandgap [16]. The iron ions are in the Fe^{2+} and Fe^{3+} valence states, and act as donors for electrons or holes. The material characteristics of crystals are structures of tensor of dielectric susceptibility ε_{ij}, the electrooptical tensor r_{ijk}, as well mobility and lifetime of carriers which both define sample conductivity. Detailed information concerning tensors ε_{ij} and r_{ijk} is available in literature, see for instance [106]. Free carriers properties vary a lot from sample to sample and we believe that the most adequate way to characterize a crystal would be to measure directly a response rate.

The point group symmetry of orthorhombic phase $KNbO_3$, which is used for photorefractive applications, is mm2-C_{2v}. Such a crystalline phase is characterized by three different orthorhombic Cartesian crystallographic axes a, b, c. The axes a and c make an angle 45° with cubic axes and the c axis is parallel to the spontaneous polarization of the crystal. These orthorhombic axes correspond to eigen dielectric and optical axes of the crystal and they will be enumerated as either x, y, z or as 1, 2, 3 axes, respectively.

Both electrostatic and electrooptical properties of crystals are different for unclamped and clamped conditions and the corresponding parameters are noticed by the superscripts T and S, respectively. Low-frequency dielectric constants for $KNbO_3$ are presented in the following table [106].

ε_{11}^T	145-170	ε_{11}^S	35-39
ε_{22}^T	965-1080	ε_{22}^S	730-830
ε_{33}^T	42-60	ε_{33}^S	22-26

Table 1 Low-frequency dielectric constants for KNbO3 crystal.

The dielectric relaxation time and the Debye radius depend on dielectric constants of the crystal: $\tau_{di} = 4\pi\varepsilon^{eff}/\sigma$, and of, $r_D = \sqrt{\varepsilon_0 \varepsilon^{eff} k_B T / e^2 N_A}$, where ε^{eff} is some combination of different constants depending on grating wavevector orientation. For the photorefractive effect these constants are closer to the clamped values since the interaction volume is a small part of the sample and this part is "clamped" by the rest of the crystal. For our the grating wavevector is directed along z-axis at its tilting up to 2°-3° only. It means that in our case ε^{eff} is $\varepsilon^{eff} \approx \varepsilon_{33}^S \approx 25$. The structure of the electrooptical tensor for $KNbO_3$ is

$$\begin{pmatrix} 0 & 0 & r_{13} \\ 0 & 0 & r_{23} \\ 0 & 0 & r_{33} \\ 0 & r_{42} & 0 \\ r_{51} & 0 & 0 \\ 0 & 0 & 0 \end{pmatrix}$$

where the two-index "tensor" r_{ik} is introduced conventionally (to express in two dimensions the third rank tensors) according to the following common rule: $r_{ijk}=r_{lk}$, see Table 2:

ij	11	22	33	23	13	12
l	1	2	3	4	5	6

Table 2 Lookup table for the index l.

The corresponding values of r_{lk} are presented in table 3, see Ref. [106], in pV/m units. They were measured at λ=0,633 μm and correspond to corrected results of some rough previous measurements of the same laboratory in Zurich.

r_{13}^T	34±2	r_{13}^S	20,1±2
r_{23}^T	6±1	r_{23}^S	7,1±0,5
r_{33}^T	63,4±1	r_{33}^S	34,4±2
r_{51}^T	120±10	r_{51}^S	27,8±3
r_{42}^T	450±30	r_{42}^S	360±30

Table 3 Pockels coefficients.

These values of electrooptical coefficients are responsible for the two-wave mixing small-signal gain Γ which is calculated according to the relationship [16]:

$$\Gamma = \frac{\omega}{c} n_{eff}^3 r_{eff} E_{sc} \tag{5.1}$$

where r_{eff} depends on grating orientation and both recording beam polarizations, E_{sc} is the amplitude of the space-charge electric field grating, and n_{eff} is a refractive index. $KNbO_3$ crystals demonstrate very high optical anisotropy: n_{11}=2,28, n_{22}=2,329, n_{33}=2,169. For our particular geometry, i.e., propagation of x-polarized beams near z-axis we have $n_{eff} \approx$ 2,33 and

$r_{eff} = r_{13}^{S} = 20$, see Eq.(4.22). The sinusoidal diffusion grating amplitude is equal to mE_{SC}, where m is the grating contrast while

$$E_{sc} = \frac{k_B T}{e} \frac{q}{1+(r_D q)^2} \tag{5.2}$$

where $q = 2\frac{\omega}{c} n_{11} = 5{,}7.10^5$ cm^{-1}. Thus this value is equal to E_{sc}=14,6.v [kV/cm] at still unknown Debye screening factor $v = [1+(qr_D)^2]^{-1}$.

5.2 Coupling gain in Fe: $KNbO_3$

5.2.1 Experimental setup

We used in our experiment the sample Fe: $KNbO_3$ (0.5 Wt%) with the dimensions: 5.7: 5.05: 6.0 mm^3 along a: b: c axes, respectively. Surface reflectivity R_0 at n≈2.3 is equal to about 16%. The sample linear transmission along $\bar{C}$ axis was $(1-R_0)^2 \exp(-\alpha L) \approx 0.4$ with fluctuations about 10% from point to point. It corresponds to the absorption decrement αL≈0.6 and the absorption coefficient α=1 cm^{-1}. The setup for our experiment is presented in Fig.5.1. A cw Ar-ion laser that provides linearly polarized single-mode emission (at 0.488μm and at an output power 200 mW) was used for recording the dynamic gratings. The output beam from the laser was divided into two beams by a Glan prism. Rotating the λ/2 plate controls the intensity ratio in both beams. The lens L was installed to control diameter of interacting beams inside the crystal C. The beams were introduced into the sample by the semitransparent mirrors M_1 and M_2 which transmitted both output beams to the photodiodes PD_1 and PD_2. The system which included a λ/2 - plate and a polarizer P was used in the upper beam to make linear polarizations in both beams identical. The sample axes orientation was as it is shown in Fig.5.1(b) was made to provide a fixed direction of energy flow from the pump beam E_L into the signal one E_S. If both pump and signal are x-polarized, the signal gain is controlled by

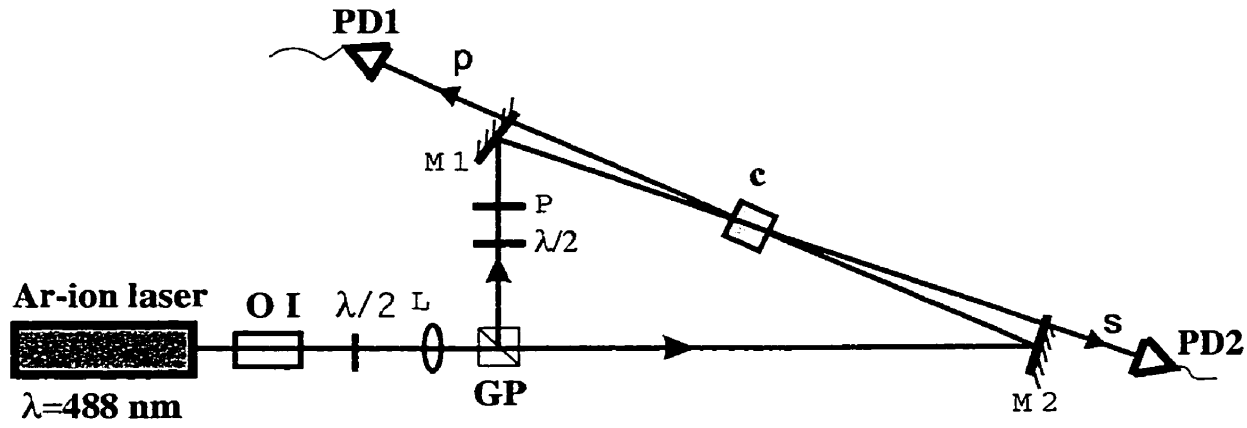

(a)

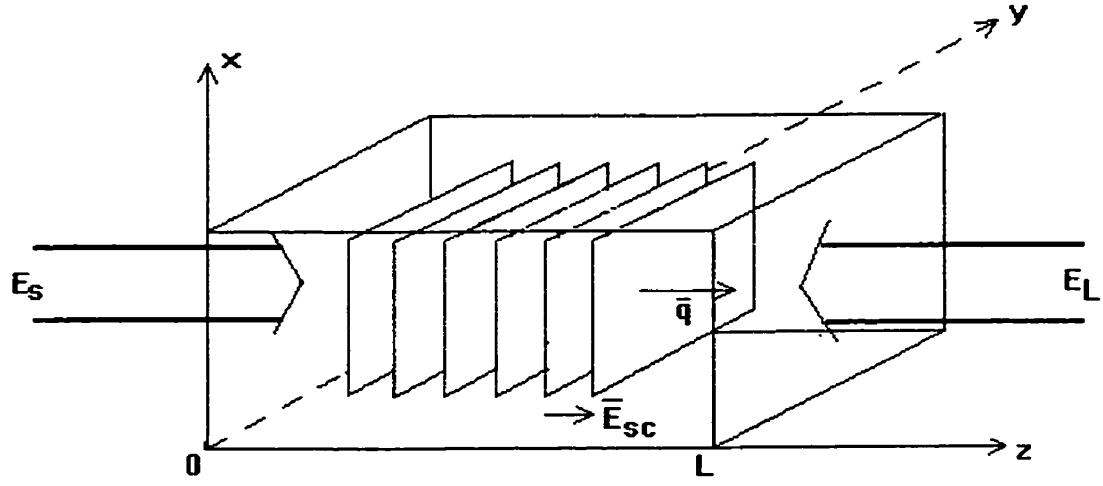

(b)

Figure 5.1 Experimental setup for two-wave coupling measurements. (a) p and s, pump and signal beams from a CW Argon ion laser (operating at 0.488 μm), respectively; OI, optical isolator; $\lambda/2$, half wave plates; L, lens; GP, Glan prism; P, polarizer; M1, M2, mirrors; c, photorefractive crystal; PD1, PD2, photodetectors. (b) Schematic presentation of the sample axes orientation; E_{SC}, the amplitude of the space-charge field; q, grating wave vector; E_L, the amplitude of the pump beam; E_S, the amplitude of the signal beam.

$r_{eff}=r_{13}\approx 2.10^{-9}$ V/cm. For y-polarized beams we have $r_{eff}=r_{23}\approx 0{,}7.10^{-9}$ V/cm. If both beams are linearly polarized along eigen directions but are orthogonal, one has $\Gamma_{xy}\propto r_{eff}=r_{63}=0$, i.e. there is no gain of the signal. For general case of mixed polarizations the eigen polarization components $\bar{e}_x$ and $\bar{e}_y$ of both pump and signal interact to the identical pair. These pairs record different gratings, for x-polarized and by y-polarized beams, separately. Such predictions can be easily verified using the scheme of Fig.5.1(a). Identical x-polarized beams and y-polarized beams wre obtained by changing orientation of x , y axes of the sample. To analyze the case of orthogonal polarizations of pump and signal beams two additional elements, a $\lambda/4$ - plate and a polarizer were introduced into the path of the pump beam.

5.2.2 Gain control by pump polarization

Let's suppose that the pump beam consists of two polarization components $\bar{E}_L = E_x\bar{e}_x + E_y\bar{e}_y$ while the signal is polarized only along the eigen direction $\bar{E}_s = E_s\bar{e}_x$. Then, if the signal intensity I_s is much smaller than the pump intensity $I_L=I_x+I_y$ and if one can neglect the dark contribution to conductivity, the steady-state gain Γ_{13} of such a signal due to its dynamic grating coupling with the x-polarization component of the pump is

$$\Gamma_{13} = \Gamma_x \frac{|E_x|^2}{|E_x|^2 + |E_y|^2} = \Gamma_x \sin^2\alpha \qquad (5.3)$$

where α - is the angle between the x - axis of the crystal and the polarization unit vector of the pump at the input. If the signal beam is polarized here along y-axis the corresponding gain Γ_{23} due to coupling of y-components will be, analogously, presented as:

$$\Gamma_{23} = \Gamma_y \frac{|E_y|^2}{|E_x|^2 + |E_y|^2} = \Gamma_y \sin^2\alpha \qquad (5.4)$$

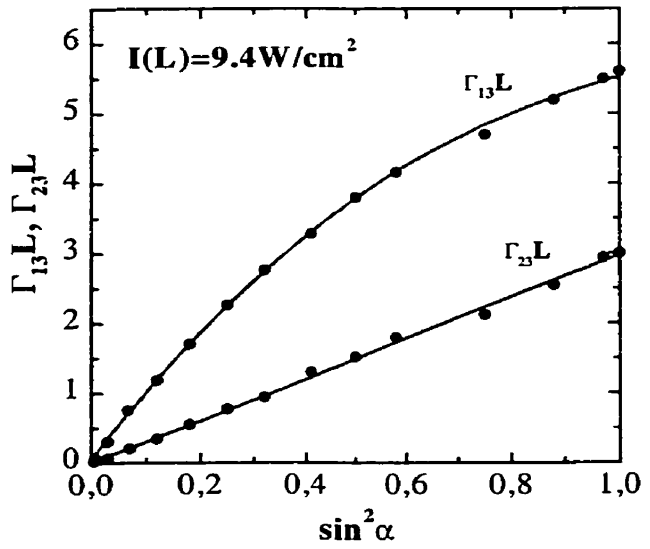

Figure 5.2 Experimental dependencies of the total gains $\Gamma_{13}L$ and $\Gamma_{23}L$ on $\sin^2\alpha$.

where α is the angle between input pump polarization and y - axis, i.e. again the angle between pump and signal input polarizations. We see that some admixture of the orthogonal alternative polarization component in the pump beam results in the drop of the gain for the linearly polarized signal. This drop can be effectively controlled by a relative ratio of this admixture power. The reason is that the alternatively polarized pumping light which does not participate in grating recording serves as a background illumination of the sample. It clearly reduces the contrast in the illumination pattern, which reduces the charges separation rate via diffusion of carriers.

Fig.5.2 demonstrates experimental dependencies for total gains $\Gamma_{13}L$ and $\Gamma_{13}L$ for x- and y-polarized signals versus $\sin^2\alpha$, where α is the angle between input linear polarizations of the incident beams. They were obtained in the conditions of a lowest possible signal intensity to minimize pump depletion effects. The total gain was measured as $\ln\left[I_s^p(L)/I_s^u(L)\right]$ where $I_s^u(L)$ corresponds to the output signal power transmitted through the sample at the

absence of pump while $I_s^p(L)$ is the same output signal power at the presence of the pump beam. These values were measured after stabilization of the build-up process. This allows us to avoid recalculations connected to linear absorption and facets reflections. For the y-polarized signal beam the coupling process took place without pump deletion. It reveals, in particularly, the linear dependence of $\Gamma_{23}L$ on $\sin^2\alpha$ with high accuracy (the experimental spread is very low, see Fig.5.2) as it would correspond just to the undepleted regime, i.e. when both (5.3) and (5.4) relations are correct. The maximal value of $\Gamma_{23}L=2.9$ or $\Gamma_y \approx 5$ cm^{-1} at L=0.6 cm. For the x-polarized signal the similar dependence of $\Gamma_{13}L$ on $\sin^2\alpha$ stays linear at small angles when the total gain is less than about 4 and the pump is not depleted. At higher angles $\Gamma_{13}L$ grows much slower and it is evidently due to pump depletion. The depletion at $\sin^2\alpha \approx 1$ occurs mostly by the fanning wave what is clearly seen in the experiment as bright background around the spot of the amplified signal. An accuracy of determination of Γ_y, which is given by the experimental spread, constituted several percents, but for Γ_x it is much lower due to the extrapolation procedure. The ratio of the corresponding values $\Gamma_x/\Gamma_y \approx 3.1 \div 3.5$. We will take the average value that gives $\Gamma_x=16.5$ cm^{-1} and for maximal total gain we have $\Gamma_x L = 10$ at about 10% accuracy. The fluctuations were about $\Delta\Gamma L \approx 1$ in the total gain for different points of a crystal cross-section, or in about the same 10% relative uncertainty, $\Delta\Gamma/\Gamma \approx 0.1$, for the gain value itself. It was also noticed that central regions of the sample provide higher gain in average than near facets.

Some interesting consequences follow from these experimental results. First, SDS gain is 15 times higher than the linear absorption, compare to the factor 3 for SBN:Rh in Ref. 81. Second, total gain which resulted in pump depletion is not so high, $\Gamma L \approx 4.5 \div 5.5$, that corresponds to the total depleting amplification about $100 \div 250$. It means that the relative seed for SDS wide-angular fanning in our sample is extremely high. It should be related to surface seed since in our sample a quality of surfaces treatment was rather poor.

5.2.3 Estimates for Debye radius of the sample

Two-wave mixing small-signal gain Γ can be calculated as (see (5.1) and [16]):

$$\Gamma = \frac{\omega}{c} n_{eff}^3 r_{eff} E_D \qquad (5.5)$$

Using the values of r_{13} and r_{23} (see Ref.18) we have $\Gamma_x \approx 45$ cm^{-1} and $\Gamma_y = 15$ cm^{-1} if E_D have taken without Debye factor $\nu = \left[1+(qr_D)^2\right]^{-1}$ which is still unknown. Both values experimentally obtained is three times smaller than the estimated theoretical values. The only factor, in our opinion, which could be responsible for such a disagreement is the Debye factor. The drop factor which is equal for both polarizations is the additional argument for it.

Thus, our measurements provided also information about the Debye factor and we could estimate the Debye radius: $(r_D q)^2 \approx 2$ and $r_D = 1.4/q = 5.5.10^{-2}\mu$m. Then the effective number of traps for our sample according to the definition of the Debye radius is: $N_A = \varepsilon_z k_B T / 4\pi e^2 r_D^2 \approx 10^{16}$ cm^{-3}.

5. 3 Intensity Dependencies of Response Rate and Gain

5.3.1 Dynamics rate measurements

Both the pump beam and the signal beam have been mechanically switched on. The starting signal intensity I_s^o grown-ups monotonously up to the steady state value I_s^{st}. We were interested in quantitative monitoring of the characteristic temporal scales and registered the time τ which is required for the signal intensity to reach 0.5 level: $I_s(T) = I_s^o + \frac{1}{2}(I_s^{st} - I_0)$. The corresponding experimental results are presented in Fig.5.3. The graph in Fig.5.3(a) corresponds to the case when both pump and signal were linearly polarized along y-axis of the crystal, i.e. the total steady-state gain $\Gamma_y L = 3$, and the input signal intensity was very low to avoid pump depletion. We choose this y-polarization geometry to decrease the total gain. As it is well known, at high total gains two-wave coupling process is slowing down

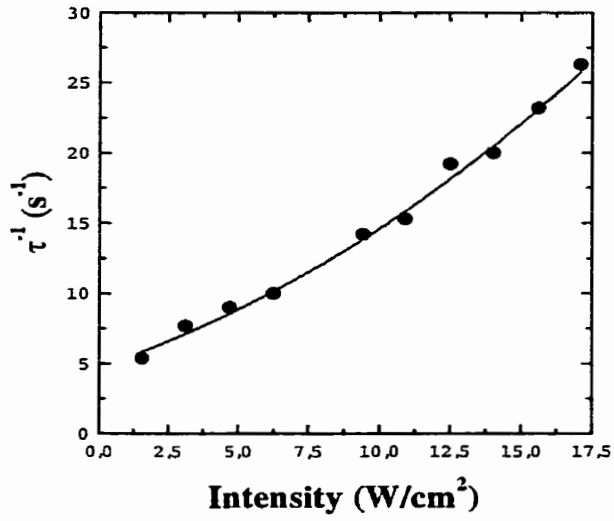

(a)

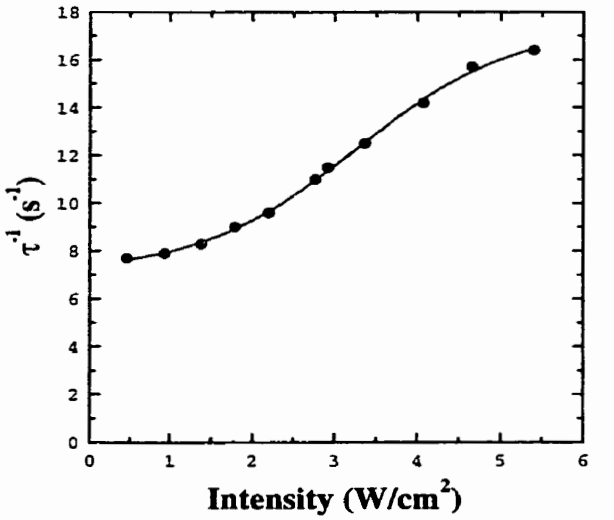

(b)

Figure 5.3 (a) Response rate as a function of pump beam intensity. Both pump and signal were linearly polarized along y axis of the crystal, (b) dielectric relaxation time as a function of pump intensity.

[8,16, 93] so that the response rate turns out to be a function of both dielectric relaxation time τ_{di} and ΓL. At very high gains the following expression could be used for estimates [8]: $\tau^{-1} \approx \left(\tau_{di}\sqrt{\Gamma L}\right)^{-1}$. In addition, the pump depletion which is unavoidable for x-polarization also violates dynamics of the process and would make an interpretation of the results rather complicated.

However, ΓL=3 turns out to be high enough to violate noticeably both the build-up dynamics and even the characteristic response time. The graph in Fig. 5.3(b) has been obtained for the conditions of additionally damped total gain. Damping has been performed by longitudinal shift of the crystal from the point of equal path length of the two legs that resulted in a drop of mutual coherence of the interacting beams. We obtained the points in Fig.5.3(b) for $\Gamma_{13}L \approx 1$. As a result just the points of Fig.5.3(b) can be directly referred to dielectric relaxation time: $\tau \approx \tau_{di}$.

The results obtained elucidate several different statements. First, the sample that we used is the rather fast, to our knowledge, comparing to other photorefractive samples reported earlier. Its speed at I_L=1 W/cm^2 corresponds to $\tau_{di} \approx 0.1$s. This based mostly on the advantages of the reflection geometry and not on outstanding properties of particular samples.

Second, at I$\rightarrow$0 the response rate τ^{-1} does not go to zero, as for the most of conventional photorefractive samples, but it stays at the finite and very high level, $\tau_{di}(I=0) \approx 0.125$ sec.., i.e., there is very high dark conductivity in our sample, $\sigma_{dark} \approx \varepsilon / 4\pi\tau_{di}(I=0) \approx 10\text{s}^{-1}$. At the same time the photoinduced conductivity contribution, as Fig.5.3 clearly demonstrates, is comparable to the dark conductivity at the illumination density I ~ 2 W/cm^2 which is unusual for photorefractive experiments.

Third, the response rate τ_{di}^{-1} intensity dependence definitely cannot be reduced to the linear dependence $\tau_{di}^{-1} = \tau_{di}^{-1}(0) + \xi I$ which is normally used and which directly follows from the simplest zone model [16]. This fact indicates that a structure of energy levels of relevant

defects in the material band-gap cannot be described as a single type of trapping centers: there could be actually many different types of trapping centers that lie at different energy levels. The simplest and the most effective model is the shallow trap model [95, 96]. We prefer to stay within the frameworks of the standard zone model [1] considering a rough zero-order approximation. We approximate the dependencies in Fig.5.3 by linear function taking

$$\tau_{di}^{-1} = \xi(I_d + I) \tag{5.6}$$

But we have some uncertainty in values of the effective parameters ξ and I_d which we have to use later. Indeed, the low intensity dependence in Fig.5.3(b) gives a rather high value $\xi \approx 2 cm^2/J$ while, and the curve for higher range of intensities in Fig.5.3(a) corresponds to low value $\xi \approx 0.6 \div 0.8$ cm^2/J. The problem of definition of I_d also arises and it results in a rather high uncertainty, $I_d \approx 2 \pm 1$ W/cm^2.

5.3.2 Gain dependence on intensity

Since the effective dark irradiance I_d is very high in our sample, it should result in a noticeable dependence on the intensity for the coupling gain and for an interaction efficiency as well. The approximate expression for Γ (I) dependence that follows from the equation (4.23) of the single trap model at $I_s << I_L$ is

$$\Gamma(I_L) \approx \Gamma_0 \frac{I_L}{I_d + I_L} \tag{5.7}$$

Fig.5.4 demonstrates this dependence for "undepleted" y-polarized pump and signal beams which was obtained using the technique described in section 3.1. Using Eq.(5.7) we obtained the fitting parameter $I_d \approx 1.5$ W/cm^2. We didn't measure similar dependence for Γ_x gain because it is much more complicated due to intensity dependent level of depletion that would decrease an accuracy of results. But we do not see any physical reasons that the dependance $\Gamma_x(I_L)$ will behave differently because $\Gamma_x/\Gamma_y = r_{13}/r_{23} = const$ at any intensity.

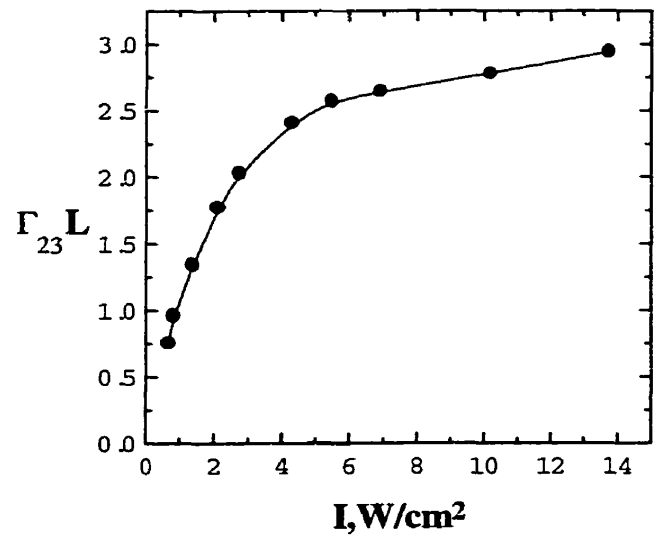

Figure 5.4 Dependence of the total gain $\Gamma_{23}L$ on the pump intensity for "undepleting" y-polarized both pump and signal beams.

We compared steady-state diffraction efficiencies η of the reflection gratings versus intensity in the two limit cases: for moderate total gain, Fig.5.5, and for gain highest values, Fig.5.6. The dependence in Fig.5.5 corresponds to a weak grating recorded by two incident waves of low-effective y-polarization. The small signal wave was taken to avoid pump depletion. The gain was also additionally damped to a level $\Gamma_{23}L\approx 1$. The resulting value of η was not higher than 2.10^{-3}. The efficiency η was measured by instantaneous blocking the signal beam after grating stabilization. The diffraction efficiency of the steady-state grating can be calculated (neglecting absorption and facets reflection) as

$$\eta \approx \varepsilon(e^{\Gamma L} - 1) \tag{5.8}$$

where ε is the relative seed $\varepsilon=I(0)/I_L(L)$. At small $\Gamma L \leq 1$ it can be approximated as $\eta \approx \varepsilon\Gamma L$ and hence $\eta(I)$ dependence has to follow Γ (I) dependence. We can see that dependencies presented in Fig.5.4 and Fig.5.5, are very similar.

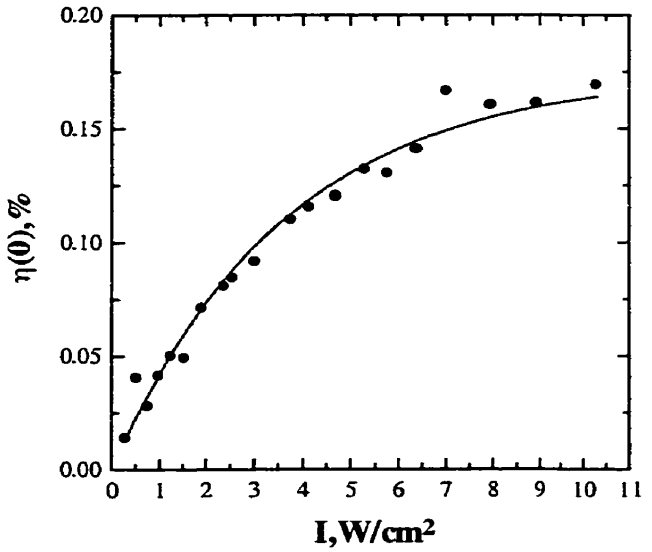

Figure 5. 5 Steady state diffraction efficiency as a function of pump intensity for moderate total gain $\Gamma_{23}L \approx 1$.

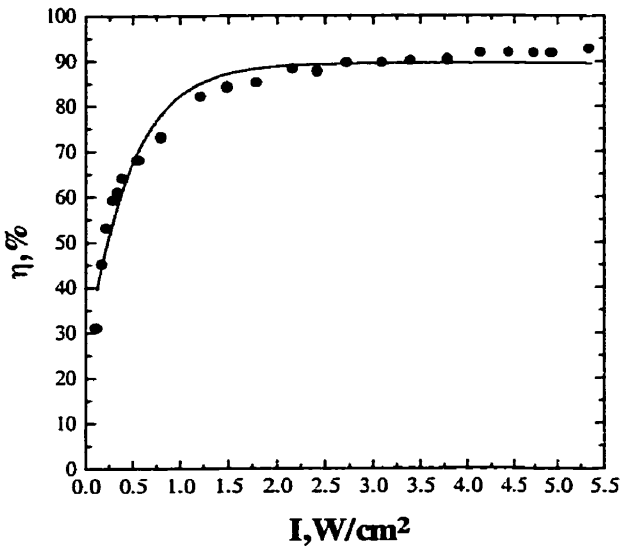

Figure 5.6 Steady state diffraction efficiency as a function of pump intensity for highest value of the total gain $\Gamma_{23}L=3$.

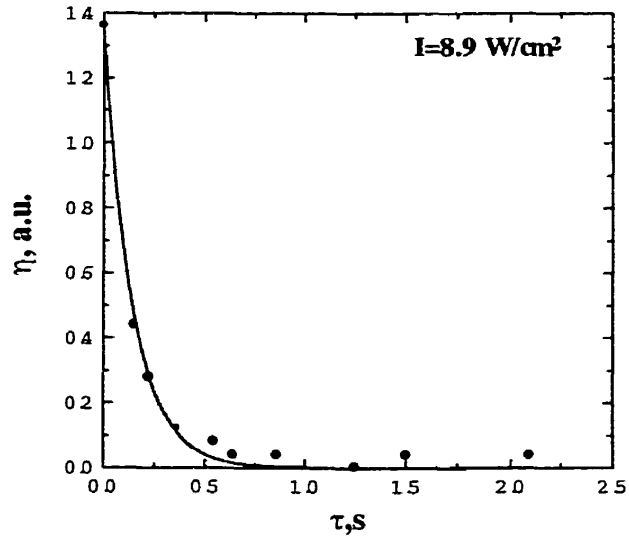

Figure 5.7 Residual grating diffraction efficiency as a function of temporal interval for which we blocked both writing beams.

Fig.5.6 demonstrates the diffraction efficiency η of the grating which results from self-seeded SDS of the smooth pump beam (at no external signal wave) into the wide-angular backward fanning. It was obtained at sample illumination only by x-polarized pump beam with a diameter about 0.7 mm. The initial sample transmission T_0 was compared to the transmission T_f after the backward fanning stabilization. The efficiency was calculated as $\eta=(T_0 - T_f)/T_0$. This result convincingly demonstrates that practically all the pump power, about 90%, at $I_L \geq 1$ W/cm^2 is back reflected demonstrating very high overall efficiency of SDS process.

5.4 Dark decay of gratings

5.4.1 Dynamics of dark decay

In these experiments we blocked both writing beams for some temporal interval Δt (after rather long illumination when some weak photorefractive grating had been stabilized). At the moment of switching light back we measured the diffraction efficiency η of a residual grating. Fig.5.7 (a) demonstrates a typical dependence of the residual grating efficiency versus

Δt at constant writing intensity. This graph was obtained for the reflection grating recorded by y-polarized beams. The pum intensity was I_L=8.9 W/cm^2 and $I_s << I_L$. We can emphasize following points: 1) dark decay exists; 2) it is very effective resulting in the complete washing out the grating; 3) it is very fast.

5.4.2 Decay rate intensity dependence and shallow traps

Fig.5.8 presents the measurements of the dark decay time τ_d on the pump intensity. The corresponding points were obtained from a set of graphs of $\eta(\Delta t)$ at different writing intensities I_L for reflection gratings. These points were obtained at 0.5 level of residual diffraction efficiency with respect to the initial one, i.e. $\eta(\tau_d)=0.5\eta(\Delta t \rightarrow 0)$. The reflection gratings were recorded by y-polarized beams.

The dependence of the dark decay rate on the recording intensity is typical for the crystals which have shallow traps [95, 96, 108] in addition to conventional deep traps. A final depth of dark decay depends only on the initial population of shallow traps since for conventional samples at thermal equilibrium the dark conductivity is negligible. Beside that the contribution to conductivity of the transient shallow-traps depends on the initial population of these traps, i.e. on the population during illumination. It is evident that the initial population of shallow traps strongly depends on recording intensity and it explains intensity dependencies of the rate and the depth of the dark decay.

We conclude that just shallow traps are the key trapping centers that are utilized for space-charge gratings recording in Fe:$KNbO_3$ and a relative role of the deep traps is rather low. It is the only explanation that we see to explain the high own dark conductivity: shallow traps can be easily thermoionized providing conductivity at dark conditions. Relatively slow intensity dependence of the dark decay rate on intensity indicates that at $I \geq 3$ W/cm^2 the transition of carriers from these shallow traps to a conductive band is almost saturated. This suggestion is in agreement with decrease of sensitivity ξ, see Fig.5.4, at the high intensities.

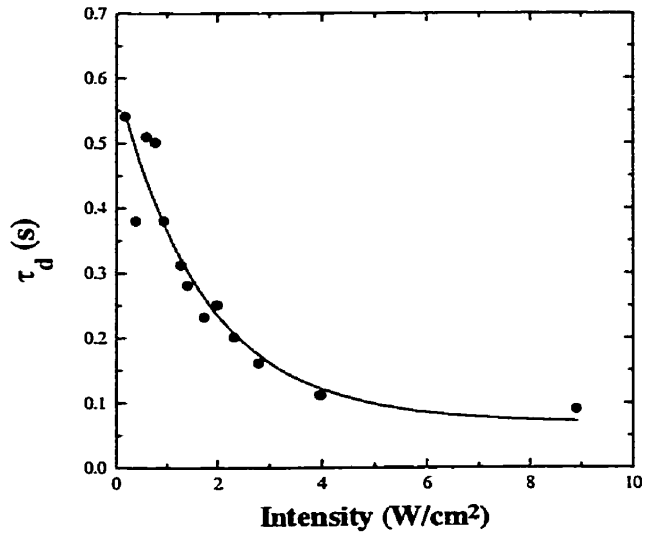

Figure 5.8 Dark decay time as a function of pump intensity for reflection gratings.

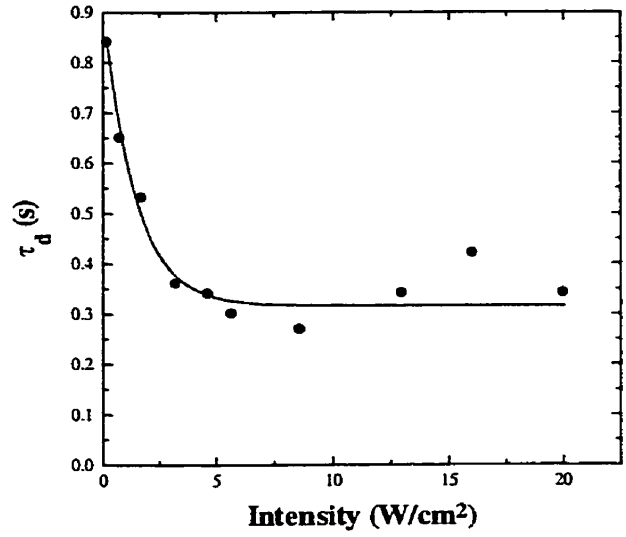

Figure 5.9 Dark decay time as a function of pump intensity for transmission grating.

5.4.3 Dark decay for transmission geometry

We performed similar measurements of the decay rate dependence on writing intensity for transmission gratings to make a comparison of transmission and reflection gratings rates (see Fig. 5.9). For any writing intensity the depth of decay was again the same: complete decay at rather high delay time Δt. The corresponding results for τ_d defined again via 0.5 level from the graph of initial grating efficiency versus writing intensity. The angle between recording beams $\theta=14^0$ (in air). As we can see the decay rate saturates at $I_L \approx 3$ W/cm^2 as for the reflection grating case. However this saturated rate at the same level of crystal photoconductivity is three times smaller than for the reflection gratings. The difference between the transmission and reflection geometries lies in a value of the Debye factor ν only [16]. For transmission gratings, $r_D q << 1$, this factor is equal to one while for reflection gratings $\nu = \left[1+(2kr_D)^2\right]^{-1}$ it can be lower.

The experimental ratio of decay time has, hence, give a value of the Debye factor as an independent method. Our result $\nu \approx 0.3$ is in agreement with the value for ν obtained at gain measurements in the section 4. This confirms the accuracy of our results for r_D and N_A density obtained above.

5.5 Conclusion

In this chapter material parameters of heavily iron doped $KNbO_3$ photorefractive crystal are experimentally studied. We observed that the most effective geometry of stimulated diffusion backscattering corresponds to pump propagation along $\vec{C}$ - axis of the sample.

We studied the polarization dependence of SDS. There are two eigen polarization states which correspond to linear polarizations along x and y axis of the sample. Both pump and signal beams are able to couple between each other by grating recording the identical polarization components. Different polarization components cannot interact via mutual grating but can serve as incoherent background illumination that decrease the gain for the orthogonal

pair. A polarization method of SDS gain measurements in the conditions of high pump-depleting total gain was proposed and used. SDS gain for x and y polarization components have been measured and amounted in our $KNbO_3$ sample to $\Gamma_x \approx 16.5$ cm^{-1} and $\Gamma_y \approx 5$ cm^{-1}.

We demonstrated that the relative seed of backward fanning is very high in our sample resulting in the pump depletion at the total gain $\Gamma_x L \approx 10$. The steady state efficiency of the reflection fanning grating at pump depletion can exceed 90%.

Using different independent techniques both Debye radius for our geometry, $r_D = 5.5.10^{-6}$ cm, and effective trapping centers density, $N_A \approx 10^{16}$ cm^{-3}, were obtained.

Both the saturation type for gain and sublinear growth for response rate intensity dependencies were demonstrated. The effective dark irradiance corresponds to about 2 W/cm^2. The photorefractive response rate 10 s^{-1} at 1 W/cm^2 intensity was demonstrated. Dark decay of the photorefractive gratings results, at any recording intensities, in complete washing out the gratings during less than 1 second. We concluded that just shallow trapping centers are responsible for space-charge gratings formation in Fe:$KNbO_3$.

CHAPTER 6

STIMULATED DIFFUSION BACKSCATTERING ABILITIES FOR PHASE CONJUGATION

In this chapter, we demonstrated that among many known phase conjugate schemes, stimulated diffusion backscattering (SDS) geometry has minimal sensitivity i.e. minimal energy required to switch on the phase conjugation (PC) reflection. This makes the SDS effect one of the important geometry for practical applications.

Both self-phase-conjugation (self-PC) and double-phase conjugation is considered possibly as the most interesting applications of stimulated diffusion backscattering (SDS) effect. We present in this chapter a clarification regarding the conditions to attain self-PC in steady-state SDS. The high quality double-PC at double-loop reflection geometry is also demonstrated. We also compared technical characteristics of different PC-mirrors based on reflection gratings.

6.1 Optical phase conjugation

6.1.1 Phase conjugation

The concept of phase conjugate of light was for the first time precisely described by Zel'dovich and his colleagues in the early seventieth [9]. They discovered an interesting phenomenon that occurred in their work with stimulated Brillouin scattering (SBS) in a CS_2 filled waveguide. They placed a beam distorting element in front of the CS_2 waveguide and observed that after returning back through the distorting element, the backscattering light had the same undistorted spatial beam profile as the original beam. The CS_2 filled waveguide was a phase conjugation mirror. Optical phase conjugate mirror reverses both the direction of propagation and the phase factor for each plane wave component of an arbitrary incoming beam of light. This means that a phase conjugator can be considered as a kind of mirror with very unusual reflection properties. Unlike a conventional mirror, where a ray is redirected according to the ordinary law of reflection, a phase-conjugate mirror (PCM) retroreflects all incoming rays back to their origin (see Fig.6.1). Thus, any optical beam that is reflected by a PCM will retrace its original path [8]. In order to understand the properties of conjugate fields we consider an optical wave of frequency ω propagating in the +z direction

$$E_1(\vec{r},t) = |E(\vec{r})|\cos[\omega t - kz - \varphi(\vec{r})] = \mathrm{Re}\left\{E(\vec{r})e^{i(\omega t - kz)}\right\} \tag{6.1}$$

where $E(\vec{r})$ is a complex amplitude containing the phase information $\varphi(\vec{r})$.

(a) (b)

Figure 6.1 Reflection of a plane wave from (a) an ordinary mirror and (b) a phase conjugate mirror.

The time-reversed wave $E_2(\vec{r},t) \equiv E_1(\vec{r},-t)$ is then given by

$$E_2(\vec{r},t) = |E(\vec{r})|\cos[-\omega t - kz - \varphi(\vec{r})] \equiv$$
$$|E(\vec{r})|\cos[\omega t + kz + \varphi(\vec{r})] = \mathrm{Re}\left\{ E^*(\vec{r})e^{i(\omega t+kz)} \right\} \tag{6.2}$$

where $E^*(\vec{r})$ is the complex conjugate of the complex amplitude $E(\vec{r})$. This conjugate wave corresponds to a wave moving in the –z direction, with the phase $\varphi(\vec{r})$ reversed relative to the incident wave. Phase conjugation can thus be regarded as a type of reflection combined with phase reversal. It is equivalent to leaving the spatial part of E unchanged and reversing the sign of t i.e. phase conjugation is equivalent to time reversal.

Degenerate four-wave mixing (DFWM) is one of the most important process used for phase conjugation [8-10, 79, 80]. It is a third-order nonlinear optical process involving the mixing of four separate optical waves, all with the same frequency ω. The three input waves consist of two antiparallel, high-power pump or reference waves and a weaker probe wave. The output of the mixing process can be interpreted in terms of induced gratings and diffraction. Furthermore, there is a close analogy between phase conjugation by DFWM and holography [8, 10]. Two of the three input waves interfere and form either a spatially or temporally modulated grating; the third input wave is scattered by the grating to yield the output wave. In conventional holography the spatial gratings are recorded in a photographic emulsion, and for DFWM they are formed by the induced nonlinear refractive index change, proportional to the local light intensity. The induced temporal gratings, at frequency 2ω, in DFWM have no analogy in holography. In terms of photons DFWM can be described as a parametric process where the energy from two pump photons, one from each wave, is converted into one probe and one output signal photon. The energy conservation requirement is obviously fulfilled in this case since all photons have the same frequency. To have an efficient energy transfer from the pumps to the probe and signal we must also have momentum conservation. With $\vec{k}_1, \vec{k}_2, \vec{k}_p, \vec{k}_s$ as the wave vectors of the two pumps, the probe, and the signal wave, respectively, this so called phase-matching condition states that $\vec{k}_1 + \vec{k}_2 = \vec{k}_p + \vec{k}_s$. Since the two pump photons are antiparallel, with zero total momentum

$(\bar{k}_1 + \bar{k}_2 = 0)$, this means that the signal wave must be antiparallel to the probe wave, $\bar{k}_p + \bar{k}_s = 0$. Momentum conservation is the basis of the phase-conjugate nature of the output signal in DFWM. A coupled wave analysis of the problem confirms that the signal is proportional to the complex conjugate of the probe field [8-10, 79, 80].

The remarkable reflection property of the PCM has found many important applications [8, 10]. These include effects as diverse as parametric oscillation, optical tracking and pointing, spatial and temporal image processing, optical computing, optical filtering, etc.[90, 10, 17].

6.1.2 Phase Conjugation by means of stimulated diffusion backscattering (SDS) and stimulated Brillouin scattering (SBS)

Both SDS and SBS processes excite the interest mostly due to their ability to perform self phase conjugation (PC) of the pump beam without any extra reference beams. However physical pictures of processes for SDS and SBS are different. A common feature of SBS and SDS is that the phase conjugate reflectivity appears due to a difference of stimulated scattering (SS) gains for different spatial configurations of backscattered radiation. Many different spatial configurations can be excited by random spontaneous seed and suffer stimulated scattering (SS) amplification. A phase conjugated beam, to the pump beam spatial profile, accidentally appears among seeding waves. This phase conjugate beam must be amplified much stronger than a large number of all alternative configurations uncorrelated to the pump.

For SBS, as it is well-known [8], the reason of preferential gain of PC configuration is connected to the proportionality of the local SS-gain $\Gamma = GI_L(\vec{R})$ to the local intensity $I_L(\vec{R})$ of the pump beam. For typical SS experiments with PC the spatial pattern of the pump intensity $I_L(\vec{R})$ is chosen strongly inhomogeneous over the interaction volume due to either strong focusing or deliberate "speckling" of the pump. PC configuration locates its maxima of the intensity spatial pattern at the maxima of the spatially inhomogeneous local gain pattern. At the same time the patterns of the uncorrelated configurations and the gain profile are not

correlated in space and their maximum and minimum are located arbitrarily with respect to each other. This spatial resonance of the PC component with the gain pattern results, in particular, for the speckled pump in the two-times excess of the PC configuration gain over the uncorrelated scattered waves [8].

For SDS, as it was mentioned above, the steady-state gain Γ is intensity independent. Hence there is no spatial resonance of the gain pattern with a pattern of any amplified configuration: the gain in the steady-state is spatially uniform even if the pump wave pattern is spatially inhomogeneous. It means that there should be a separate mechanism to attain PC at a steady-state regime of the stimulated diffusion backscattering. At the same time a transient regime of SDS is preferable from the viewpoint of phase conjugation [83, 86-88, 92-94]. The reason lies in the mentioned above proportionality of the local grating response rate $\tau_{di}^{-1}(\vec{R}) \propto I_L(\vec{R})$ to the pump intensity $I_L(\vec{R})$. As the result, the PC configuration obtains a privilege to build-up the grating configuration, which reflects pump just into this PC wave, faster than any other uncorrelated configuration can create its own grating. This type of the discrimination mechanism had been proposed in refs [83, 86]. Transient SDS of spatially coherent pump was studied in ref's [91, 94, 104]. The spatially incoherent, "boiling" pump pattern in a quasi-steady-state, was also studied in [87, 88]. It was shown that the relative excess of PC-mode gain is not high for this transient discrimination mechanism, no more than 1,3 [87, 88].

It was demonstrated experimentally [84] that some additional and uniform in space component of the conductivity can provide positive correlation of the steady-state SDS gain with the pump intensity: $\Gamma(I_L) = \Gamma_0 \frac{I_L / I_d}{1 + I_L / I_d}$. This positive correlation is rather high if this additional conductivity is comparable in average with the pump induced photoconductivity, i.e. if $I_L \sim I_d$. The uniform conductivity can be originated either from high concentration of impurities of the sample [84] or from deliberate additional uniform illumination of the interaction volume. In the latter case I_d is just this illumination intensity, in the former case it is some effective parameter. Such a positive correlation can be evidently responsible for the

preferential steady-state amplification of the PC-mode, and it was successfully demonstrated in [84].

However the first experimental demonstration of self-PC in SDS [82] as well as some other observations [90, 105] indicate that the reflection gratings can play some role in the self-conjugation process even in a steady-state and if $I_d << I_L$. Actual role of these grating is still to discuss.

6. 2 Scan of the pump beam

First, we study stimulated diffusion backscattering in the conditions of a single transverse mode smooth pump beam focused into the crystal $KnbO_3$: Fe (0.5 wt.%) (see chapter 5). We observed the following. If focusing is not strong so that the focal neck $l_f \approx \left[k(D/F)^2\right]^{-1}$ of the beam is much longer than the sample thickness L=0.6 cm, i.e. at $l_f >>$ L, then the reflected wave is simply a wide angular speckled fanning which is much more divergent than the pump beam. The particular output divergence $\Delta\theta_s$ depends on a relative location of the neck itself with respect to a sample and is minimal if it is centered inside or near the sample. In general case, Fig.6.2.a, $\Delta\theta_s$ can be estimated as d/L where d is a diameter of the illuminated area.

If the pump beam convergence D/F after a lens is chosen to create the neck of a length $l_f \approx$L, then the minimal divergence $\Delta\theta_s$ of the reflected wave decreases up to the angle which is very close to the angle D/F, i.e. close to the diffraction limited one, $\Delta\theta_s \geq \Delta\theta_{diff}$, Fig.6.2.b. Of course it is true when the pump beam is the diffraction quality itself. So one can talk about phase conjugation if the neck is located inside the sample, i.e. when $d = d_0 = \sqrt{L/k}$, so that the aperture angle of the illuminated volume d/L correspond

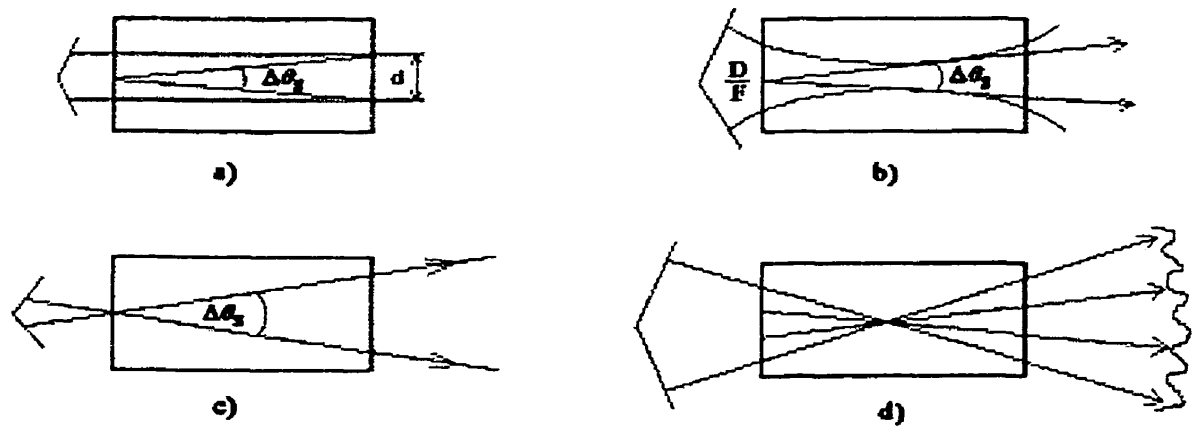

Figure 6.2 A single transverse mode pump beam focused into the crystal. The particular output divergence $\Delta\theta s$ depends on a relative location of the neck with respect to a sample.

to the diffraction limited angle $\Delta\theta_{diff}\sim(kd_o)^{-1}$ at the diameter d of the focal neck, $\Delta\theta_s=d_o/L\approx\lambda/2\pi d_o$. Otherwise the output divergence is again much higher then the diffraction limited $\Delta\theta_{diff}\approx\lambda/d$.

If focusing is very sharp the divergence $\Delta\theta_s$ which could be close to the diffraction quality limit can be also obtained but only if one precisely adjusted the neck near the output surface, Fig.6.2.c. This neck in this case serves as a "point source" seed, which is amplified within the illuminated cone. At other locations of the neck many alternative rays which do not cross this neck can effectively amplified by the illuminated cone-type volume which provides in the steady-state the uniform gain at each illuminated point; the output radiation is again speckled one, Fig.6.2.d.

The experimental verifications of the optimal condition for phase conjugation is presented later. We would like to pay reader's attention to the following estimate. The conditions when PC-type output is available, as it was shown above, are $d\leq\sqrt{\lambda L}$. The parameter $\sqrt{\lambda L}=d_{max}\leq 0.05mm$ for all samples and wavelengths used in photorefractive experiments. It means that at the pump power, which is typically $P_L\approx 0.1$ W, the power density

in the neck exceeds $I_L \geq 10^4$ W/cm^2. According to our measurements of the response rate τ_{di}^{-1} which has been performed in the range $I_L \leq 10$ W/cm^2 and also to the standard extrapolation of this rate into the range of higher intensities using the approximate expression $\tau_{di}^{-1} \approx \xi I_L$ one can estimate the dielectric relaxation time in the neck as the extremely short value: $\tau_{di} \leq 0.1$ms. Even if we take into account the slowing-down factor $\tau_{SDS} \approx \tau_{di}/(\Gamma L/2)$ [85, 104] the final estimates of the SDS build-up time would give us $\tau_{SDS} \leq 0.5$ ms.

Such an extremely fast response rate at rather moderate pump power revealed in our experimental test as rather interesting effect. At rather strong focusing when the neck embedded into the sample we always observed very effective stimulated backscattering. If one moves the sample in any direction the nonlinear reflection remained as effective as at the motionless sample. And it was the case at any motion velocity we were able to apply by hands, $V \geq 1$ cm/s.

We did not study this effect quantitatively and performed qualitative demonstrations only because it was accompanied by very strong fluctuations of fidelity and, at a bit lower level, reflectivity. We defined fidelity as $H=R_0/R$, where R is the total nonlinear reflection coefficient of a crystal, and R_0 is the coefficient of reflection into the phase conjugate component. The problem is that these fluctuations were induced, in our opinion, by poor quality of our sample surface polishing. The surface induced distortions of the wavefront are severe enough to disturb significantly the pump beam pattern in the neck and these disturbance realizations strongly varied at crystal motion resulting in the fluctuation of the reflected beam. Unfortunately we were not ably to improve crystal quality in our conditions and did not found it feasible to monitor poor surface parameters instead of properties of SDS itself. We believe that for a sample of proper quality the fluctuations in such the experiment will take place at very sharp focusing only, $l_f \ll L$, and will be connected to the adjustment of the neck into the output surface, Fig.6.2.c,d, being resulted from longitudinal motions of the sample only.

The above discussion about focusing conditions to attain phase conjugation at SDS of the single-transverse-mode pump beam is applicable qualitatively to the steady state

conditions. The improvement we have to apply especially for the steady-state concerns a manner to define an actual shape of the effective active waveguide [8] which is formed in the sample by the pump beam inside the illuminated area.

For SBS case such a waveguide is a nonuniform gain profile since the SS gain is proportional to the pump intensity. The effective width of the SBS waveguide at each cross-section can be defined as a width of the pump beam itself [8] using a criterion of e^{-1} intensity at the axis.

For the steady-state SDS the situation is very different. First of all it is very difficult to define correctly the steady-state conditions because the response time $\tau_{di}(\vec{R}) \propto I_L^{-1}(\vec{R})$ at the far wings of the beam, were $I_L \to 0$, is formally infinite. But if the dark conductivity is taken into account the response time is nevertheless finite even at the wings: $\tau_{di}^{max} \approx (\xi I_d)^{-1}$ which corresponds, in our case, to $\tau_{di} \approx 0.2$ s (see Fig.5.3). Second, the gain intensity dependence can be reduced for SDS to $\Gamma(I_L) = \Gamma_0 (I_L / I_d)/[1 + (I_L / I_d)]$, (see Fig.5.4). It means that actual boundary of the active waveguide for the signal beam is defined by the condition $I_L(\vec{R}) \approx I_d$. For the pump Gaussian beam of a radius *a* and of an axial intensity I_0, i.e. for the illumination profile $I_L(\vec{r}) = I_0 \exp(-r^2 / a^2)$, the effective radius of the waveguide is

$$r_{eff} = a\sqrt{\ln I_0 / I_d} \tag{6.3}$$

and it is about $\sqrt{\ln I_0 / I_d}$ times wider than the one for SBS case. For Gaussian beam this factor is not large. But in the PC conditions demonstrated above, where $I_0 \approx 10^4$ W/cm^2 and $I_d \approx 2$ W/cm^2, this factor is equal to about 3. Thus, for SDS the effective active waveguide near the focal neck turns out to be noticeably wider than the pump beam itself. This broadening diminishes (by the way, up to zero) at a rather far distance from this neck. And finally all the illuminated area inside such boundaries for SDS has, due to the same $\Gamma(I_L)$ dependence, the constant gain $\Gamma(\vec{R}) = \Gamma_0 = \Gamma(I_L >> I_d)$.

We made the following experiment: a radiation from an cw Ar-ion laser (λ=0.488 μm) was focused in the crystal $KNbO_3$:Fe (0.5 wt%) (see chapters 4&5). Expanded to diameter D≈5 mm pump beam was focused by the lens of focal distance F = 11 cm into the crystal, so that the beam focal neck was inside the crystal i.e. $l_f \approx L$. Then the reflected beam is strongly aberrated comparing to the input pump beam. The particular realization of this aberrating pattern was accidental and depended on a particular place in the crystal where the pump was focused. The output PC fidelity $H=R_0/R$, defined above, fluctuated from focusing. However, these fluctuations were not very high at $l_f \approx L$ and the output beam parameters demonstrated reasonable stability being very good in average. The overall reflectivity R measured was always higher than 50% and the same for the fidelity $H \geq 70\%$, which had been measured as a portion of the reflected beam penetrating into an aperture of angular diameter $\Delta\theta_0 = 4.10^{-4}$ rad.

If we used sharp focusing of the pump at D/F≈0.1 and $d_{min} \approx 20$ μm, $l_f \approx 0.5$ mm, then the final result strongly depended in this case on a location of the focal neck: focusing inside the crystal, very accurately near the back facet of the crystal or focusing far behind the back facet of the crystal. PC regime is available, but only at precise adjustment of the scheme. Fig. 6.3 illustrates the accuracy required: the brightness of the central bright spot in the far field versus longitudinal detuning of the neck is plotted; the maximum corresponds to focusing at the back facet. Such a high accuracy is evidently responsible for high fluctuations of fidelity at longitudinal shifts of the sample. The measurements demonstrated that, at least for the optimal conditions, the overall SDS reflectivity from the crystal was also very high, $R \geq 50\%$, and relatively stable with respect to changing a place of focusing. The fidelity at these optimal conditions has almost maximum value.

6. 3 Measurements of SDS-PC sensitivity for unaberrated focused pump

The actual steady-state SDS-PC at pump focusing is reached at τ–0.2 s (see above) which corresponds to process stabilization in the whole area where external illumination

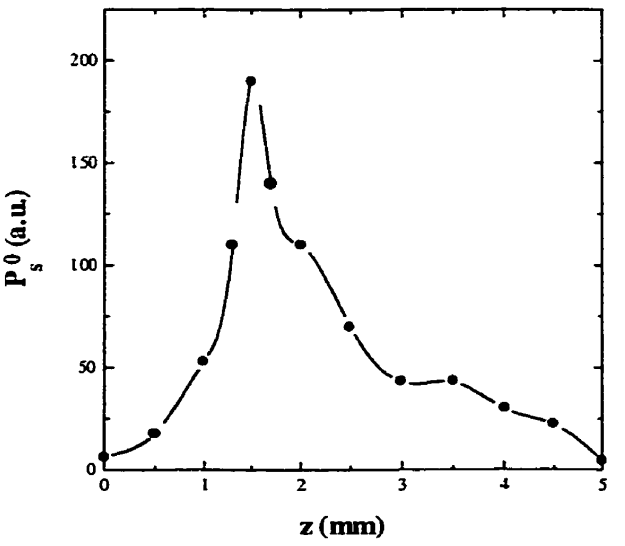

Figure 6.3 Brightness of the central bright spot in the far field versus longitudinal detuning of the neck.

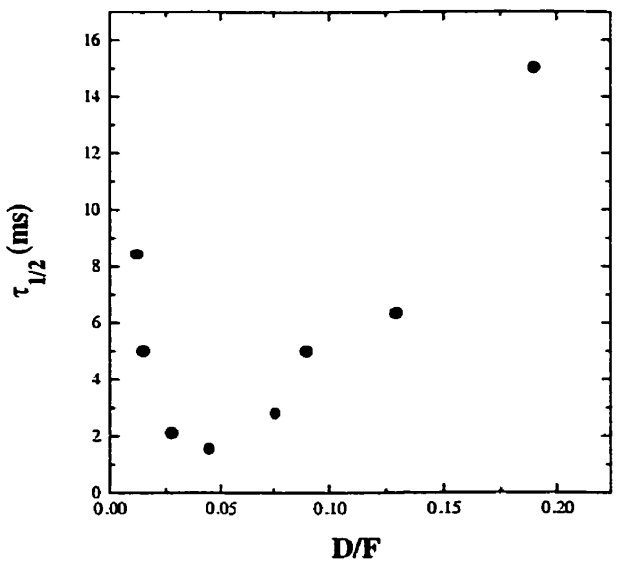

Figure 6.4 Backward SDS build-up time τ, which had been measured at a level of 0.5 of the steady-state reflectivity R, for unaberrated pump focused inside the sample at different convergence angles.

exceeds the dark I_d one. The obvious idea to increase the SDS response rate consists in sharp focusing of the pump beam inside the sample.

The experimental points in Fig.6.4 demonstrate the backward SDS build-up time τ for unaberrated pump focused inside the sample $KNbO_3$: Fe at different convergence angles. The build-up time values were measured at a level of 0.5 of the steady-state reflectivity R using a radiation from an cw Ar-ion laser (λ=0.488 μm). The angles were varied by changing expanded beam diameter D at the focusing lens of F= 11 cm. The input power of the pump P_L was fixed for all these points at rather low level P_L=6 mW. All points were obtained at optimal position of focal neck which at $l_f \leq L$ provided PC. This figure shows that the condition of optimal focusing exist and variations in both sides result in a drop of SDS sensitivity (which can be defined as $W_{thr}=P_L\tau_{1/2}$). The optimal condition corresponds to the case $l_f \approx [k(D/F)^2]^{-1} \sim L$ and, in our case, is attained at D/F≈0.04. Our best sensitivity obtained is $W_{thr}=10^{-2}$ mJ. The physical origin of the optimum in Fig.6.4 is rather obvious. A decrease in the focusing strength, $l_f >> L$, leads to a drop of the axial intensity in the sample. Sharper focusing at $l_f << L$ would enhance a response rate due to the increase of the intensity inside the neck. However, it is not the case. The reason of the overall decrease of the response rate is connected here to very sharp nonuniformity of the axial intensity along the pump trace inside the sample. Very high intensity is available in the neck only for a small part of the whole interaction length. At a residual part of the sample the intensity is oppositely very low just due to sharp convergence of the pump. As a result, at very strong focusing of the pump at fixed total power, one has the local acceleration of the grating build-up process only in the short focal neck but the slowing process outside the neck. The overall dynamics turn out to be rather complicated at sharp focusing. The grating was stabilized fast at small area and than it slowly spread to the less illuminated area, approaching necessary threshold interaction length.

From the practical point of view, for corrections of aberrations, the phase conjugation of the strongly aberrated or even speckled pump is the most desirable point. The complex amplitude of the speckle field at every given point is composed of a large number of small independent contributions, namely the waves reflected (or transmitted) by different points of the object. The backward conductivity mechanism for speckled pump was verified

experimentally in the work [93] in very "dirty" $BaTiO_3$ sample. We tried to verify it as well in application to our $KNbO_3$ sample. Phase conjugation was reached by a careful choice both of the input power (to provide $\langle I_L \rangle \sim I_d$ in the neck) and of particular realization of the place at the distorting phase plate.

The maximal value of fidelity in this scheme was very low $H_{max} \approx 15$ %. But the most pity point was that a reproducibility of PC effect was extremely low and it was related to accidental "lucky" illuminated area of both the aberrator and crystal. We did not study this effect in more details because it will be hard to find any application, at least for our sample of moderate total gain $\Gamma L \approx 10$.

6. 4 Effect of dark conductivity

At pump depletion, i.e. in the conditions when $I_S(L) \approx I_L(L)$, the intensities of both beams are very close at the most part of the interaction length (because the difference between both these intensities is a constant of interaction and does not change along z, see below). It means that the interference pattern contrast $|m| = \dfrac{2|E_L E_S|}{|E_L|^2 + |E_S|^2}$ can be very close to unity everywhere inside a sample. As it is well-known [16] for such conditions the grating fringe shape is not sinusoidal and one has to utilize the first spatial harmonic only, see Eq.(4.17). If the dark conductivity in negligible, $I_d=0$, the amplitude E_1 of this first spatial harmonic of the space-charge field grating is [1]

$$E_1 = E_D \frac{1-\sqrt{1-m^2}}{m} \nu \qquad (6.4)$$

instead of $(1/2)mE_D\nu$ as it is usually taken at small m. For plane interacting waves the resulting equations of interaction are presented and discussed in chapter 4, see Eqs.(4.19).

The idea that we would like to propose and to defend, is based on already mentioned and well known fact that at m≈1 an effective coupling efficiency is actually higher than in the case where E_1 is taken as $(1/2)mE_D v$ even at high contrast and where the Eqs.(4.18) is taken as the basic one. For plane interacting waves at $I_S \leq I_L$ the signal wave is amplified at maximal possible gain: $E_S(z)= E_S(0)\exp(\Gamma z/2)$, see Eqs.(4.19). While the approximate model (4.18) gives nonexponential amplification with a differential gain $\Gamma I_L/(I_L+I_S)$ that is always less than Γ. The "high contrast induced" enhancement of local differential gain is especially high at $I_S \approx I_L$, i.e. at deep depletion, and corresponds up to two times difference in the actual and approximate gain.

One has to mention that the effect described should be especially high just for the reflection gratings geometry comparing to the transmission gratings. The reason is that for reflection gratings an integral of interaction is $I_L(z)- I_S(z)$=const. Then at $R=I_S(L)/ I_L(L) \approx 1$ we have $I_L(z) \approx I_S(z)$ almost along all the interaction length L: both intensities drop simultaneously together along (-z) direction. For the copropagating case a sum of intensities is an integral of interaction [16], $I_L(z)+ I_S(z)$=const. In this case an efficient coupling results evidently in considerable change of the beams intensity ratio $I_S(z)/ I_L(z)$ along z axis. Only relatively small portion Δz of the interaction length L corresponds to close intensities $I_S \sim I_L$ where high-contrast coupling enhancement emphasize the differential gain.

We demonstrated in chapter 5 that dark conductivity is extremely high in our samples I_d=2 W/cm^2 [15, ch.5] and we will estimate its effect on the efficiency of PC discrimination. The depletion induced discrimination mechanism is based on the grating first harmonic amplitude enhancement in the conditions of high interference pattern contrast m ≈1. The grating fringe profile, which at I_d=0, gives the enhancement factor ρ [16]:

$$\rho = \left(\frac{1-\sqrt{1-m^2}}{m} \right) \Big/ (m/2) \qquad (6.5)$$

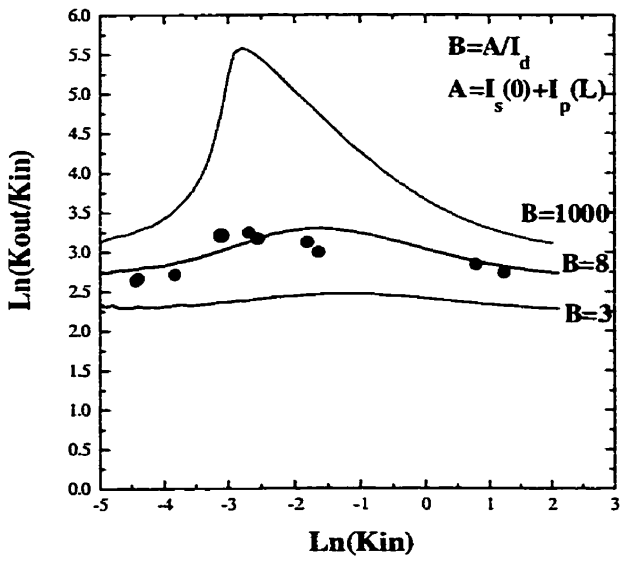

Figure 6.5 Both theoretical and experimental dependencies of the effective total gain ΓL for pump depletion regime versus the natural log of the input intensity ratio.

At m→1 one has ρ→2. When I_d is not zero, the conductivity spatial pattern contrast m_σ, which is actually responsible for grating formation, turns out to be lower than the light pattern contrast. Then, at m→1 the enhancement factor (6.5), which is controlled now by m_σ value instead of m, turns out to be lower:

$$\rho_{max} \approx 2\left[1-\sqrt{\frac{2I_d}{I_L+I_S}}\right] \tag{6.6}$$

that was obtained assuming $I_d/(I_L+I_S)$ as small parameter. The resulting dependence of the enhancement factor ρ_{max} on I_d turned out to be very sharp. Particularly, for $I_d/I_L \approx 0.1$, that corresponds in our case to $I_L \approx 20$ W/cm^2 or to focusing our pump into the small spot about 0.5mm in diameter, we have $\rho_{max} \approx 1$. It means that any enhancement discussed completely disappears and no noticeable discrimination is possible for our samples.

In Fig.6.5, both theoretical and experimental dependencies of the effective total gain ΓL for pump depletion regime versus input intensity ratio is drawn. The effective total gain had been found here according to the following definition:

$$\Gamma l_{eff} = \ln\left[\frac{(I_S(L)/I_L(0))}{(I_S(0)/I_L(L)}\right] \tag{6.7}$$

i.e. as the natural logarithm of the ratio of the output to input ratios of the interacting beams. The experimental points were obtained for y-polarized smooth beams coupling, i.e. at $\Gamma_y L=3$. The solid curves represent the theoretical results obtained by direct computer integration of the two-wave coupling equations (4.14)-(4.16) at different ratios B of photo- and dark conductivities. It is seen that at B≈8, that approximately corresponded to experimental conditions, the theory fits the experiment well enough.

The results in Fig.6.5 convincingly demonstrate that even at a very moderate level of relative dark conductivity, the effect of high contrast enhancement of coupling efficiency completely disappears, and unfortunately disappears together with PC discrimination effect for our samples. We has to provide $I_L/I_d \geq 10^2$ to attain noticeable discrimination effect.

6. 5 Comparison of Sensitivity for SDS and PC-Loop geometries

The self-seeded SDS may serve as a rather effective and fast PC-mirror for unaberrated pump beams. The unique benefit of this simple scheme of self-PC: it allows the wide angle of vision of this mirror, about a ratio of a sample size to a focal length L/F~0.1. Moreover, the sensitivity is about 10^{-5} J, which at the optimal focal neck diameter equal to about 50 μm and at the incident power equal to about 10 mW, corresponds to the mirror response rate equal to about 10^4 s^{-1}. This allows one to move the neck position within this angle of vision at a transverse speed about 50 cm/s. It corresponds, at F~10 cm, to a speed of

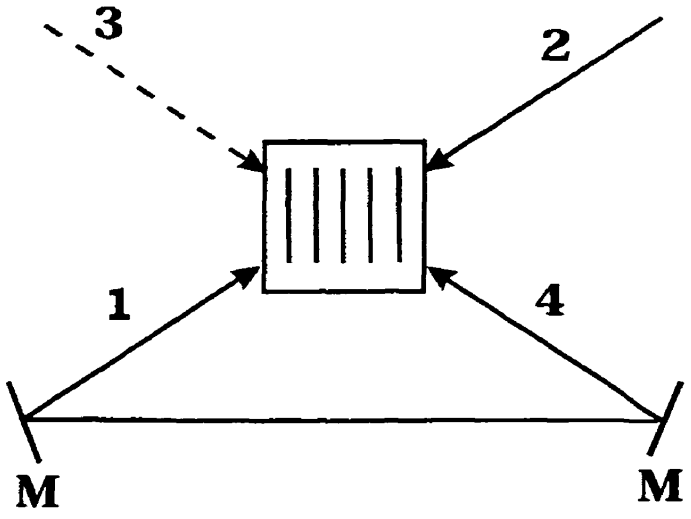

Figure 6.6 Geometry of the reflection-grating passive ring mirror.

angular variations of arriving pump direction about several radians per second. This figure also looks like the absolute record for a speed of optical tracking.

The alternative device that provides self-PC at reflection gratings is loop-type geometry [89, 98, 101]. In this geometry (see Fig.6.6) beam 2, to be conjugated after passing through a nonlinear medium, is returned to the medium (as beam 4) along an external optical feedback loop. Scattered beams 1 and 3 may be generated in this geometry as the result of an oscillation instability development. Beam 3 propagates opposite the pumping beam 4 and, after passing through the feedback loop, turns into beam 1, counter-propagating to the initial pumping beam 2.

Fig.6.7 represents the experimental curves for the temporal response of various configurations. All of them were obtained for the same pump beam of fixed diameter d=0.2mm and fixed cw power P_L= 80 mW. The curve (4) presents two-wave mixing (TWM) experiment (see Fig.5.1) at x-polarizations and at I_S~I_L; the curve (3) is the self-seeded SDS response (that gave no PC at such a large diameter d) and the curves (1) and (2) give the loop scheme PC-reflectivity versus time at different adjustments of beams overlapping inside the

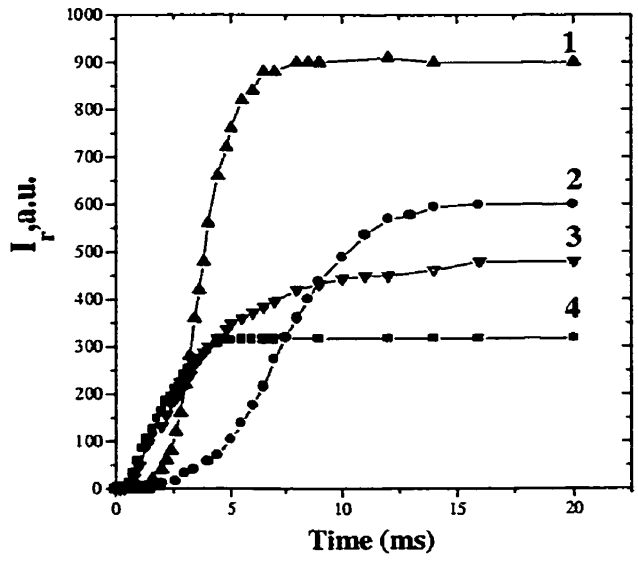

Figure 6.7 Experimental curves for the temporal responses of different configurations.

sample. The last two curves drawn using the same units for reflectivity, vertical scales for two others are arbitrary.

First, a difference in adjustments for (1) and (2) curves was accidental and it was within an available accuracy of adjustment. It demonstrates how vulnerable is this loop scheme at such small pump beam diameters with respect to loop adjustment and to input parameters of the incident pump. Second, typical temporal scales for all curves are comparable. Third, TWM is, as it was expected, the fastest process providing the growing-up rate close to τ_{di}^{-1}. The backward fanning wave was somewhat slower. The loop geometry was stabilized the last among all of them. Finally, careful adjustment of the loop makes its effective response rate very close to the ones of SDS backscattering and also results in much better reflectivity.

The fact that the loop scheme was the last in this "competition" is interesting. The typical response time τ for self-seeded SS process is estimated as $\tau \sim \tau_{di}(\Gamma L/2)$ [8] while a rate of overthreshold exponential growth for the loop is estimated as $\tau^{-1} \sim \tau_{di}^{-1} \frac{\Gamma L - (\Gamma L)_{thr}}{(\Gamma L)_{thr}}$

[98, 100] (which is a property of any absolute instability). Then the loop scheme is faster than self seeded SS process due to high (up to five times) excess over threshold at ΓL=10. However, if one accounts for linear losses in the loop, as well as not perfect adjustment, the value $(\Gamma L)_{thr}$ will amount to about 4 instead of theoretical limit of 2 [30], so that actually for this loop $\Delta \Gamma L / \Gamma l_{thr} \sim 1{,}5$ only. Another factor is that the initial seed ε for the loop, which corresponds to excitation of only one transverse mode, is much smaller than the one at wide-angular fanning excitation. As a result, a generated signal in the loop demonstrates a sharper temporal derivative (what is clearly seen for the curve 1 in Fig.6.9) but being poorly seed it grows to saturation level longer than the very reach SDS seed is doing it.

The best sensitivity value for reflecting gratings loop PC-mirror which was obtained in these particular measurements corresponds to 0.25 mJ. The lower sensitivity, comparing to the the value 0.01 mJ attained for self-seeded SDS, is due to the purely technical reason: we have to provide wide enough beams diameter for a reliable alignment of the loop optical elements. Particularly, for focusing strength used the SDS sensitivity is about 0.15 mJ which is ten times worse than the best value obtained. Nevertheless, both loop and SDS sensitivities, which are very close, were obtained for the same beam diameter. This observation definitely indicates that there exists a possibility to further improvement of the loop sensitivity if the problem of reliable loop adjustment would be solved for the beam diameter $d \leq 100$ μm.

6.6 Double-Loop Reflection Gratings DPCM

In self-pumped phase conjugators, a single incident laser beam is responsible for the oscillation and the subsequent generation of the phase conjugate wave. However there is another class of phase conjugators in which two incident laser beams mutually pump the photorefractive crystal. The last object of our experimental study is the double loop geometry shown at Fig.6.8. This scheme provides phase conjugation of radiation of two mutually incoherent laser beams [109-114]. This geometry is as follows : two mutually incoherent beams are incident upon two nonlinear mediums. After passing through the nonlinear medium, each of the beams, with the help of external mirrors, is directed to another medium,

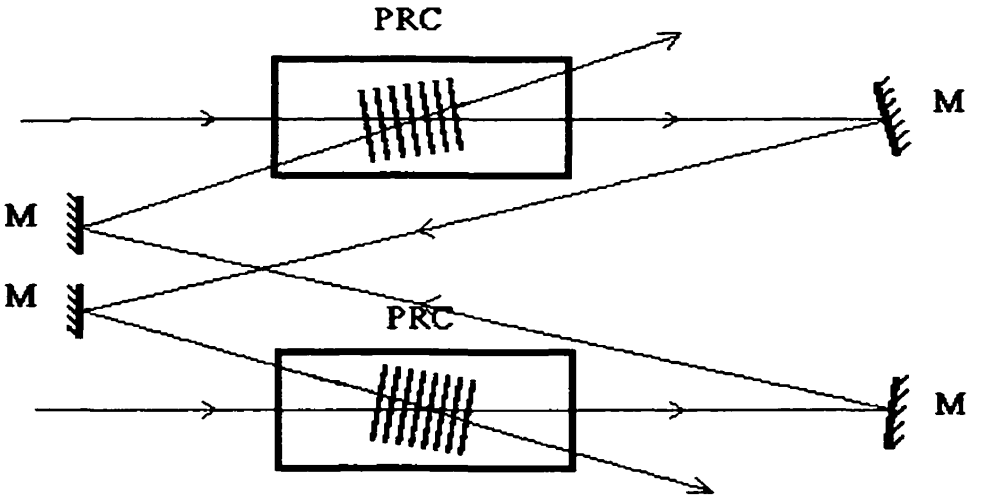

Figure 6.8 Double loop geometry using photorefractive crystals (PRC)

where it intersects the second beam. Scattered radiation arises in this geometry as the result of an oscillation regime (temporal instability) development and travels opposite the primary incident beams. The scattered light (fanned light) from one beam can Bragg diffract off the scattered (fanning) gratings formed by the other beam. The gratings generated from one incident beam will reinforce the gratingsproduced by the second incident beam only if the light diffracted from the first incident beam's grating is the phase conjugate of the diffracted light from the second beam [109-114]. All overlapping photorefractive SDS gratings produced independently by the two incident beams will out unless they are written by mutually phase-conjugated beams.

In each of the beam overlap regions the interacting waves wave-vector configuration allows the existence of four nonlinear refraction index gratings. When the coherence times of the pump beams are much smaller than the nonlinear characteristic relaxation time, only the grating that is written by the coherence pairs of pumping and scattered beams is effectively excited. The readout of this grating by the pumping beams closes the feedback loops, resulting in the scattered radiation generation.

Here we report the results of more detailed measurements performed to monitor reflectivity in both channels as well as a response rate as functions of input power ratio of the

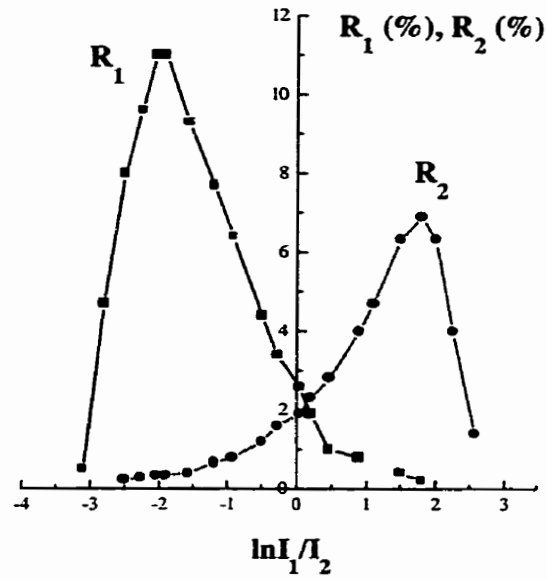

(a)

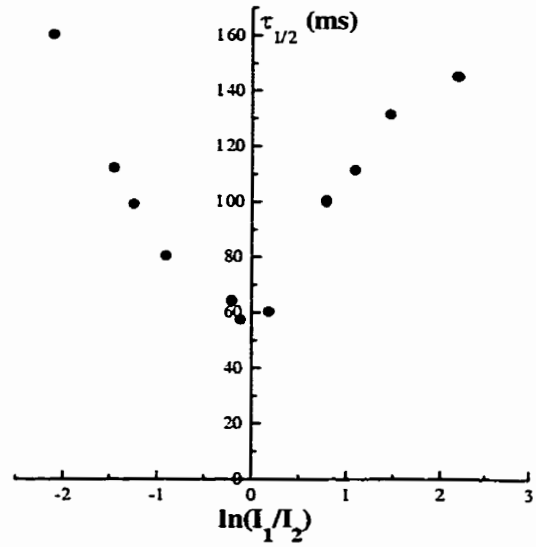

(b)

Figure 6.9 (a) steady-state reflectivity for double loop geometry (b) build-up time (which was defined at a level of 0.5 of a steady-state reflectivity).

pumping beams. The corresponding points are plotted at the Fig.6.9.a for the steady-state reflectivity and at the Fig.6.9.b for a build-up time (which was defined at a level of 0.5 of a steady-state reflectivity). At any experimental conditions here the output radiation corresponded to very high quality PC replicas for both incident pumps.

The experiments have been carried out for two beams at large optical path difference between them to provide their temporal incoherence to each other. The beam diameters inside two different $KNbO_3$ samples were about 0.45 mm (for both beams), and incident power was about 90 mW (Ar-ion laser beams). Such relatively wide beams had been chosen to simplify adjustment procedures which with smaller diameters constituted a big problem with a reproducibility of results.

The results obtained demonstrate that the DPCM reflectivity up to 10% are possible at $I_1/I_2 \approx 7$. Some asymmetry of the curves in Fig.6.9(a) indicates some asymmetry in beams overlapping on different crystals. From the response rate viewpoint the optimal condition is $I_1 \approx I_2$ and it is in agreement with the theory in [98] which predicted a lowest threshold: $(\Gamma L)_{thr}^{min} \approx 2$, just as it is for the single loop.

The absolute value of DPCM sensitivity was not very high in this experiment, about 6 mJ. The reason to this was the deliberate broadening of the neck diameters to provide reproducible quantitative experimental dependencies. The coincidence of threshold at $I_1 \approx I_2$ for the single and double loops directly mean that they have the same best possible sensitivity. It means that this scheme can demonstrate DPCM sensitivity better than 0.1 mJ.

We believe that the key result of the measurements of this subsection is the experimental verification that at practically perfect fidelity, the double-loop DPCM demonstrates the sensitivity which is about three orders of magnitude less than other known DPCM devices.

6.7 Conclusion

In this chapter the effect of permanent backscattering of focused CW pump beam by $KNbO_3$ sample at fast scanning of the focal neck over crystal is observed. It is shown that scanning rate at 10 mW input power is more than 10 cm/s. It corresponds to several radians/second rate of angular tracking. The conditions of SDS self-PC of focused unaberrated beam are optimized with respect to fidelity, response rate and minimal fluctuations. They correspond to about 4.10^{-2} convergence angle of focused radiation, i.e. at focal neck length, which is about sample thickness and located in the sample. The minimal energy of incident beam to be conjugated was measured for SDS, single loop and double-loop geometries. The best sensitivity demonstrated corresponds to self-PC via SDS and amounts to about 10^{-5} J, which is the best sensitivity of any PC mirror ever known.

CONCLUSION

This thesis contains two parts: a study of photoanisotropic dynamic gratings and a study of the stimulated diffusion backscattering in the photorefractive crystals.

Because of photoanisotropy of azo-dye-doped polymer materials, we can record field which includes both the state of polarization and the vector characteristics of the total intensity. We have successfully fabricated thin and thick azo-dye doped polymer materials. A new technique of fabrication of high optical quality thick azo-dye-doped polymer materials was proposed. Coupled wave equations were derived to analyse thick photoanisotropic gratings.

We experimentally demonstrated that one could successfully store and reconstruct an elliptical polarization state of light using photoanisotropic materials. This reconstruction is possible even if a plane polarized reference beam is used for the recording and readout. We believe that for the first time, a linearly and an elliptically polarized beams were used to record gratings. Theoretical analysis for this case was made and the conditions for reconstruction of an elliptical polarization were obtained. The theoretical results and the experiment have shown that the diffraction by photoanisotropic thin gratings is much more complicated than by scalar gratings. The polarization state of the diffracted signal depends on the polarization state of the probe beam. The analysis give us a detailed understanding which unable us to optimize the parameters of the experimentally fabricated azo-dye doped polymer films in order to obtain the highest possible diffraction efficiency and the conditions to reconstruct needed polarization.

We have performed the first theoretical analysis of volume dynamic holographic recording using reflection geometry. We experimentally demonstrated a light-induced helicoidal structure in non-chiral polymer films i.e. an optical axis gradually rotates around the

thickness of the film, like a helix. Polarization properties of the recorded reflection gratings are similar to cholesteric liquid crystals: the response of the system differs between the left and the right circularly polarized light.

We studied linear diffraction gratings that provide asymmetric diffraction without surface modulation. Asymmetric diffraction is usually achieved using blazed gratings. But in our case, the spatial phase shift of the refractive index grating relative to the absorption grating is the origin of asymmetric behavior. The spatial phase shift between the absorption and the phase grating present in photoanisotropic materials has been discussed for thick and thin gratings. For the first time, to our knowledge the experiment was made using artificially shifted gratings. The obtained experimental results with thin mixed phase and absorption gratings in azo-dye-doped polymer films are consistant with our theoretical results. It has been demonstrated that diffraction efficiency shows strong dependence on dephasing. The most significant asymmetry (with maximum ratio $I_{+1}/I_{-1} = 7.1$) of diffraction takes place when the amplitude grating is $\pi/2$ out of phase with respect to the phase grating. We believe that the proposed approach and the results obtained for shifted gratings may find interesting applications. In contrast to photorefractive media, this device is a linear optical element, is not expensive and is easy to control. The application of lasing dyes or ions (for example, erbium) would permit their use in optical data communication systems for which asymmetric reflection and amplification are needed.

Future work in this field could focus on numerous issues. We believe that the results obtained could be significantly improved in the future using doped polymer materials with higher birefringence. Photoanisotropic materials would allow observing much reflectivity, optical activity and circular dichroism in the experience with helicoidal standing waves. It would be interesting in the future to try a holographic recording technique along with the use of new dyes with better spectral separation to obtain much stronger asymmetric diffraction. It also would be interesting to try the experimental recording of shifted phase and absorption transmission and reflection volume gratings. Similar results may be expected to be obtained for slanted gratings.

The results in the second part of the thesis have been obtained for heavily iron doped $KNb0_3$ crystals as nonlinear medium that demonstrate the best parameters for backscattering. This study is aimed at quantitative characterization of both the relevant material properties and waves mixing parameters as well as at analysis of prospects of this effect from the viewpoint of creation of effective phase conjugate mirrors.

We demonstrated that reflection gratings geometries provide for photorefractive mixing a lot of advantages including highest possible space-charge grating amplitude, best response rate and possibility of sharp focusing of radiation.

A new polarization method of stimulated diffusion backscattering gain measurements in the conditions of high pump-depleting total gain was proposed and used. Iron doped $KNbO_3$ crystals demonstrated in visible the backward SDS gain of 15 cm^{-1} which can be potentially increased at proper doping up to 45 cm^{-1}. Self-seeded SDS effect is excited at linearly polarised pump along x-orthorhombic crystal axis only. The grating response time is always less than 0.2 s and is monotonously shortened with a growth of illuminating intensity. The best response time, obtained up to now to our knowledge, is about 0.1 ms and corresponded to about 3 kW/cm^2 intensity. The new method to measure Debye radius was proposed. We observed dark decay, which results from domination of shallow trapping centers and completely washes out in these samples any photorefractive gratings during less or about one second. We concluded that just shallow trapping centers are responsible for space-charge gratings formation in $Fe:KNbO_3$.

Reliable self-PC at more than 50% both reflectivity and fidelity is demonstrated by SDS at sharp enough (the whole focal neck should be inside the sample) pump beam focusing and for unaberrated pumps only. The self-PC in this case takes place both for steady state illumination and for the pump neck transverse scanning at a speed more than 10 cm/s in the sample.

We observed that dark conductivity is very high in our photorefractive crystal. The condition of phase conjugation discrimination mechanism was obtained. Sensitivities with

respect to self-starting for PC mirrors based on SDS, on single conjugating loop and on double loop mutual conjugation geometries operating at reflection gratings had been measured for the Fe:$KNbO_3$ sample. We obtained the best value of sensitivity, about 0.01mJ, obtained till now for self-seeded SDS of a single unaberrated pump beam.

All the results obtained convincingly indicate very high potential abilities of SDS based photorefractive schemes in application, in particular, for fast PC-tracking. They also showed perspective directions of further research in this field. These directions are related to optimization of crystal growth and treatment procedures aimed at higher gain either potassium niobate or barium titanate samples (especially doped with rhodium for application in infrared region) as well as of wave mixing conditions. It seems that it would be interesting to spread reflection grating geometry to semiconductors which demonstrate very fast photorefractive response in near infrared region that is rather high practical interest from the viewpoint of compatibility with semiconductor laser sources.

REFERENCES

1. Collier, R.J., C.B. Burckhardt, and L.H. Lin, *Optical Holography* (Academic Press, New York, 1971 paperback edition 1977).

2. D'Auria, L., J.P. Huignard, C. Slezak, and E. Spitz, "Experimental holographic read-write memory using 3-D storage," Appl. Opt. **13,** pp. 808-818 (1974).

3. Smith, H.M., ed., *Holographic Recording Materials* (Springer-Verlag, New York, 1977).

4. Preston, K., *Coherent optical Computers*, (Mc-Graw-Hill, New York, 1972).

5. Flanders, D. C., H. Kogelnik, R.V. Schmidt, and C.V. Shank, "Grating filters for thin film optical waveguides", Appl. Phys. Lett. **25,** pp. 194-196 (1974).

6. Marom, E., N. Konforti, "Subtraction via processing simultaneously recorded holographic images," Opt. Commun. **21,** pp.63-66 (1977).

7. Tamir, T., and S.T. Peng, "Analysis and design of grating couplers," Appl. Phys. **14,** pp. 235-254 (1977).

8. Zel'dovich, B.Ya., N.F. Pilipetsky, V.V.Shkunov, *Principles of Phase Conjugation* (Springer-Verlag, Berlin, 1986).

9. Zel'dovich, B.Ya., V.I. Popovichev, V.V. Ragulski, and F.S. Faisullov, "Connection between the wave fronts of the reflected and exciting light in stimulated Mandel'shtam-Brillouin scattering," Sov. Phys. JETP Lett. 15, pp. 109-112 (1972).

10. Fisher, R. A., *Optical Phase Conjugation* (Academic, San Diego, 1984).

11. Todorov, T. and L. Nikolova, "Spectrophotopolarimeter : fast simultaneous real-time measurement of light parameters," Opt. Lett. **17**, pp.358-359 (1992).

12. Ashkin, A., G. D. Boyd, J. M. Dziedic, R. G. Smith, A. A. Ballman, K. Nassau, "Optically-induced refractive index inhomogeneities in $LiNbO_3$ and $LiTaO_3$," Appl. Phys. Lett. **9**, pp. 72-74 (1966).

13. Kukhtarev, N. V., V. M. Markov, S. G. Odulov, M. S. Soskin and V. L. Vinetski, "Holographic storage in electrooptic crystals," Ferroelectrics **22**, pp. 949-959 (1979).

14. Vinetskii, V. L., N. V. Kukhtarev, S. G. Odulov, and M. S. Soskin, "Dynamic self-diffraction of coherent light beams," Sov. Phys. Usp. **22,** pp. 742-756 (1979).

15. Staebler, D. L. and J. J. Amodei, "Coupled wave theory for thick hologram gratings" J. Appl. Phys. **34**, pp. 1042-1049 (1972).

16. Gunter, P. and J.-P. Huignard, eds., *Photorefractive Materials and Their Applications I & II* (Springer-Verlag, Berlin, 1988 & 1989), Vol.61 & 62.

17. Yeh, P., and C. Gu, eds., *Landmark papers on photorefractive nonlinear optics,* (World Scientific, Singapore, 1995).

18. Rau, H., "Photoisomerization of azobenzenes," in *Photochemistry and Photophysics,* J. F. Rabek, ed. (CRC, Boca Raton, Fla., 1990) pp. 119-141.

19. Lessard, R. A., ed., *Photopolymers and Applications in Holography, Optical Data Storage, Optical Sensors, and Interconnects*, Proc. SPIE **2042** (1994).

20. Lessard, R.A., *Photopolymer Device Physics, Chemistry and Applications II*, Proc. SPIE **1559** (1991).

21. Pham, V. P., T. V. Galstyan, A. Granger, R. A. Lessard, "Novel Azo-dye Doped Poly(Methyl Methacrylate) Films as Optical Data Storage Media," Jpn. J. Appl. Physics **36,** pp. 429-438 (1997).

22. Klein, W.R., B.D. Cook, and W.G. Mayer, "Light diffraction by ultrasonic gratings," Acustica **15**, pp. 67-69 (1965).

23. Nath, N.S.N., "Diffraction of light by supersonic waves," Proc. Ind. Acad. Sc. A **8**, pp. 499-454 (1938).

24. Kogelnik, H., "Coupled wave theory for thick hologram gratings," Bell Syst. Tech. J. **48**, pp. 2909-2947 (1969).

25. Montemazzani, G. and M. Zgonik, "Light diffraction at mixed phase and absorption gratings in anisotropic media for arbitrary geometries," Phys. Rev. E **55**, pp. 1035-1047 (1997).

26. Moharam, M.G., T.K. Gaylord, R. Magnusson, "Criteria for Raman-Nath regime diffraction by phase gratings," Opt.Commun. **32**, pp. 19-23 (1980).

27. Moharam, M.G., T.K. Gaylord, R. Magnusson, "Criteria for Bragg regime diffraction by phase gratings," Opt.Commun. **32**, pp. 14-18 (1980).

28. Moharam, M.G. and T.K. Gaylord, "Three-dimensional vector coupled-wave analysis of planar-grating diffraction," J. Opt. Soc. Am. **73,** pp. 1105-1112 (1983).

29. Moharam, M.G. and T.K. Gaylord, "Rigorous coupled –wave analysis of planar-grating diffraction," J. Opt. Soc. Am. **71,** pp. 811-818 (1981).

30. Russell, P.J. and L. Solymar, "Borrman-like anomalous effects in volume holography," Appl. Phys. **22,** pp. 335-353 (1080).

31. Todorov, T., L. Nikolova, and N. Tomova, "Polarization holography. 1: A new high efficiency organic material with reversible photoinduced birefringence," Appl. Opt. **23,** pp. 4309-4312, (1984).

32. Todorov, T., L. Nikolova, and N. Tomova, "Polarization holography. 2: Polarization holographic gratings in photoanisotropic materials with and without intrinsic birefringence," Appl. Opt. **23,** pp. 4588-4591 (1984).

33. Todorov, T., L. Nikolova, K. Stoyanova, and N. Tomova, "Polarization holography. 3: Some applications of polarization holographic recording," Appl. Opt. **24,** pp. 785-787 (1985).

34. Todorov, T., L. Nikolova, N. Tomova, V. Dragostinova, "Photoinduced anisotropy in rigid dye solutions for transient polarization holography," IEEE J. Quantum Electron. **22**, pp. 1262-1266 (1986).

35. Nikolova, L., P. Markovsky, N. Tomova, V. Dragostinova and N. Mateva, "Optically-controlled photo-induced birefringence in photoanisotropic materials," J. Mod. Opt. **35,** pp. 1789-1799 (1988).

36. Nikolova, L., T. Todorov, M. Ivanov, F. Andruzzi, S. Hvilsted, P.S. Ramanujam, "Photoinduced circular anisotropy in side-chain azobenzene polyesters,", Opt. Materials **8,** pp. 255-258 (1997).

37. Makushenko, M., B.S. Neporent, and O.V. Stolbova, "Reversible orientational photodichroism and photoisomerization of aromatic azo compounds I: model of the system," Opt. Specrosc. **31,** pp. 295-299 (1971).

38. Makushenko, A.M., B.S. Neporent, and O.V. Stolbova, "Reversible orientational photodichroism and photoisomerization of complex organic compounds in viscous solutions II: azobenzene and substituted azobenzene derivatives," Opt. Specrosc. **31,** pp. 397-401 (1971).

39. Makushenko, A.M., B.S. Neporent, and O.V. Stolbova, "Reversible orientational photodichroism and photoisomerization in viscous solutions of complex organic substances," Opt. Specrosc. **31,** pp. 331-335 (1971).

40. Kakishashvili, S.D., "Polarization recording of holograms," Opt. Spectrosc. **33**, pp. 90-94 (1972).

41. Kakichashvili, S.D., "Regularity in photoanisotropic phenomena," Opt. Spectrosc. **52,** pp.191-194 (1982).

42. Kakishashvili, S.D., "Polarization holography: possibilities and the future," Proc. SPIE **1183,** pp. 290-295 (1989).

43. Kakichashvili, S.D., "Polarizational holographic recording on practical photoanisotropic materials," Opt. Spectrosc. **42**, pp. 218-220 (1976).

44. Couture, J.J.A. and R.A.Lessard, "Modulation transfer function measurements for thin layers of azo dyes in PVA matrix used as an optical recording media", Appl. Opt. **27,** pp. 3368-3374 (1988).

45. Huang, T. and K. Wagner, "Holographic diffraction in photoanisotropic organic materials," J. Opt. Soc. Am. A **10**, pp. 306-315 (1993).

46. Huang, T. and K. Wagner, "Photoanisotropic incoherent-to-coherent optical conversion," Appl. Opt. **32,** pp. 1888-1900 (1993).

47. Dumont, M., "Photoinduced orientational order in dye-doped amorphous polymeric films," Mol. Cryst. Liq. Cryst. **282**, pp. 437-450 (1996).

48. Dumont, M., S. Hosotte, G. Froc and Z. Sekkat, "Orientational manipulation of chromophores through photoisomerization," Proc. SPIE **2042,** pp. 2-13 (1994).

49. Sekkat, Z., W. Knoll, "Photoreactive organic thin films in the light of bound electromagnetic waves," in *Advances in Photochemistry*, Vol. 22, Eds. D. C. Neckers, D. H. Volman, G. von Bünau (John Wiley&Sons, Inc, 1997).

50. Birabassov, R., N. Landraud, T.V. Galstyan, A. Ritcey, C. G. Bazuin, T. Rahem, "Thick dye-doped poly(methyl methacylate) films for real-time holography," Appl. Opt. **37**, pp. 8264-8269 (1998).

51. Birabassov, R., T. V. Galstyan, F. Dechamplain, T. Rahem, A. Ritcey, "Nouveaux matériaux à base de cellulose dopée par DR1 pour les applications photoniques", Colloque d'Optique Guidée et Photonique V, 66^{e} Congrès de l'ACFAS (Laval University, Quebec City, Canada, 1998).

52. Birabassov, R., T. V. Galstyan, F. Dechamplain, A. Ritcey, "Azo-dye-doped cellulose acetate for optical data storage and processing," Proc. SPIE **3491**, pp 704-711 (1998).

53. Birabassov, R., T.V. Galstyan, F. Dechamplain, A. Ritcey "Polarization recording and reconstruction in Disperse Red 1–doped cellulose acetate," Opt. Lett. **24**, pp. 649-651 (1999).

54. Birabassov R., T. Galstyan "Holographic recording and reconstruction of the angular momentum of light in doped polymers", European Conference on Lasers and Electro-Optics (Nice, France, 2000).

55. Blombergen, N., "The stimulated Raman effect," Amer. J. Phys. 35 pp. 989-1004 (1967).

56. Chiao, R.Y., C.H. Townes and B.P. Stoicheff, "Stimulated Brillouin scattering and coherent generation of intense hypersonic waves," Phys. Rev. Lett. **12** pp. 592-594 (1964).

57. Fabelinski, I.L., D.I. Mash, V.V. Morozov, and V.S. Starunov, "Stimulated scattering of light in hydrogen-gas at low pressures", Phys. Lett. **27,** pp.253-255 (1968).

58. Kanaev, I.F., V.K.Malinovsky, B.I.Sturman, "Effects of induced reflection and transparency in electrooptic crystals," Zh. Eksp. Teor. Fiz. (JETP) **74**, pp.1599-1602 (1978).

59. Patai, S., *The Chemistry of the Hydrazo, Azo and Azoxy Groups* (NY, Wiley, 1975).

60. Kuzyk, M.G., K.D. Singer, H.E. Zahn, and L.A. King, "Second-order nonlinear-optical tensor properties of poled films under stress," J. Opt. Soc. Am.B **6,** pp. 742-752 (1989).

61. Robertson, R. E., "Effect of free volume fluctuations on polymeric relaxation in the glassy state," J. Polym. Sci. Polym. Symp. **1,** pp.173-177 (1978).

62. Wu, P., W. Chen, X. Gong, G. Zhang, G. Tang, "Red-band holographic storage in azo dye sensitised by noncoherent light," Opt. Lett. **21**, pp. 429-431 (1996).

63. Lefin, P., Fiorini C., Nunzi J.M., "Anisotropy of the photoinduced translation diffusion of azo-dyes," Optical Materials **9**, pp. 323-327 (1998).

64. Birabassov, R., A. Yesayan, T. V. Galstyan, "Nonreciprocal diffraction by spatial modulation of absorption and refraction," Opt. Lett. **24**, pp.1669-1671 (1999).

65. Birabassov R., A. Yesayan, T. Galstyan, "Artificially created nonreciprocal diffraction gratings in dye-doped polymer materials", Diffractive Optics and Micro-Optics 2000, Optical Society of America (OSA) Technical Digest, 63-65 (2000).

66. Birabassov R., T. Galstyan, "Holographic reflection gratings in dye-doped polymer materials", International Conference on Applications of Photonic Technology (ICAPT'2000) (Quebec City, Canada, 2000).

67. Galstyan, T. V., B. Ya. Zel'dovich, I. C. Khoo, N. V. Tabiryan, Sov. Phys. JETP **73**, pp. 409-414 (1991).

68. Kastler, M.A., "Champ lumineux stationnaire à srtucture hélicoidale dans une cavité laser," C.R. Acad. Sci. Paris **271b**, pp. 999-1001 (1970).

69. Nikolova, L., P.Sharlanjiev, "Holographic reflection gratings in photoanisotropic materials," Proc. SPIE **1183**, pp. 260-267 (1983).

70. Evthuhov, V. and A.E. Siegman, "A twisted-mode technique for obtaining axially uniform energy density in a laser cavity," Appl. Opt. **4**, pp.142-143 (1965).

71. de Gennes, P.G., *The Physics of Liquid Crystals* (Oxford University Press, New York, 1993).

72. Rudenko, E. V., A. V. Sukhov, Sov. JETP **78** (6), 875 (1994).

73. Kippelen, B., K. Meerholz, N. Peygambarian, *Nonlinear Optics of Organic Molecules and Polymers*, edited by H. S. Nalwa and S. Miyata, (Boca Raton 1997), pp. 465-513.

74. Berry, M. V., *The diffraction of light by ultrasound*, (Academic Press, 1966).

75. Boucher, Y., "Non-reciprocal effects of complex-coupled distributed-feedback structures resulting from the phase difference between the coupling constants," Optics Communications, **136** 410-414 (1997).

76. Yeh, P., "Contra-directional two-wave mixing in photorefractive media," Opt. Commun. **45,** pp. 323-326 (1983).

77. Odoulov, S. G., O. I. Oleynik, Kvantovaya Elektron. **10**, 1498 (1983).

78. Erbschloe, D., L.Solymar, J.Takacs, T.Wilson, "Two-wave mixing in reflection holograms in photorefractive materials," IEEE J. Quant. Electron. **24**, pp. 820-825 (1988).

79. Cronin-Golomb, M., B.Fischer, J.O.White, A.Yariv, Theory and applications of four-wave mixing in photorefractive media," IEEE J. Quant. Electron. **20**, pp. 12-30 (1984).

80. Hellwarth, R. W., "Generation of time-reversed wave fronts by nonlinear refraction" J. Opt. Soc. Am. **67**, 1 (1977).

81. Ewbank, M.D., R.A.Vazquez, R.R.Neurgaonkar, F.Vachss, "Contradirectional two-beam coupling in absorptive photorefractive materials: application to Rh-doped strontium barium niobate (SBN:60)," J. Opt. Soc. Am. B **12**, pp. 87-97 (1995).

82. Chang, T.Y., R.W.Hellwarth, "Optical phase conjugation by backscattering in barium titanate, " Opt. Lett. **10**, pp. 108-110 (1985).

83. Mamaev, A.V., V.V.Shkunov, "Transient self phase conjugation in lithium niobate crystals," Kvantovaya Electron. **16**, pp. 1317-1318 (1988).

84. Mamaev, A.V., V.V. Shkunov, "Interaction of contrapropagating waves with self phase conjugation in a $BaTiO_3$ crystal," Kvantovaya Electron. **16**, pp. 1863-1869 (1989).

85. Mamaev, A.V., V.V.Shkunov, "Mutual optical phase conjugation at stimulated diffusion backscattering, " Kvantovaya Elektron. **17**, pp. 389-390 (1990).

86. Mamaev, A.V., V.V.Shkunov, "Mechanisms of discrimination for phase conjugation at stimulated diffusion scattering in a backward direction in photorefractive crystals," Izvestiya Acad. of Sc. USSR **54**, pp. 1036-1041 (1990).

87. Dyakov, V.A., S.A.Korol'kov, A.V.Mamaev, V.V.Shkunov, "Self conjugation of a "boiling" speckle pattern at backward SDS in $KNbO_3$:Fe crystal," Kvantovaya Elektron. **19**, pp. 1093-1096 (1992).

88. Dyakov, V.A., S. A. Korol'kov, A. V. Mamaev, V. V. Shkunov, "Self-conjugation of pump waves with a boiling speckle-structure under SDBS in $KNbO_3$:Fe Crystal," Proceedings SPIE **1841**, pp. 68-73 (1992).

89. D'yakov, V. A., S. A. Korol'kov, A. V. Mamaev, V. V. Shkunov, A. A. Zozulya, "Reflection-grating photorefractive self-pumped ring mirror," Opt. Lett. **16**, pp. 1614-1616 (1991).

90. Birabassov, R., A.V. Mamaev, V.V. Shkunov, Final Report of the Laboratory of Optical Means for Informatics and Control, Institute for Problems in Mechanics (Moscow, Russia, 1996).

91. Korol'kov, S.A., A.V.Mamaev, V.V.Shkunov, "Stimulated diffusion backscattering with phase conjugation," Int. Journ. Nonl. Opt. Physics **2**, pp. 157-169 (1993).

92. Kuz'minov, Yu.S., A.V.Mamaev, V.V.Shkunov, T.V.Yakovleva, "Steady-state energy exchange of speckle-beams in photorefractive crystals," Journ. Tech. Physics **61**, pp. 94-98 (1991).

93. Vinokurov, V.I., V.V. Shkunov, "Theory of self phase conjugation at transient stimulated diffusion backscattering in photorefractive crystals," Zh. Eksp. Teor. Fiz (JETP) **97**, pp. 1486-1490 (1990).

94. Gusev, V., B.Ya Zel'dovich, V.A. Krivoschekov, V.V. Shkunov, "Stimulated diffusion backscattering for nanosecond pulses at exposure accumulating regime," Zh. Eksp. Teor. Fiz. (JETP) **99**, pp.1082-1087 (1991).

95. Mamaev, A.V., K.Orazov, V.V.Shkunov, and M.V.Zolotarev, "Shallow traps in doped SBN crystals," Optical Materials **4**, pp. 188-191 (1995).

96. Taebati, P., D.Magherefteh, "Theory of the photorefractive effect for $Bi_{12}SiO_{20}$ and $BaTiO_3$ with shallow traps," J. Opt. Soc. Am. B **3**, pp. 1053-1064 (1991).

97. Bel'dugina, N. I., A. V. Mamaev, V. V. Shkunov, "Dynamics of Self-Starting Generation of a Phase-Conjugate Semilinear Mirror," Appl. Opt. **32**, pp.3962-3968 (1993).

98. Mamaev, A.V., A. A. Zozulya, "Conjuagation of mutually incoherent light beams in the geometry of two interconnected ring mirrors," J. Opt. Soc. Am. B **8**, pp. 1447-1454 (1991).

99. Zozulya, A.A. and A.V. Mamaev, "Mutual conjugation of incoherent light beams in a photorefrctive crystal," JETP Lett. **49**, pp. 553-556 (1986).

100. Honda, T. and H. Matsumoto, "Reflection-grating self-pumped phase conjugation with $BaTiO_3$:Co and compensation for air turbulence," J. Opt. Soc. Am. B **11,** pp. 1983-1991 (1994).

101. Honda, T., T.Yamashita, H.Matsumoto. "Self-pumped phase conjugation with $BaTiO_3$ in a reflection-grating ring configuration" Opt. Communs., **103**, pp. 434-441 (1993).

102. Honda, T., H. Matsumoto, "Reflection-grating self-pumped phase conjugation with optical feedback free of input conditions," Appl. Opt. **33**, pp. 4475-4481 (1994).

103. Valley, G.C., "Competition between forward- and backward-stimulated photorefractive scattering in $BaTiO_3$," J. Opt. Soc. Am. B **4,** pp.14-19 (1987).

104. Valley, G.C., "Evolution of phase conjugate waves in stimulated photorefractive backscattering," J. Opt. Soc. Am. B **9,** pp. 1440-1448 (1992).

105. Mullen, R.A., D.J.Vickers, L.West, D.M.Pepper, "Phase conjugation by stimulated photorefractive scattering using a retroreflected seeding beam," J. Opt. Soc. Am. B **9**, pp.1726-1734 (1992).

106. Zgonik, M., R.Schlesser, I.Biaggio, E.Voit, J.Tscherry, P.Gunter, "Materials Constants of $KNbO_3$ relevant for electro- and acousto-optics," J. Appl. Phys. **74**, pp. 1287-1291 (1993).

107. Tschudi, T., A.Herden, J.Goltz, H.Klumb, F.Laeri, J.Albers, "Image amplification by two- and four-wave mixing on $BaTiO_3$ photorefractive crystals," IEEE J. Quant. Electr. **22**, pp. 1493-1501 (1986).

108. Biaggio, I., M.Zgonik, P.Gunter, "Speed Limit of the Photorefractive Effect in $KNbO_3$," Ferroelectrics **126**, pp. 15-19 (1992).

109. Ewbank, M.D., "Mechanism for photorefractive phase conjugation using incoherent beams," Opt. Lett. **13**, pp. 47-49 (1988).

110. Weiss, S., S. Sternklar, and B. Fisher, "Double phase conjugate mirror : analysis, demonstration, and applications," **12,** pp. 114-116 (1987).

111. Engin, D., M. Segev, S. Odulov, A. Yariv, "Double phase conjugation," J. Opt. Soc. Am. B **11,** pp. 1708-1717 (1994).

112. Orlov, S., M. Segev, A. Yariv, G.C. Valley, "Conjugation fidelity and reflectivity in photorefractive double phase-conjugate mirrors," Opt. Lett. **19**, pp. 578-580 (1994).

113. Eliseev, V.V., V.T. Tikhonchuk, and A.A. Zozulya, "Double phase-conjugate mirror: two-dimensional analysis," J.Opt.Soc.Am. B **8,** pp. 2497-2504 (1991).

114. Lyubomudrov, O.V. and V.V. Shkunov, "The threshold of double phase conjugate mirror for speckle pattern reversal," Kvantovaya Electron. **19**, pp. 1102-1106 (1992).

115. Sturman, B.I., Kvantovaya Electron. **7,** pp. 483-488 (1980).

116. Wechsler, B.A., M.B. Klein, C.C. Nelson, and R.N. Schwartz, Spectroscopic and photorefrective properties of infrared-sensitive rhodium-doped barium titanate," Opt. Lett. **19**, pp. 536-538 (1994).

117. Kaczmarek, M., R.W. Eason, "Very-high-gain single-pass two-beam coupling in blue Rh: $BaTiO_3$," Opt. Lett. **20**, pp. 1850-1852 (1995).

118. Liu, D., G. Manivannan, H.H. Arsenault and R.A.Lessard, "Assymmetry in the diffraction spectrum of reflection hologram grating", J. Modern Optics **42**, pp. 639-653 (1995).